THIN FILM HEAT TRANSFER GAUGES FOR SHORT DURATION TRANSIENT MEASUREMENTS

A thesis

Submitted in Partial Fulfillment of the Requirements for the Award of the Degree of

DOCTOR OF PHILOSOPHY

By

Shrutidhara Sarma

DEPARTMENT OF MECHANICAL ENGINEERING

INDIAN INSTITUTE OF TECHNOLOGY GUWAHATI

APRIL 2017

DECLARATION

I hereby certify that the work compiled in this dissertation is the outcome of the research work, performed by myself, else stated, under the guidance of Prof. Niranjan Sahoo and Prof. Aynur Unal.

Any part of this work has not been submitted for the award of any degree, diploma, associate-fellowship, fellowship or its equivalent to any university or institution.

Shrutidhara Sarma

Registration No. 126103013

Department of Mechanical Engineering

Indian Institute of Technology Guwahati

CERTIFICATE

It is certified that the work contained in the thesis entitled **"Thin Film Heat Transfer Gauges for Short Duration Transient Measurements"** by **Shrutidhara Sarma**, a student in the department of Mechanical Engineering, Indian Institute of Technology Guwahati, India, for the award of the degree of the Doctor of Philosophy, has been carried out under our joint supervision and that this work has not been submitted elsewhere for the degree.

Prof. Niranjan Sahoo

(Supervisor)

Professor

Department of Mechanical Engineering

Indian Institute of Technology Guwahati

Guwahati-781039, Assam, India

Prof. Aynur Unal

(Co-Supervisor)

Visiting Professor

Department of Mechanical Engineering

Indian Institute of Technology Guwahati

Guwahati-781039, Assam, India

Dedicated to my parents

Mr. Gunindra Nath Sarma and Mrs. Pranita Devi,

sister Bhaswati Sarma and brother Onkar Sarma,

for whom, I am who I am today.

ACKNOWLEDGEMENT

I am deeply indebted to my supervisors **Prof. Niranjan Sahoo** and **Prof. Aynur Unal**, for their invaluable guidance and steady encouragement throughout my Ph. D. program. The vigor and attention bestowed by them in taking my research ahead in difficult times will never be forgotten. Right from the inception of the problem statement to the final experimental results and physical interpretations, they have remained deeply involved in my thesis work. Their suggestion on ideas, books and journals have been of immense help to me. I also take this opportunity to thank **Prof. Panos Patsalas** for guiding me during the critical phase of my experimental stage and also creating a homely environment in a foreign land. As my supervisors, their optimism will remain a source of inspiration for the rest of my life. I am highly motivated by their intellectual prowess and exemplary professionalism. My association with all of them have been very beneficial both on academic and personal front.

I am also thankful to my doctoral committee members, **Prof. Pinakeswar Mahanta**, **Prof. S. Kanagaraj** and **Prof. Debapratim Das** for providing insightful comments and valuable suggestions during the annual progress seminars and on other occasions too. Their suggestions helped me work in a focused manner.

I would like to express my sincere thanks to **Prof. D. Tassis** and **Prof. E. Hatzekraniotis** from the Department of Physics, Aristotle University of Thessaloniki, GREECE and **Prof. V. Kulkarni**, **Prof. U. S. Dixit**, **Prof. S. R. Deepak**, **Prof. S. N. Joshi**, **Prof. A. Dalal** of the Department of Mechanical Engineering, IIT Guwahati, INDIA for their encouragement and support. I am also thankful to the all Scientific Officers, Lab Assistants and Administrative Staffs of IIT Guwahati who directly or indirectly helped me in completing the thesis work.

I am extremely thankful to my lab mates **Ilias Fekas** and **Nikolaos Pliatsikas** and **Spiros Kassavetis** for helping me with several critical experiments and analysis starting from material growth to characterization. In the same way, I am also grateful to my friends and labmates **Shuvayan Brahmachary**, **Sumit Agarwal**, **Rohit Pauriyal**, **Soumya Ranjan Nanda, Siddharth Kar** and **Siddhant Parvat**, who had been a helping hand throughout.

My friend **Dipika Deb**, my sister **Bhaswati Sarma** and brother **Onkar Sarma** deserve a special "thank you" for lifting up my spirits whenever I got disappointed. I am extremely thankful to my papa **Gunindra Nath Sarma**, ma **Pranita Devi** and my father-like mentors **Prof. Mihir K. Chaudhuri** of Tezpur University and **Prof. Gautam Biswas** of IIT Guwahati, for their patience and the enormous trust they repose in my abilities. Without their moral support, wishes and guidance, it would have been difficult for me to reach this position.

Last but not least, I extend my sincere thanks to all who have helped me directly or indirectly in completing the thesis successfully.

December 2016 SHRUTIDHARA SARMA

LIST OF PUBLICATIONS FROM THIS THESIS WORK

Journals:

i. Sarma S, Unal A, Sahoo N (2016) "Thin film gauges using carbon nanotubes as composite layers". ASME Journal of Engineering Materials and Technology 138: 041014-1-8. doi: 10.1115/1.4033909.

ii. Sarma S, Sahoo N, Unal A (2016) "Calibration of a silver thin film gauge for short duration convective step heat load". SADHANA 41 (7): 787-794. doi: 10.1007/s12046-016-0513-8.

iii. Sarma S, Fekas I, Filintoglou K, Aryanitidis J, Christofilos D, Hatzikraniotis E….Patsalas P (2017) "Layer by layer deposition of alternate CNT and Ni films for efficient multilayer thin film temperature gauges". Carbon. Under review.

iv. Sarma S, Unal A, Sahoo N (2016) "Prediction of impulse heat load on thin film gauges through soft computing technique". Journal of The Institution of Engineers: Series C. Under review.

Conferences:

i. Sarma S, Sahoo N (2013) "Thin film temperature sensors for transient measurement". *Proceedings of the 22nd National and 11th International ISHMT-ASME Heat and Mass Transfer Conference*, IIT Kharagpur-India, 28-31 December.

ii. Sarma S, Sahoo N (2014) "Computational study of a thin film heat transfer gauge for transient measurements". *FMFP-5th International and 41st National Conference on Fluid Mechanics and Fluid Power*, IIT Kanpur-India, 12-14 December.

iii. Sarma S, Agarwal S, Sahoo N (2014) "Numerical and experimental study for measurement of exhaust gas temperature and heat flux using thermal sensors in an internal combustion engine". *ICTACEM-6th International Conference on Theoretical, Applied, Computational and Experimental Mechanics*, IIT Kharagpur-India, 29-31 December.

ABSTRACT

Surface temperature or heat flux measurement has always been one of the major requirements in many scientific and engineering applications and will continue to claim its position in the coming decades too. Certain applications demand transient measurements even in the order of milliseconds and accordingly the techniques used there must have response time fast enough to trace similar variations. In this regard, thin film sensors are the most suitable candidates because of their extremely small thickness which allows them to measure temperature quickly yet accurately. Several practical purposes starting from measurement of surface temperature, heat flux in internal combustion (IC) engines, gas turbine blades to high speed flight experiments utilizes thin film sensors, better known as thin film gauges (TFG).

These TFGs are inherently resistance temperature detectors (RTD) consisting of a thin metallic film (silver/copper/platinum) topped over the surface of substrates of low thermal conductivity (pyrex/macor). They are advantageous in terms of response time, application range and small dimensions. However, these gauges are passive in nature and need to be powered by a constant current source. Furthermore, the measured time-dependent surface temperature of the gauge with the known thermal properties of substrate material, allows estimation of heat flux applied (both steady and transient) on the surface from any source. The purpose of this thesis is to provide a mature approach to the fundamentals of TFGs, right from their modeling, fabrication, characterization to application. Sufficient effort has been laid in this thesis to achieve some amount of expertise in fabricating efficient TFGs.

Various types of TFGs are developed in-house with different techniques during the course of the study. Static calibrations of individual sensors are done using an oil-bath calibration set-up prepared especially for calibration of the gauges. A hot air gun and laser setup set the convective and radiation type of environment, for carrying out dynamic calibration of the gauges. Static calibration is done to determine sensitivity or temperature co-efficient of resistance (TCR) whereas dynamic calibration is done to check gauge response in real-time environments. The performance capacity of different TFGs is compared and methods of

improving sensitivity/TCR are explored. Few such methods used for efficiency enhancement of TFGs are addition of nanoparticles with base film material, study relation between film thickness and resistivity, deposit films on substrates in different ways etc. Numerical analyses have been done to verify the gauge response subjected to transient heat load, using an in-house developed code. Both the dynamic calibration setups are analyzed numerically using commercial software to validate the experimental results.

In the latter part of the study, utilization of soft computing techniques in deriving heat flux from the temperature histories has been attempted. The method is established as a novel and quick technique for heat flux determination compared to the usual lengthy and complicated analytical techniques based on one-dimensional heat transfer in semi-infinite gauges. The study gets further extended to modeling of thermo-electrical properties of the TFGs.

Finally, carbon nanotubes (CNTs) are grown (in-house) over Si substrates using a catalyst assisted low pressure chemical vapor deposition (LPCVD) system with a view to building multilayer films for multilayer TFGs. The final multilayer structure comprises of alternate layers of Ni and multi-walled carbon nanotubes (MWCNT); its position as a temperature sensor being adjudged with single layer Ni/CNT structure. Various characterization techniques like Raman spectroscopy, scanning electron microscopy (SEM), X-ray photoelectron spectroscopy (XPS), Auger electron spectroscopy (AES) and optical spectroscopy are performed to get a detail idea about the film structure, quality of nanomaterials grown, thickness, chemical bonding etc. The electrical properties of the CNT films are investigated by a Van der Paw setup. TCR and Hall coefficients (change of resistance with change in magnetic field in a magnetic environment) measured, confirm that these materials are apt candidates for temperature sensing. Films of bi and few layer graphene are also grown but electrical measurements on them are not possible since they grew in separate domains instead of continuous films. Continuous graphene films for temperature sensing can be considered a total new domain of future prospects of this study.

Nomenclature

a : Atomic radius (nm)

b : Opening between atoms (nm)

c : Specific heat capacity (J/kg. K)

$d(hkl)$: Spacing between crystal planes

D : Beam diameter (mm)

n : Integer

E : Distance from surface of the gauge to the substrate (nm)

C, δ, γ : Constants

k : Thermal conductivity (W/m. K)

K : Boltzmann constant

k' : Constant (between 0 and 1)

N : Experimental parameter

m, n, o : Constants

q'' : Heat flux (kW/m^2)

q_s : Surface heat flux (kW/m^2)

P : Power (W)

R : Film resistance at surface temperature T (Ω)

t : Time (s)

t' : Film thickness (nm)

T_i : Initial temperature (K)

$T_s(t)$: Surface temperature (K)

u_i : Experimental parameters

V_0 : Initial voltage (V)

$f(t)$: Measured temperature (K)

x : Distance measured from substrate surface (m)

ΔT : Change in temperature (K)

ΔV : Change in voltage (V)

α' : Thermal diffusivity (m^2/s)

α : Temperature Coefficient of Resistance (K^{-1})

λ : Wavelength (nm)

η : Reduction factor

θ : Half of Bragg's angle

$\bar{\theta}$: Polar co-ordinate

ρ : Density (kg/m^3)

ρ' : Resistivity (μΩ-cm)

ρ_0' : Bulk resistivity (μΩ-cm)

$\frac{\tau_1}{\tau_2}$: Ratio of travel time before an electron scatters (s)

ω : Successive over relaxation

Abbreviations

1D: One-dimensional
2D: Two-dimensional
3D: Three-dimensional
AES: Auger Electron Spectroscopy
ANFIS: Adaptive Neuro Fuzzy Inference System
ANN: Artificial Neural Network
CFBP: Cascade Forward Back Propagation
CNT: Carbon Nanotubes
CS: Cubic Spline
DHFG: Direct-Heat-Flux Gauge
DLC: Diamond Like Carbon
DTM: Digital Thickness Monitor
EDX: Energy Dispersive X-ray
FCC: Face Centered Cubic
FESEM: Field Emission Scanning Electron Microscopy
FFBP: Feed Forward Back Propagation
FWHM: Full Width Half Maximum
GTFG: Gold Thin Film Gauge
HT: High Tension
HTC: Heat Transfer Coefficient
IR: Infrared
IRT: Infrared Thermography
LPCVD: Low Pressure Chemical Vapor Deposition
LS: Least Square
LT: Low Tension
MF: Membership Function
MISO: Multiple Input Single Output
MR: Multiple Regressions
MSE: Mean Square Error
MWCNT: Multi-Walled Carbon Nanotubes
NCTFG: Nanocomposite Thin Film Gauge
NISI: Non Integer System Identification
PDE: Partial Differential Equation
PVD: Physical Vapor Deposition
RTD: Resistance Temperature Detector
sccm: Standard Cubic Centimeter
SEM: Scanning Electron Microscopy
SOR: Successive Over Relaxation
STFG: Silver Thin Film Gauge
SWCNT: Single-Walled Carbon Nanotubes
TCR: Temperature Co-efficient of Resistance
TFG: Thin Film Gauge
TLC: Thermo Chromic Liquid Crystals
TSC: Thin Skin Calorimeter
TWG: Thick Wall Gauge
UV: Ultra Violet
VdP: Van der Paw
XAES: X-ray Auger Electron Spectroscopy
XPS: X-ray Photoelectron Spectroscopy
XRD: X-ray Diffractometry

Table of Contents

List of Tables

List of Figures

Chapter 1

Chapter 2

Chapter 3

Chapter 4

Chapter 5

Chapter 6

Chapter 7

Chapter 1

Introduction

1.1 Heat transfer

Heat transfer is the exchange of thermal energy between boundaries of physical systems by virtue of temperature difference. Being a boundary phenomenon, heat transfer is always directional i.e. always taking place from the high temperature system to the low temperature system. When an object/fluid is at a different temperature than its surroundings, thermal energy transfers in such a way that the body and the surroundings reach thermal equilibrium. The discipline of heat transfer in thermal engineering concerns with the generation, use, conversion, and exchange of thermal energy and heat between physical systems.

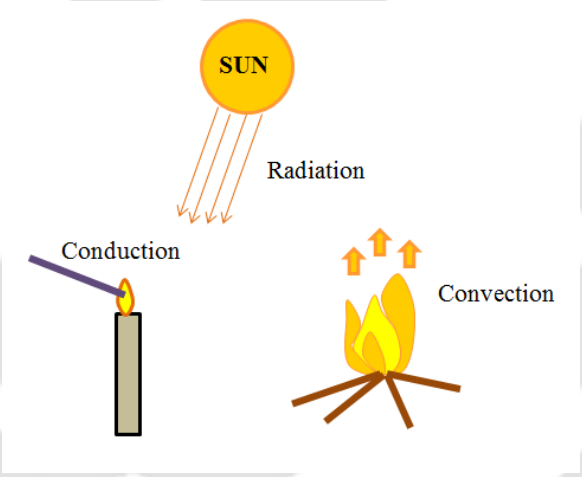

Fig. 1.1 Modes of heat transfer

Heat transfer is classified into various mechanisms, such as conduction, convection, radiation, and transfer of energy by phase changes. Conduction (also called diffusion), is the direct microscopic exchange of kinetic energy of particles through the boundary between two systems. Convection occurs when bulk flow of a fluid (gas or liquid) carries heat along with the flow of matter in the fluid. The flow of fluid may be forced by external processes, or by buoyancy forces (when thermal energy expands the fluid), thus influencing its own transfer. The former process is called “forced convection” while the latter "natural convection". Radiation is the transfer of energy by means of photons in electromagnetic waves. It occurs through a vacuum or any transparent medium (solid or fluid). Interestingly, these mechanisms

occur simultaneously in a system in spite their distinct characteristics. Fig. 1.1 displays different modes of heat transfer.

1.2 One-dimensional heat transfer

Heat transfer is considered one-dimensional (1D) when the amount of heat transfer is prominent in one direction i.e. heat transfer in other directions are negligibly small. For problems where the temperature variation is significant only in one direction, Fourier's Law simplifies to:

$$q'' = -k\frac{\partial T}{\partial x} \text{ or } Q = -kA\frac{\partial T}{\partial x} \tag{1.1}$$

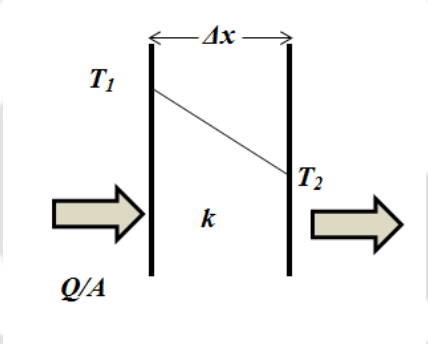

Fig. 1. 2 One-dimensional heat conduction

where, the heat flux q'' depends on given temperature profile T and thermal conductivity k (Fig. 1.2). A negative sign ensures that heat flows down the temperature gradient. The same equation of 1D heat flow through a material of thickness Δx can be discretized as:

$$Q = \frac{kA}{\Delta x}(T_1 - T_2) \tag{1.2}$$

where, T_1 and T_2 are the temperatures at two boundaries.

1.3 Transient heat transfer

Heat transfer is energy in transit due to temperature difference which may occur either under steady state or unsteady conditions. If the temperature of a body does not vary with time, it is said to be in steady state. On the contrary, a continuous change in its surface temperature of a body refers to unsteady or transient state heat transfer. A body under transient condition requires some time to attain an equilibrium or steady state, thus designating a time dependent

phenomenon to the term “transient” or “unsteady”. Transient heat transfer is used in a variety of applications such as internal combustion engines, gas turbines, aircrafts and aerospace industries, heat treatment of metals etc.

1.3.1 Transient heat conduction in semi-infinite solids

A semi-infinite solid is an idealized body that has a single plane surface and extends to infinity in all directions. This idealized body is used to study the temperature change in the part of the body in which we are interested (the region close to the surface) considering the thermal conditions on a single surface. Also, a thick wall can be modeled as a semi-infinite medium if we are interested in the variation of temperature in the region near one of the surfaces, and the other surface is too far to have any impact on the region of interest during the experimental runtime. For short periods of time, most bodies can be modeled as semi-infinite solids since heat does not have sufficient time to penetrate deep into the body, and the thickness of the body does not enter into the heat transfer analysis. Fig. 1.3(a) shows a typical semi-infinite body.

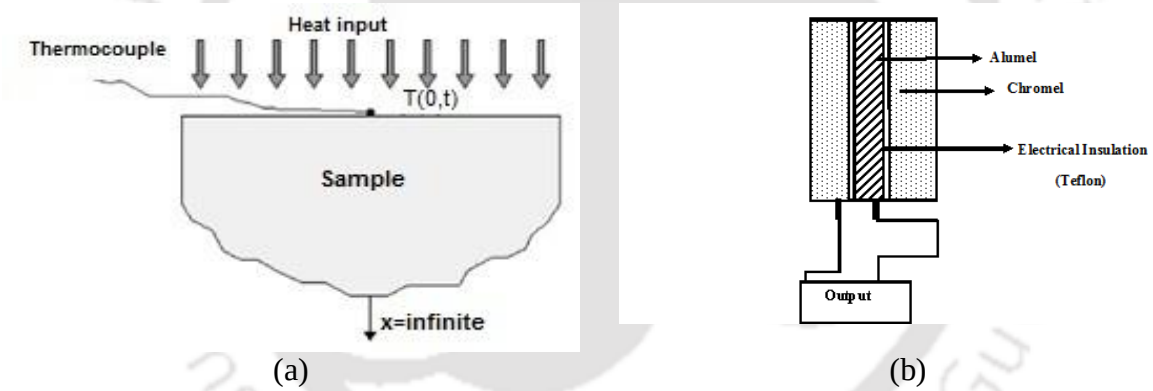

Fig. 1.3 (a) Semi-infinite body (b) K-type coaxial thermocouple

1.4 Heat transfer measurement techniques

There is a wide range of measurement techniques that have been adopted to determine surface heat flux in experiments. In general, most of the transient devices measure the temperature history during the measurement time scale and the heating rates are subsequently predicted from these measurements.

Apparently, thermocouples have been the most commonly used device for such measurements as they are simple, reliable and convenient. Thermocouples work on the fact that any junction of dissimilar metals will produce an electric potential related to temperature;

and so they are called as active devices because no other instruments require activation of the sensing element. The junction of the thermocouple is created by eroding or scratching the surface of the thermocouple. The micro scratches generated through erosion, form the active junction of the thermocouple. Hence it refers to a very small amount of active mass resulting in a short response time. Welding and soldering methods are well established method to join the two dissimilar metallic alloyed wires together to form thermocouple joints. Coaxial thermocouples are of different types depending upon the materials used for the fabrication. Some of them are Type K (Chomel-Alumel), Type E (Chromel-Constantan), Type J (Iron-Constantan). A K-type co-axial thermocouple is shown in Fig. 1.3(b).

Another class of sensors based on semi-infinite theory is broadly classified as, thin film gauges (TFGs), thin skin calorimeters (TSCs) and thick wall gauges (TWGs). They are used for inferring transient temperature signals in short duration impulse facilities. The physical model applied to all the heat transfer gauges is similar i.e. uniform slab where a high conducting sensing element is mounted on an insulating substrate (Fig. 1.4). When a constant heat flux is applied on the surface, the sensing element measures the instantaneous surface temperature which is parabolic in nature. In TFGs (Fig. 1.4(a)), the film is so thin that the measured temperature is same as that of surface temperature**.** TFGs are prepared by coating films of high conducting metals like silver, gold and platinum over an insulating substrate such as pyrex and macor. The corresponding heat flux rate is deduced using the lumped heat conduction formulation with semi-infinite substrate since the thermal penetration depth is negligibly small compared to substrate dimensions during experimental run time. The calorimetric element being thin in TSCs (Fig. 1.4(b)) which are basically thin metal plates with thermocouple wires welded to form a surface junction, the rate of surface temperature rise is approximately equal to the rate of mean temperature rise at the interface. So, the one dimensional heat conduction modeling can thus be applied to extract the heat flux from the mean temperature variations. In contrast, the TWGs (Fig. 1.4(c)) are comparatively thick for which the temperature rise is related to surface heat flux in a complex manner as compared to other gauges. It is measured at the interface of the two materials and subsequent heat flux is determined using inverse heat conduction modeling.

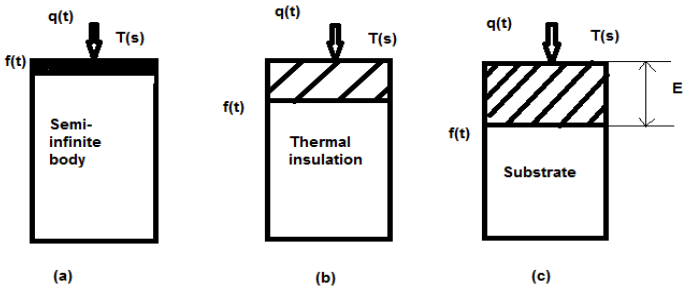

Fig. 1.4 (a) Thin film gauge (b) thin skin calorimeter (c) thick film gauge

Other techniques include optical techniques like infrared and phosphor thermography and temperature-sensitive liquid crystals. Infrared Thermography (IRT) is based on discovery of subsurface features like subsurface thermal properties, presence of surface anomalies/defects etc. IRT is deployed along two schemes, passive an active. The response time of IRT (range of microseconds) strongly depends on the dynamic capabilities of the electronic instruments (amplifier, A/D conversion, etc.) of the measuring line. The thermo-graphic phosphor technique uses the level of emitted visible light from thermo-graphic phosphors when illuminated by ultraviolet light. The varying fluorescence intensity with temperature can be measured.

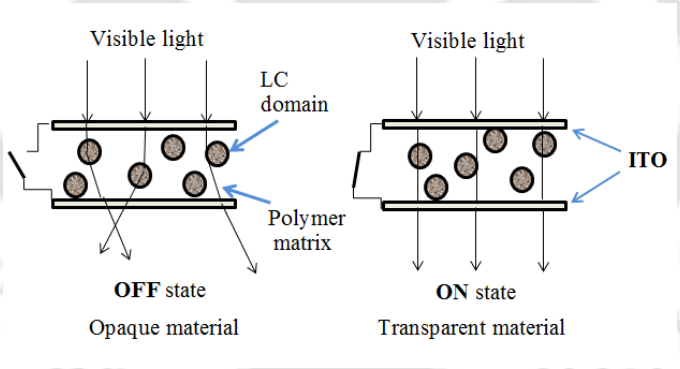

Fig. 1.5 Liquid crystal thermography

Thermo chromic liquid crystals (TLC) are materials that change their reflected color as a function of temperature, when illuminated by white light. Hence, they reflect visible light at different wavelengths (Fig. 1.5). A bright and stable white light source is required to obtain accurate and reliable reflected light intensity from a (TLC) coated surface. The light source must be void of infrared (IR) and ultra-violet (UV) radiation. Any energy content in the incident light in IR, will cause radiant heating of the test surface. Extended exposure to UV radiation can cause rapid deterioration of the TLC surface. This causes the surface to produce

unreliable color-temperature response performance. Consistent light source settings and lighting viewing arrangements between calibration and actual testing are essential to minimize color-temperature interpretation errors.

None of the techniques mentioned above are without drawbacks and each one is limited to particular test conditions. Hence there should be a compromise among temperature limits, sensitivity and response time.

1.5 Thin film gauge

Thin film gauge (TFG) is an emerging technology for measuring surface temperature history that can be used for inferring heating rates. It generally consists of a thin metallic film (usually very conducting material like platinum, nickel, gold or silver) placed on a substrate of poor conductivity. The gauge is mounted on the test surface and temperatures can be obtained by measuring the resistance of the metal film. The basic principle on which the gauges work is that the penetration of heat pulse from a high conducting material to a low conducting one is very small during the span of the experiment. These gauges operate in two modes: constant-temperature (hot-film) mode and constant current mode. In the constant-temperature mode, the gauges can be calibrated to measure skin friction or heat flux as heat transfer in this case occurs primarily by conduction into the substrate. When operated in the constant-current mode, TFGs act as temperature sensors, and heat flux must be inferred from temperature information [O'Brien 1990]. The advantageous characteristics of the TFGs include high precision, sensitivity and most importantly, rapid response times. Unlike thermocouples, the small finite heat capacity of the thin film metal produces instantaneous surface temperature measurements, making the instruments ideal for millisecond test flows. Due to small response time, it can be used in highly transient environment like shock tunnels, Internal Combustion (IC) engine inlet and other industrial applications. The TFGs are also suitable for steady state measurements although their superiority lies in measuring transient temperatures. Once the surface temperature is known, the time dependent heat flux can be recalculated, provided the thermal properties of the substrate are given as a priori. This is accomplished by the theory of heat conduction into a semi-infinite body. Other distinctive advantages of TFG are (i) Ease of fabrication, (ii) Stable and repeatable in measurements, (iii) cost-effective, (iv) adaptability in fitting to any model surface like cone, cylinder, sphere etc. due to its small size and sturdy design.

1.6 Layout of the thesis

The thesis discusses the development of Thin Film Gauges (TFG) for measurement of temperature in transient environment. It investigates both composite and non-composite TFGs and characterizes those details, all the implications that arouse during the Ph. D. timeline. This thesis is organized as follows: Chapter 1 gives an introduction and motivation behind the work carried out. An exhaustive literature survey has been made in Chapter 2. Chapter 3 discusses about numerical modeling of such gauge to determine appropriate dimensions, carried out using commercial software (ANSYS Thermal Transient). Chapter 4 details the fabrication of different conventional/composite TFGs, their characterization using X-ray diffractometry and slightly touches upon the thickness-resistivity relations in the gauges. Chapter 5 describes calibration of the as-fabricated sensors: static calibration for determination of Temperature co-efficient of resistance (TCR) and dynamic calibration (convection and radiation based) to understand their working nature in real-time environments. Chapter 6 investigates the usage of soft computing in modeling thermo-physical properties of TFGs and its use in quick determination of heat flux from temperature history without having to calculate analytically. Chapter 7 discusses about using films of carbon nanotubes (in-house grown) for utilization as TFG materials and the development of multilayer composite film from a monolayer one. This chapter also includes various characterization techniques used for such in-built nanomaterial based films. Finally the concluding remarks and the future work are presented in Chapter 8.

Chapter 2

Literature Review

A thorough literature survey is done about thin film gauges with particular interest on six points:

- Mathematical modeling of transient heat transfer measurement techniques
- Effect of parameters on properties of gauges
- Different types of gauges and their application
- Fundamentals of nanocomposites/nanofluid
- Characterization of film materials and
- Concepts of soft computing in prediction/estimation

The literature study brings out some of the important research work done in the field of heat transfer gauges, and exactly points out the gap between academic achievements and industrial requirements. Each sub category of the literature survey has been described in detail in subsequent paragraphs.

2.1 Mathematical modeling of transient heat transfer measurement techniques

Modeling of heat flux from temperature signal happen to be one of the most significant aspect to research upon as far as heat measurement techniques are concerned. The major way to reduce data is by considering one-dimensional heat conduction in a semi-infinite gauge. Several researchers have contributed significantly. Some notable works are the data reduction numerical technique obtained by **Cook and Felderman (1966**) where it was found that if the response of the TFG is parabolic from initial time; a constant heat flux is indicated. However, if it is not parabolic, it is necessary to determine the heat flux as a function of time. This study of one-dimensional unsteady heat-transfer problem within the thin-film measurement indicated that, at a given time, heat flux depends less on the early temperature-time history than on the shape of the temperature-time curve. Similar work was carried out by **Blackwell (1981)** who further extended it for determination of heat fluxes from experimental thermocouple data when multiple thermocouples at various depths below the heated surface

were used. The prediction of transient heat transfer rate in case of two or multilayer substrate gauges was successfully achieved by **Doorly and Oldfield (1987).** Their experiment, where a TFG response to a step heat input is shown in Fig 2.1.

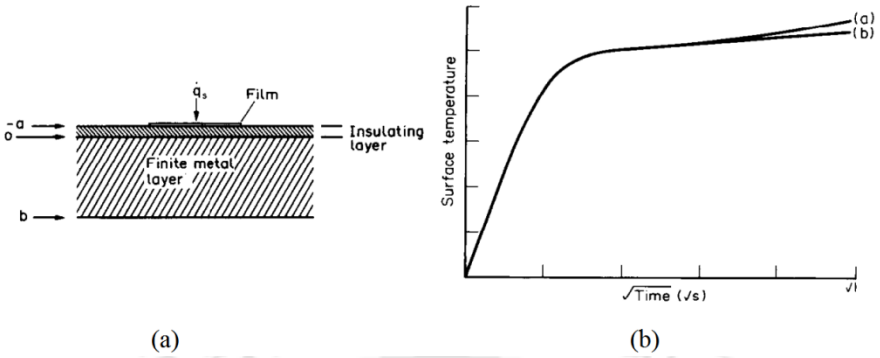

Fig 2.1 (a) TFG on a two layer composite (b) response subject to step heat load [Doorly and Oldfield 1987]

Monte (2000) developed a 'simple and convenient' analytic approach for solving one-dimensional transient heat conduction in a composite slab having layers in perfect thermal contact. A numerical example was employed to calculate the slab temperature profile and the heat exchanged with the surrounding fluid during the transient process. The method was applicable to composites of any number of layers.

Slightly different aspect in modeling was opened by **Mehta et al. (1988)** who investigated the influence of normal and lateral conduction on the temperature distribution and heat transfer coefficient on the surface of a typical sounding rocket using finite element method. The study concluded that the normal conduction was having significant influence in estimation of heat-transfer coefficient, which is why, inclusion of normal conduction in inverse heat conduction problem was a must to predict accurately heat-transfer coefficient in a free flight of a sounding rocket. In a similar way, **George et al. (1991)** discussed the importance of frequency response considerations in the use of thin-film gauges for unsteady heat transfer measurements in transient facilities and proposes methods for evaluating them. A detail description of the unified mathematical procedures of transient methods for measuring surface heat transfer rates was presented by **Jan Taler (1996).** Three types of heat flux gauges namely, thin film, thick-wall gauges placed on semi-infinite substrates and thin-skin calorimeters were described. The author attempted to present a simpler method for accurate determination of transient heat flux from a given temperature history of the body at a selected point beneath the surface. Cubic spline smoothing or digital filtering of the raw interior temperature data was done prior to using them in the inverse heat conduction analysis

in order to reduce the inaccuracies. After couple of years, **Walker and Scott (1998)** evaluated existing methodologies for the determination of the unsteady heat flux and introduced a new approach based on an inverse technique. The performance of these methods were measured in terms of accuracy and their ability to handle inherently unstable or highly dynamic data such as step fluxes, pulse flux, temperature spike and high-frequency oscillating fluxes. Data reduction methods were grouped into three primary classes- analytical (Class 1), direct numerical techniques (Class 2) and a proposed inverse solution technique (Class 3). Class 1 techniques seemed to exaggerate temperature changes and the class 2 could not model the large gradients. Class 1 methods lacked ability to model the physics adequately while Class 2 was restricted in their ability to resolve surface gradients. The class 3 methods were found to be more robust and allowed more accurate estimates than can be obtained with class 1 or 2 techniques. Additional advantages included the statistical elimination of experimental noise, increased stability of the solution, extendibility to multidimensional problems, and the inclusion of other known information and sensor modeling. **Mansur et al. (2009)** presented a numerical solution algorithm for the linear transient heat conduction equation using the 'Explicit Green's Approach'. The method used the Green's matrix that represents the domain of the problem to be solved in terms of the physical properties and geometrical characteristic. The numerical results obtained with the algorithm were quite accurate when compared to analytical solutions and to numerical solutions obtained by the FEM.

Unlike rest of the researchers, **Chantasiriwan (2000)** however, developed an experimental setup for the inverse determination of steady-state heat transfer coefficient in a two-dimensional system. Temperatures were measured at locations where sensors can be conveniently placed without disturbing the fluid flow field. The mathematical model of the system was solved numerically by using the boundary element method. The approach was more computationally intensive than conventional approaches, but the setup was simple and less expensive.

2.2 Effect of parameters on properties of gauges

Hypothesis states that the increase in resistivity with decrease in thickness of a thin film is due to the shortening of the mean free paths of the conduction electrons of the metal by collisions with the boundaries of the film. Results from formula, derived based on the same hypothesis and experimental results were first compared by **Fuchs (1938)** reconsidering the

assumptions. He found that for very thin films, the electrons were all scattered at random at the boundaries of the film and for greater thicknesses the proportion of specular reflexion grew larger with increasing film thickness. Similar study was carried out by **Namba (1970)** but with inclusion of surface roughness, in addition to reduced mean free path of conduction electrons. The ratio of surface roughness to mean free path was included as a parameter to decide the same. He arrived at a conclusion that temperature co-efficient of resistance decreases with increase in surface roughness and becomes zero at certain thickness where resistance tends to infinity, irrespective of the degree of specular reflection of the electrons. When the ratio of roughness to mean free path became zero, the theory became equivalent to Fuchs-Sondheimer theory. However, Namba's theory was limited to thicker films since tunneling current could be neglected in such case. **Durkan and Welland (2000)** took up the effect of size in the electrical resistivity of polycrystalline nanowires to evaluate which of the mechanisms between grain boundary and surface scattering was more relevant since both of them are generally used to explain the thickness dependence on resistivity. An experimental study of the width dependence of the resistivity of thin-film polycrystalline gold nanowires was carried out and the expected behavior was computed on the basis of both surface and grain-boundary scattering mechanisms independently. Resistivity got increased as wire width decreased in a manner which was dependent on the mean grain size; and could not be explained adequately by either model alone. When wire width was comparable to mean film grain size, grain boundary scattering became dominant source of increased resistivity. But, when wire width was below approximately half the size of mean film grain size, surface scattering became important. Finally, they suggested a modification to the Mayadas and Shatzkes model, incorporating the variation of mean grain size on wire dimensions.

A remarkable step was added by Lacy, who carried out a series of experiments to learn the physics behind temperature-resistivity relations in case of thin and thick films. Platinum film temperature sensors were prepared and the temperature-resistivity relation was observed to change when dimensions of the material changed into nanometer size **(Lacy 2007)**. Results indicated that the film resistance was linearly related to temperature below a certain temperature but above that it remained relatively constant. Thinnest films were found to have lower TCR than larger films at a particular temperature. Further characterizations of the nanometer-sized films were carried out including mathematical calculations and finite-element analysis to determine the relationships between the thermal properties and the electrical properties **(Lacy 2009)**. Evaluation of the sensors showed that the sensitivity was

approximately half of the bulk value in these nanometer sized films and the measurement error due to Joule heating could be avoided. Later in 2011, he developed a theoretical framework using solid-state physics and quantum mechanics principles to obtain an equation for bulk conductors that relate resistivity to temperature **(Lacy (2011-a)**. A two-dimensional model for the face centered cubic (FCC) lattice structure was created and an equation was established that expressed electrical resistivity as a function of temperature. Fig 2.2 shows the variation of resistivity with thickness for a copper film sample. The newly developed equation produced a linear relationship for conductors and provided a very good match with experimental data obtained from platinum and nickel RTDs.

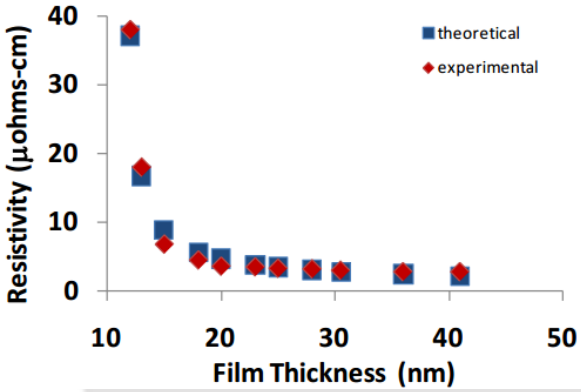

Fig 2.2 Variation of resistivity with thickness for a copper film [Lacy 2011-a]

Further, **Lacy (2011-b)** extended the model to a two-dimensional form. Experimental data confirmed that the model generated accurate results. Two cases were considered: one with the film thickness smaller than the mean free path of the conduction electron and the other with the film thickness greater than the mean free path. The effective resistivity and effective mean free path were calculated and values were provided as input to the already existing temperature-resistivity model to infer the resistivity-film thickness-temperature model. Gamma values (proportionality variable relating energy of atoms to separation distance between atoms) were altered to get even better results. The model took into account various defects like variation of film thickness, irregularities present during fabrication of the gauges, errors due to grain boundaries, uneven surfaces etc. The model provided excellent insight into the underlying physical mechanisms by which the film thickness and temperature affect the electrical resistivity. It was also proved that the properties of material changed from bulk form to nano form. However the model lacked the ability to distinguish between some of the different scattering effects, for example, scattering from grain boundaries and from rough surfaces. Electrical resistivity of thin copper films sputtered onto silicon dioxide measured by

Barnat et al. (2002) showed that average grain size plays a dominant role in the resistivity during growth and a relaxation of resistivity after the termination of growth. This idea was also supported by the experiments carried out by **Camacho and Oliva (2005)** on gold, aluminum and copper films, which revealed grain boundaries to be the main contributions of high electrical resistivity.

Van der Paw [1958] contributed greatly in terms of resistivity measurement in any shape of film by presenting a method based upon a theorem which holds for a flat sample of arbitrary shape and sufficiently small contacts located at the circumference of the sample. Specific resistivity and Hall Effect of flat samples of arbitrary shape could be measured but with a condition that the sample must be void of isolated holes.

With time, many researchers started contributing experimentally by fabricating films of various sizes and studying relation among various film parameters. Some such works are deposition of silver films onto single-crystal silicon substrates by **Dayal et al. (1981)** to correlate film structure with scattering parameter, study by **Kawamura et al. (2000)** on platinum and aluminum films on glass substrate to investigate transitions from discontinuous to continuous film, through characterization of the electrical properties and microstructure of films, development of ultrathin copper films **Liu et al. (2001)** to measure their sheet resistances at different film thicknesses. Other remarkable works are measurement of electrical resistivity/piezoresistances of continuous and coalesced palladium, gold and copper films by **Jen et al. (2003)**, study of overlayers by **Rossnagel and Kuan (2004)**, invention of ordered CuAu I films by **Zhang et al. (2004)** to reduce size effect, preparation of zinc nanowire arrays by **Wang et al. (2006)** to study their melting behavior using the differential scanning calorimetry. In this study, Wang et al. noticed a decrease in melting temperature with decrease of nanowire diameters.

2.3 Heat transfer gauges and their applications

Numerous works has been carried out in terms of heat transfer gauges and their applications. **Lyons and Gai (1988)** determined the thermal product for thin film/surface thermocouple type heat transfer gauges namely a NASA manufactured palladium thin-film gauge on a macor substrate and a K-type surface thermocouple with coaxial symmetry manufactured by the ASEA Corporation of Sweden, by utilizing optical technique. **Jessen and Groenig (1991)** developed a simple method for the production of reusable and rigid thin film heat flux gauges. They also calibrated the gauges (both static and dynamic calibration) to establish

repeatability and accuracy of the sensors. **Lei et al. (1997)** presented two advanced thin film sensors viz. palladium-13% chromium based strain gauges and platinum-13% rhodium vs. platinum thermocouples and demonstrated on a variety of engine materials, including superalloys, ceramics and advanced ceramic matrix composites, in several hostile, high-temperature test environments. They also developed a weld-able strain gauge for applications where sputtering a gauge directly onto a large test article was impossible. **Kinnear and Lu (1999)** developed thin film platinum resistance temperature detectors (RTDs) in order to determine if RTDs are suitable for measuring surface temperatures and heat transfer rates under transient conditions. **Piccini et al. (2000)** developed a new type of direct-heat-flux gauge (DHFG) comprising an insulating layer mounted on a metal substrate. A detailed method of analysis for calculating the surface heat flux from DHFG temperature traces was presented and the DHFGs were applied to a gas turbine nozzle guide vane. **Ewing (2006)** designed and constructed a new thin film heat flux array using a series of nickel/copper thermocouples deposited onto a thin Kapton® polyimide film and calibrated it. In order to measure the signal from the array, amplifiers were designed to increase the magnitude of the voltage output. A test case was designed to study the time-resolved effects of free stream turbulence on heat transfer in stagnating flow using the heat flux array.

Employing such gauges for real time experiment had been reported by **Chana et al. (2001)** where platinum thin film sensors were used in a single cylinder engine for heat transfer measurement. The investigation clearly demonstrated the use of thin film gauges for taking heat transfer measurements in a spark ignition engine operated at realistic conditions. **Saito et al. (2004)** measured the surface convective heat transfer rates to a cylinder using platinum thin film gauges in a shock tube and used the results to validate two numerical codes. The investigations were carried out at different incident shock Mach numbers and flow Reynolds numbers. The heating rate distributions on the model surface showed that maximum heat transfer occurs at the front stagnation point due to a sudden deceleration of the flow behind the normal shock at that point and relatively lower heat transfer rates were observed downstream on the cylinder surface and also in the wake. **Saravanan et al. (2009)** carried out experiments with air as the test gas to obtain the surface convective heating rate on a missile shaped body flying at hypersonic speeds. Measured heat-transfer rate with fin was slightly higher than that of without fin. Heat transfer coefficient of sputtered platinum sensors was repeatable but data measured at stagnation point were always lower for both the Mach numbers when compared with the Fay- Riddell correlation. **Dau et al. (2010)**

fabricated carbon nanotubes (CNTs) thin film on micro electro-mechanical sensors (MEMS) structure, and characterized piezo-resistive coefficients of aligned single wall carbon nanotube (SWCNT) forest film. Specimens were tested on either longitudinal or transverse direction of applied stresses; thus measuring both longitudinal and transverse piezo-resistive coefficients of CNTs film at the same time. Although the gauge factor was small, very good tensile strength with elongation, small Young's modulus value and standard MEMS compatible process made these CNT film applicable in large deformation sensing device.

As far as calibration of the heat flux sensors are concerned, the study of **Gardarein et al. (2009)** to calibrate heat flux sensors of different geometrical designs using the Non-Integer System Identification (NISI) technique is worth mentioning. Another such work is by **Frankel and Keyhani (2013),** who developed theoretically a surface heat flux calibration method applicable to thin-film resistive temperature gauges and co-axial thermocouples. Extraction of the net surface heat flux was acquired by resolving a newly formulated first-kind Volterra integral equation that contained calibration data. Sensor characterization, sensor positioning and thermo-physical properties were implicitly contained in the newly devised calibration integral equation unlike in Cook-Felderman equation. Hence, the calibration equation was expressed only in terms of input–output variables (measured temperatures and surface net heat fluxes) and was applicable to both in-depth and surface analysis.

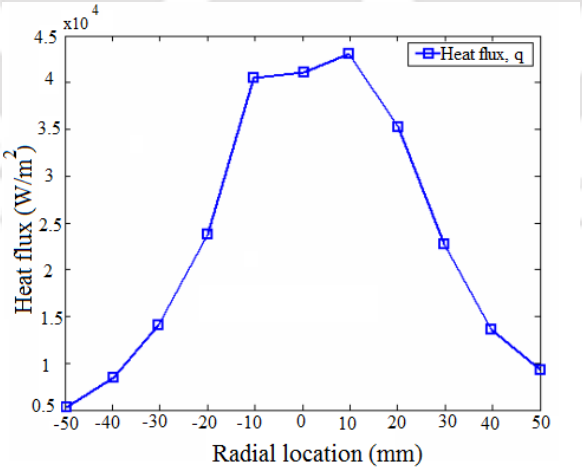

Fig 2.3 Variation of heat flux from the TFG calibration of heat flux using hot air gun [Talib et al. 2005]

Talib et al. (2005) presented a numerical analysis on conduction heat transfer through a custom built thin film gauge that was developed to measure the heat flux from ISO2685 fire-

certification burner under isothermal wall conditions. During calibration of the TFG using a hot air gun, the heat flux was not uniform as heat flux level directly underneath the hot plume was high (Fig 2.3). To investigate the effect of the non-uniform distribution of the heat flux, a two-dimensional numerical analysis was conducted to confirm that one-dimensional conduction conditions prevails throughout the temperature sensing section of the TFG.

Finally, an uncommon study done by **Mocikat and Herwig (2009)** deserves a mention, where they reviewed film-sensors and showed their different modes of operation: primarily passive mode but when used for wall shear stress measurements, the detection of laminar/turbulent transition, or the measurement of certain flow velocities, they were operated in an active mode. The classification of the gauges based on active and passive mode is shown in Fig 2.4.

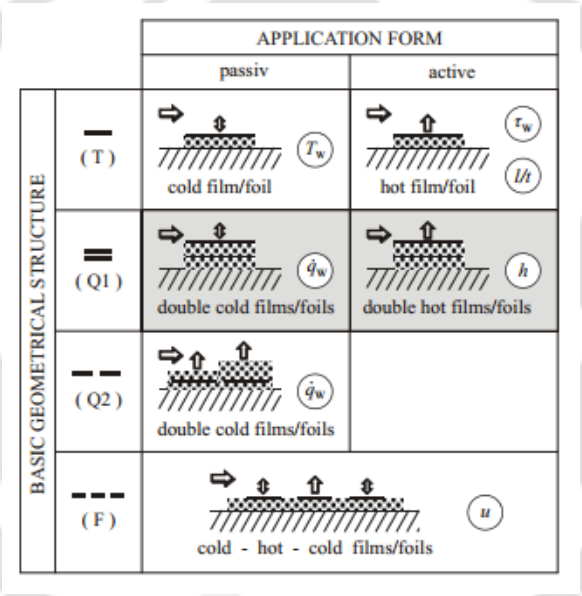

Fig 2.4 Classification of TFG as per application
[Mocikat and Herwig 2009]

They demonstrated how laminated nickel- and polyimide-foils sensors can also be applied in an active mode for heat transfer measurements when made on cold, unheated bodies, provided certain requirements with respect to the flow field are fulfilled. They also found that the convective heat transfer co-efficient measured in active mode did not measure expected values but an equivalent "pseudo" values and named the adjustment co-efficient as "tac factor".

2.4 Fundamentals of nanocomposites/nanofluids

Nanocomposites are composites containing nanoparticles of a material in a base matrix. The base matrix, if solid results in nanocomposite and if liquid, results in nanofluids. Nanocomposites have been a keen area of research for enhancing properties of base material. A few important literatures pertinent to TFGs have been listed in this section. **Xuan and Li (1999)** prepared nanofluid by suspending nanophase powders in a base liquid and studied the thermal conductivity based on factors like volume fraction, dimensions, shapes and properties of the nanoparticles. The measurement results indicated that the thermal conductivity of nanofluids remarkably increases with the volume fraction of ultra-fine particles. It was inferred that by suspending nanophase particles in heating or cooling fluids, the heat transfer performance of the fluid can be significantly improved. Similar study was carried out by mixing nanosized particles of alumina (Al_2O_3) in water to enhance the critical heat flux in pool boiling by **You et al. (2003).** Results showed an unprecedented increase of approximately 200% in critical heat flux measured in nanofluids containing 0.005 g/l of alumina nanoparticles. **Liu et al. (2005)** investigated thermal conductivity enhancements in ethylene glycol and synthetic engine oil in the presence of multiwalled carbon nanotubes (MWNTs). CNT–ethylene glycol suspensions had noticeably higher thermal conductivities than the ethylene glycol base fluid without CNT. Results for CNT–synthetic engine oil suspensions also exhibited the same trend. They also found linear thermal conductivity enhancement for CNT nanofluid with volume fraction of CNT. They attributed the reason for conductivity enhancement to the extensive three dimensional CNT networks that facilitate thermal transport. In a similar study, **Wang and Mujumdar (2006)** reported that much larger relative surface area of nanoparticles not only significantly improves heat transfer capabilities, but also increases the stability of the suspensions. **Loos et al. (2008)** achieved apparent increase in Young's modulus and strength in nanocomposites prepared by adding a small amount of single walled carbon nanotubes (SWCNTs) to an epoxy resin. However, in this regard **Wiegand et al. (2008)** reported the first successful fabrication of metal-single walled carbon nanotubes (SWCNT) composite having significantly enhanced yield strength. They used catalytic chemical vapor deposition to infiltrate metal matrices with single and multiwall carbon nanotubes. **Kakac and Pramuanjaroenkij (2009)** also ended up with similar conclusions of heat transfer enhancement with nanofluid. **Marcq et al. (2011)** proposed a hybrid conductive adhesive filled with silver flakes and carbon nanotubes (DWCNTs or MWCNTs) for achieving high electrical conductivity and improved mechanical

properties. Glassy and rubbery storage moduli of the hybrid composites increased with increasing silver loading at fixed CNTs volume fraction. DWCNTs were more difficult to disperse and therefore no beneficial impact in electrical conductivity was observed in hybrid DWCNT/lAg composites.

Ghadimi et al. (2011) picked up the topic of reviewing stability properties and characterization of nanofluids under stationary conditions. Nanofluids made in one step and two-step process were included. One of the significant findings of their experiment was that a more stable nanofluid does not necessarily have more enhanced characteristics. **Aryasomayajula and Wolter (2013)** reviewed on carbon nanotube composites for electronic packaging applications. Experimental and theoretical calculations showed improved mechanical and physical properties like tensile stress, toughness, and improved electrical and thermal properties. **Fu and Yu (2014)** studied fabrication of carbon nanotube based thin films, their characterization and applications. As per author's opinion, the use of CNTs based thin film represented a challenging but potentially rewarding opportunity to develop the next generation of advanced functional materials.

To add a different angle to nanocomposites, studies on graphene based material were adopted. Despite numerous theoretical suggestions that graphene may also have unusually high thermal conductivity, **Balandin et al. (2008)** investigated that experimentally for the first time with the help of confocal micro-Raman spectroscopy. The extremely high values of the thermal conductivity suggested that graphene could outperform carbon nanotubes (CNTs) in heat conduction. The outstanding thermal properties of graphene provided an extra motivation for integration with the nanometer scale silicon complementary metal oxide semiconductor technology and increase the range of graphene applications as the thermal management material in optoelectronics, photonics and bioengineering.

2.5 Characterization of film materials

The morphology and growth mechanism of thin silver films sputtered on silicon substrates was studied using Atomic Force Microscopy (AFM) and X-ray reflectivity techniques earlier in the year **1998** by **Kundu et al.** Later with the discovery of CNTs, characterization of multiwalled carbon nanotubes, prepared on silica substrates from the thermal decomposition of a ferrocene-xylene mixture was done using polarized Raman spectroscopy by **Rao et al. (2000).** This study showed a strong dependence of the graphite like G band and the disorder-

induced D band on the polarization geometry. Study about bonding and electronic structure of amorphous carbon films on Si substrates, by optical and electron spectroscopy was carried out by **Patsalas et al. (2001).** The sp^3 and sp^2 fractions in the films were calculated by deconvolution of the X-ray photoelectron spectroscopy XPS C1s peak and studied by the differential auger electron spectroscopy (AES) C_{KLL} peak signal. They observed considerable increase of sp^3 content in films deposited with negative bias voltages. Similarly, **Hone et al. (2002)** studied the thermal properties of CNTs and other nanomaterials by measuring the specific heat and thermal conductivity of bulk SWCNT samples. Nanotube-based composite materials were synthesized and their thermal conductivities were also measured. Measured specific heat of single-walled nanotubes differed from both 2D graphene and 3D graphite, especially at low temperatures, where 1D quantization of the phonon band structure was observed. The measured specific heat showed only weak effects of intertube coupling in nanotube bundling. Nanotube–epoxy blends showed significantly enhanced thermal conductivity, showing that nanotube-based composites could be useful not only for their potentially high strength, but also for their potentially high thermal conductivity. **Hone (2004)** further showed direct evidence of 1-D quantization of the phonon band structure while measuring specific heat of SWNTs. He also showed how addition of only 1% nanotubes to epoxy resin doubled the thermal conductivity. **Dresselhaus et al. (2005)** and **Chu and Li (2006)** reviewed characterization techniques of amorphous and nanocrystalline carbon films. **Bokobza and Zhang (2012)** also used Raman spectroscopy for extensive characterization of MWCNTs and of MWCNTs/rubber composites. Raman spectra of bundled and dispersed multiwall carbon nanotubes were measured and all the Raman bands of the carbon nanotubes were seen to shift to higher wavenumbers upon debundling due to less intertube interactions.

The electronic structure of graphene was captured in its Raman spectrum by **Ferrari et al. (2006)** with clear number of layers. The D peak second order was seen to change in shape, width, and position for an increasing number of layers, reflecting the change in the electron bands via a double resonant Raman process. The G peak down shifted slightly. Later disorder, electron-phonon coupling, doping and non-adiabatic effects were also included **[Ferrari 2007]**. He proposed Raman spectroscopy to be an efficient tool for monitoring number of layers, quality of layers, doping level and confinement in graphene nanostructures. Years later in 2013, **Ferrari and Basko (2013)** continued the work further and reviewed the state of the art, future directions and open questions in Raman spectroscopy of graphene. Various physical processes like different types of resonance at play, role of quantum

interference etc. had been described. **Klar et al. (2013)** studied the Raman scattering efficiency of the G and 2D peaks in graphene. The study included three types of substrates: silicon covered with 300 or 90 nm oxide, and calcium fluoride (CaF_2). On Si/SiO*x*, the areas of the G and 2D peak showed a strong dependence on the substrate due to interference effects, while on CaF_2 no significant dependence was detected. They showed how the Raman scattering efficiency of graphene changes with the number of layers, the type of substrate, and the incident laser frequency. In addition, the authors highlighted that the Raman intensity of graphene was strongly modulated by the Si/SiO_x substrate, as confirmed by depositing graphene on a different substrate (CaF_2).

Sumant et al. (2007) presented a comprehensive study of surface composition and nanotribology for ultrananocrystalline diamond UNCD surfaces. X-ray photoelectron spectroscopy and Auger electron spectroscopy determined the surface chemical composition and verified the composition and bonding configuration. Nanoscale topography and nanotribological properties were studied through quantitative atomic force microscopy. Friction was substantially reduced demonstrating a direct link between the surface chemistry and nanoscale friction. **Sun et al. (2011)** on the other hand, fabricated polycrystalline Si nanowires with silver assistance by electroless deposition and characterized the chemical composition and bonding on the surface of silicon nanowire arrays by Fourier Transform Infrared spectroscope and X-ray photoelectron spectroscope. The photoluminescence spectra of silicon nanowires showed red light emissions centered around 700 nm. Due to the passivation effect of Si dangling bonds by concentrated HNO_3 aqueous solution, the photoluminescence intensities improved by 2 times. The influences of surface chemical states on the wettability of silicon nanowire arrays were also studied. The super-hydrophobic properties of the as-etched silicon nanowire sample were attributed to both the rough surface composed of aligned nanowires, and the hydrophobic state characterized by Si–Ag and Si–H bonds. When these bonds were replaced by Si = O, Si–O–Si, and Si–OH bonds, the HNO_3-treated silicon nanowire arrays presented superhydrophilic properties.

2.6 Concepts of soft computing in prediction/estimation

Although soft computing techniques, such as artificial neural networks (ANNs) and fuzzy logic, etc., have been successfully applied for predicting and optimizing various processes starting from machining to modeling, yet the cases utilizing them in heat transfer associated problems are few. Some of the works, which are close to, if not totally similar to our case

study, have been mentioned here. **Diaz et al. (2001)** controlled the temperature of air passing over a heat exchanger by simulating the time-dependent behavior of a heat exchanger working between a closed hot water and an open air loop, with ANN. A methodology was proposed for training and prediction of the dynamic behavior of thermal systems with heat exchangers and then an internal model scheme was developed for the control of the over-tube air temperature with two ANNs, one to simulate the heat exchanger and another as controller. Comparison of results with standard PI and PID controller showed that AI based controller allowed the system to reach steady-state operating conditions in regions where the PI and PID controllers were not able to perform and they were less oscillatory as well. Study showed neural networks as powerful tools for thermal control. **Denai et al. (2004)** studied modeling and control of complex systems like nonlinear knee-joint dynamics, with soft computing approaches namely ANFIS. **Scalabrin et al. (2006)** studied the local representation of flow boiling heat transfer at varying fluid dynamics conditions along a tube through a newly proposed modeling technique based on neural networks. They showed how flow boiling heat transfer model was not intrinsically flow pattern dependent. **Wei et al. (2007)** built two adaptive network-based fuzzy inference (ANFIS) models ANFIS-GRID, and ANFIS-SUB to predict injection profiles during oil field developments. They compared the performance of resultant FIS and studied the effect of parameters and data quality on the performance. FIS were generated and tested using training and testing data from that data set. ANFIS-GRID outperformed ANFIS-SUB due to its simplicity in parameter selection and fitness in the target problem. In a similar fashion, **Caydas et al. (2009)** developed an ANFIS model for prediction of white layer thickness and the average surface roughness of a wire electrical discharge machined surface. In the authors' opinion, the ANFIS model could greatly improve the process responses. **Esen and Inalli (2010)** predicted the performance of a vertical ground source heat pump system with ANN and ANFIS. Experimental performances were performed to verify the results from the ANN/ANFIS approaches and the appropriateness of ANFIS in quantitative modeling of the heat pump systems was claimed. **Kishor and Das (2010)** studied applicability of soft computing techniques, swarm-intelligence based neural network, and adaptive fuzzy models in the prediction of boiling heat transfer coefficient (HTC). Pool boiling heat transfer coefficient of liquids on copper-coated heating tubes over a wide range of pressure conditions was experimentally computed and the prediction results were compared with the experimental ones. The model predicted HTC with a maximum error of ± 5%. Use of higher MFs (i.e., six) enhanced the prediction accuracy in relation to the results

obtained with MFs of two for fuzzy modeling. Quite notably, the performance of the ANFIS model significantly reduced from atmospheric to sub-atmospheric conditions. Similar study for prediction of building energy consumption with ANFIS was carried out by **Ekici and Aksoy (2011).** Outputs compared with numerically calculated results with finite difference approach showed that ANFIS predicted energy requirements of different buildings with an accuracy of 96.5% and 83.9% for heating and cooling respectively.

An online tool wear monitoring system based on ANFIS was proposed by **Rizal et al. (2013)** to predict tool wear during a turning process. Cutting speed, depth of cut, feed rate etc. were inputs, and flank wear value for the cutting edge was an output of the model. Results generated by ANFIS model had error of minimal 2.30% and 5.08% in minimum and maximum average flank wear respectively. Similar application of ANN, ANFIS was done by **Azari et al. (2014)** to predict the applied force during the radial forging process with a view to predicting die force to prevent die damage and material waste. Obtained results were compared with the multiple regressions (MR) method. Based on ANN, reduction in cross-section came out as a significant variable for the model, while according to ANFIS and MR, the initial billet temperature was the most effective input. ANFIS model came out to be the fittest among all. ANFIS with Gaussian member function was used by **Nayak et al. (2014)** to predict cutting forces in milling during conventional machining of mild steel. An ANN model with 4 neurons of input layer, 20 neurons of hidden layer, one neuron of the output layer and Levenberg- Marquardt BP algorithm as train process was used to predict heat transfer coefficient for forced convection over aluminum and steel plates by **Mert and Arat (2014).** On a similar trend, **Zhu and Wu (2014)** developed a damage detection method based on structural dynamic vibration data to fast assess structural fault for short-term monitoring by integrating ANFIS with interval modeling technique. A high degree of accuracy for the prediction of the structural response was assured by ANFIS and interval modeling technique to effectively extract damage characteristics. **Rath et al. (2015)** suggested an alternative to the traditional mathematical models based on plane homogeneous plastic deformation theory used for prediction of roll force during hot rolling process for model based automation of plate mills. The response of gauge control hardware was highly dependent on the accuracy of prediction of roll force but the traditional method was based on many simplified assumptions which were not valid for actual industrial application. This suggested alternative model, based on ANN took roll gap of previous pass, roll gap of current pass, rolling temperature, rolling speed, plate width, and pass number as input and roll force as the output. Feed

forward network was chosen as ANN structure and back propagation algorithm with variable learning rate and conjugate gradient optimization of cost function was chosen as network training methodology. The model was found to be highly accurate with r-square value about 0.94.

2.7 Research at IIT Guwahati

The research in the domain of heat flux measurements and thin film gauges started in the year 2010 by **Sahoo and Peetala (2010)** where they attempted to infer transient surface heat flux from the temperature history using one dimensional heat conduction model. A nickel sensor was used to record the experimental temperature data for a supersonic flight test. Curve fitting techniques like piecewise linear fitting of temperature data were used to recover the actual experimental signal with fair agreement between the original and produced data. Although for longer times, they observed better fitting with cubic spline method compared to linear or polynomial fitting of data. That temperature data obtained from various techniques were used in one dimensional heat conduction modeling and transient surface heat fluxes were predicted. The following year, **Sahoo and Peetala (2011)** extended the study for measuring convective surface heating rates on aerodynamic surfaces which mostly included unsteady flows resulting in temperature variation in the body. In addition, the effect of sensor thickness on surface heat flux measurements during the flight measurement was also investigated. For that, two methods were used to infer the surface heat flux viz. inverse methods using analytical solutions and control volume approximations. The surface heating rates predicted via inverse method from the measured temperature histories used similar heat transfer modeling using one-dimensional heat conduction. No significant change in surface heat flux was observed between inverse and thin film analysis. However when the thickness of nickel film was increased by 100 times, the peak surface heat flux also increased by 20%.

In the same year, **Kumar et al. (2011)** prepared platinum thin film sensors and designed radiation based calibration experiments with step heat load applied using laser light of known wattage. Later, the recorded transient temperature data were processed for estimating laser wattage numerically with ANSYS (v. 14.5) solver. During the experimental time scale, temperature rose instantaneously in the initial period and later with a consistent parabolic trend all throughout. The parabolic rise of temperature plots ensured the analogous behavior with respect to the use of platinum thin film gauges in shock tunnel applications. The temperature histories obtained using experiment, finite element simulation (FEM) and

analytical techniques showed similar results. However, for laser based experiments, a delay was observed for rise in surface heat flux. The minor difference in signals obtained from the simulation and the experimental signal were attributed to the use of standard thermal properties for platinum and pyrex materials during simulation. Later in that year, **Kumar and Sahoo (2011)** tried to enhance thermal properties of platinum gauges with nanofluids. They observed thermal diffusivity getting doubled with an addition of 35% mass fraction of CNT in platinum. Authors concluded that small amounts of CNTs dispersed in platinum could help in achieving more sensitive gauges. A similar conduction based calibration was designed in the next year with the same platinum gauges by **Kumar et al. (2012).** A constant power supply source was used to apply constant heat flux to one end of an insulated copper rod while the other end was exposed to surroundings creating a constant temperature gradient along its length, all other surfaces being completely insulated. This steady state heat flux was used as the source of known conduction heat flux applied to thin film gauges. The recovered signals for temperatures and surface heating rates matched well within a reasonable uncertainty of ± 2%. These platinum gauges were refabricated with both pyrex and macor as substrates in 2014 by **Kumar and Sahoo (2014).** Thickness of the film was maintained around 0.1μm - 1.0μm to ensure same temperature on the surface of the substrate and on the film. However, this time coaxial thermocouple (K-type) was also prepared. The analysis of variation of surface temperature histories for pyrex, macor, chromel-alumel materials as a function of the substrate depth for several different testing time intervals were plotted. It was noted that for a substrate base temperature to surface temperature ratio of less than 1%, the substrate thickness must be at least 10mm for relatively longer testing time (more than 10s). Substrates exceeding this value gave satisfactory result for short durations testing and satisfied the semi-infinite assumptions for heat conduction modeling. Heat transfer measurement at stagnation point was predicted using the sensors and a blunt nose test model with an in-house fabricated experimental set-up to generate heated air jet at sonic velocity. Unlike in any other cases, for stagnation point based experiments a delay of 1ms was observed for rise in surface heat fluxes.

2.8 Literature closure

From the concise review of the different works done by various researchers in thin film gauges, following summary could be drawn.

- For the satisfactory performance of a gauge it is very important to obtain expertise in fabricating them.
- TFGs are modeled well with semi-infinite assumptions and the methods described for extracting heat flux from temperature signal using one-dimensional heat conduction in semi-infinite gauges, are efficient.
- There is a need for improvement of sensitivity of the gauges and addition of nanoparticles to base material might help in doing so. The best combination of nanomaterials with base material is not studied yet. This would help in measuring lower heat fluxes with higher accuracy.
- From the research done at IIT Guwahati it is seen that implementation of the fabricated gauges in practical situations are yet to be carried out. Quantification and qualification of nanocomposite gauges are yet to achieve. In addition, an attempt could be made for multilayer gauges and their comparison with monolayer gauges could provide better insight about TFGs and their applications.

Although a lot of work has been carried out by different researchers in the area of thin film gauges, yet a lot can be done in this field for improvement of its sensitivity, performance etc.

2.9 Objective of the Thesis

The main objective of the thesis is fabrication of quality Thin Film Gauges for use in transient environments. In order to achieve the specified objective, the following sub objectives have been decided upon:

- **Fabrication:** The coating of thin films of conductive metals with solid/power form or ink/paste form on the insulating ceramic substrate is possible in an effective manner, with appropriate skills. In this direction various methods of film deposition can be attempted i.e. hand-painting/vacuum-coating/foil-laminating or etching type (*Chapter 4*). Also, fabrication of multi-layer type of TFGs can be attempted which can be considered as a new design in this area (*Chapter 7*).

- **Characterization:** Investigating the compatible nanoparticles for base metals of TFGs that can lead to a possible enhancement of sensitivity or TCR of the fabricated gauges and establishing factors responsible for such enhancement (*Chapter 4*). This calls for characterization of the nanocomposites viz. analysis of crystal structures of sample films, their surface morphology study etc. by X-ray diffraction (XRD), field emission scanning electron microscopy (FE-SEM), and scanning electron microscopy (SEM), energy-dispersive X-ray spectroscopy (EDX), etc. Moreover, quantification of enhancement by varying design parameters could also be included (*Chapter 7*).

- **Calibration techniques:** While performing real time experiments with TFGs, it is also necessary to have proper calibration methodologies which include exposing the TFGs in heating environments (*Chapter 5*).

- **Numerical study:** Numerical modeling of TFGs for prediction of surface heat flux from measured transient temperatures for variety of applications is already studied and appropriate modeling has been reported. Easier and comparatively faster alternatives could be a well sought objective in this regard (*Chapter 6*).

Chapter 3

Preliminary study on modeling of TFG

3.1 Introduction

A semi-infinite solid is an idealized body having a single plane surface and extends up to infinity in all other directions. In general, anybody can be considered to be semi-infinite if the temperature change occurs near a single surface only and the changes in other surface are small enough or far away to effect the variation in that particular surface during the time of observation. The thin film gauges under consideration are also applicable to semi-infinite assumptions. In order to check for what time scales the semi-infinite assumption is valid in these gauges, a numerical study is carried out at the onset in both two dimensions (2D) and three dimensions (3D).

3.2 Thermal penetration study (2D)

3.2.1 Geometry, mesh and boundary conditions

The thin film gauge is considered to have a two dimensional planar geometry with a film length of 10 µm, substrate length of 10 mm and width (diameter in 3D) of 6 mm. The gauge is subjected to constant heat load on the top. The geometry used is displayed below (Fig. 3.1).

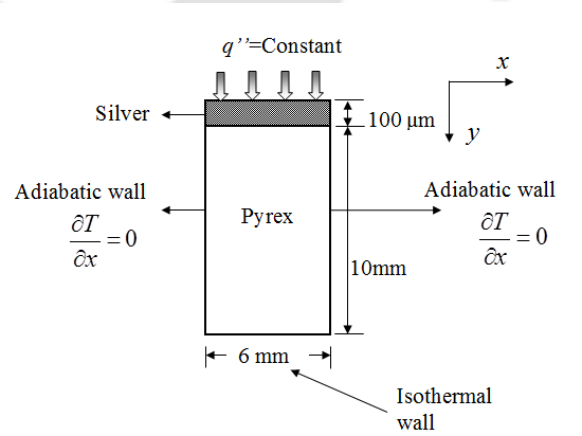

Fig. 3.1 Schematic of TFG model for semi-infinite validation

A structured grid of size 100×100 and 100×10 has been used for the substrate and the film, respectively. The domain is accepted as a result of grid independence study. The substrate is

divided into equal increments in both x and y directions. However, in case of film, the increment in y direction is kept comparatively small. A total of 11000 nodes have been used to represent the whole system. The nodal points in x and y direction are indicated by i and j , respectively. The two-dimensional unsteady heat conduction equation is solved to determine the temperature at any of these nodal points (Eq. 3.1). The computational mesh for thin film gauge and nodal points are shown in Fig. 3.2. The boundary conditions used for gauge are described above in Fig. 3.1.

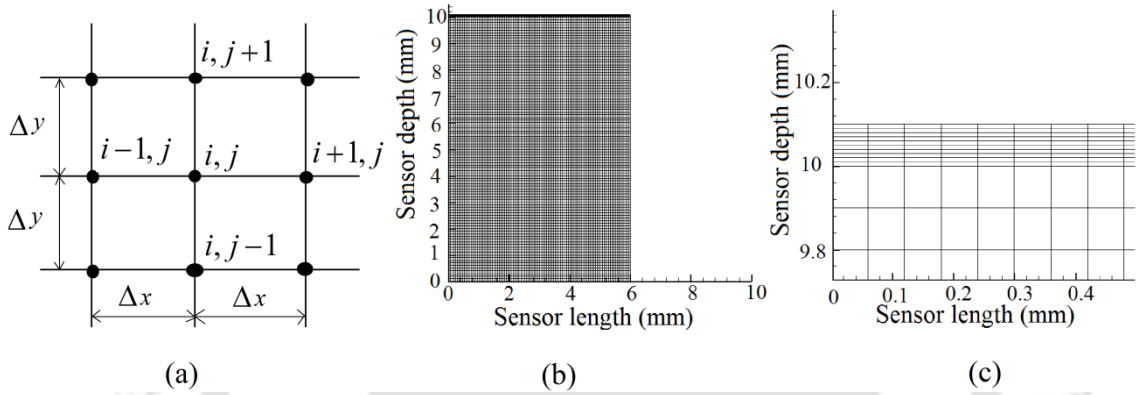

Fig. 3.2 (a) Nodal points for computation grid (b) mesh (c) magnified mesh

The 2D unsteady heat conduction equation is used to describe the temperature field in the sensor.

$$\frac{\partial T}{\partial t} = \alpha' \left(\frac{\partial^2 T}{\partial x^2} + \frac{\partial^2 T}{\partial y^2} \right) \tag{3.1}$$

Here α' is thermal diffusivity of the material. Using second order accurate central difference scheme, temperature gradients are discretized in both longitudinal and lateral directions. The discretized form of Eq. 3.1, which is an algebraic representation of the partial differential equation (PDE), is solved at every node. However in case of steady state, the RHS of Eq. 3.1 becomes zero and thus the equation gets simplified to Laplace equation (Eq. 3.2).

$$\left(\frac{\partial^2 T}{\partial x^2} + \frac{\partial^2 T}{\partial y^2} \right) = 0 \tag{3.2}$$

Crank Nicholson scheme has been used for time integration with successive over relaxation (SOR) accelerated convergence keeping $\omega_{opt} = 1.5$ since Crank Nicholson scheme does not

impose restriction on the value of time step (Δt) . A second order central difference scheme is used for spatial discretization. Given the data states on all the walls of the gauge, the temperature contour is obtained. In the present analysis, thermal properties of both the materials viz. silver and pyrex are assumed to be constant. The thermal properties of silver and pyrex are considered as mentioned in Table C.1 (*Appendix C*) during the analysis. Convergence criterion of 10^{-6} has been used. Initial temperature throughout the gauge is considered at 298K. The simulation took 1655 number of iterations to converge during steady state. During transient analysis, value of time step (Δt) is fixed at 0.001 s. The results obtained are discussed below.

3.2.2 Results and Discussion

The variations of temperature along lateral and longitudinal directions of the thin film gauge under steady state analysis have been plotted in Fig. 3.3(b). It is clear from the plots that there is no variation along the lateral direction whereas temperature decreases linearly along the depth of the substrate. Thus, heat can be assumed to flow along the depth of substrate due to absence of significant temperature gradient in lateral direction. Therefore, one-dimensional heat conduction assumption in thin film gauges gets validated as reported in the literature [Talib et al. 2005].

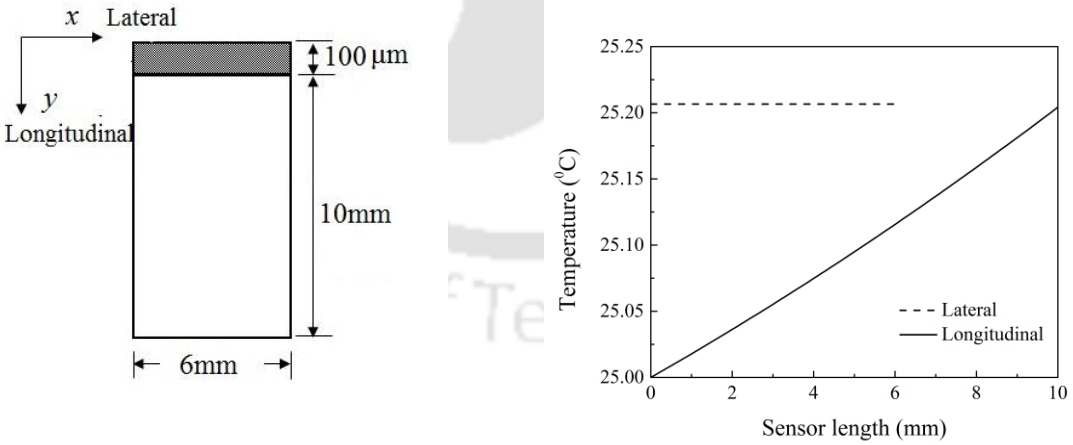

(a) (b)

Fig. 3.3(a) Lateral and longitudinal direction in sensor (b) variation of temperature in both direction during steady state

Further, the study of the thin film gauge is extended in transient environment for four cases (for a total time of 1 ms, 10 ms, 100 ms and 1 s). The variations of temperature within the film and along the depth of substrate are compared for all the time scales ranging from 1 ms

to 1 s (Fig. 3.4). The thermal penetration depth in the substrate during these run-times has been listed in Table 3.1.

Table 3.1 Thermal penetration depth in substrate measured in the direction from film surface to the core

Simulation time (ms)	Thermal penetration depth (mm)	Percentage of thermal penetration (%)
1	1.3	12.87
10	1.7	16.83
100	2.4	23.76
1000	5.1	50.49

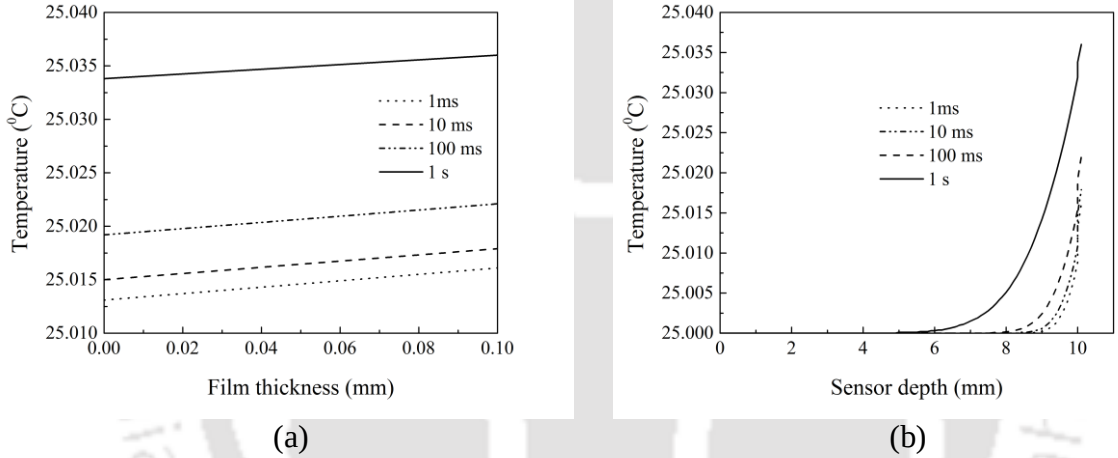

(a) (b)

Fig. 3.4 Variation of temperature (a) within the film (b) within substrate during different run-times of transient analysis

As could be seen from the plots, no significant variation of temperature within the film is observed even for 1 s time scale (Fig. 3.4(a)). In other words, the variation is so negligible (of the order of 0.0008 ºC) that it has no effect on the substrate surface temperature history. All the plots reveal that the maximum temperature attained and depth of penetration increases with increase in the time of measurement. However, it is low enough not to violate the semi-infinite assumption of the gauge. The temperature contour shown in Fig. 3.5, also supports the above inferences.

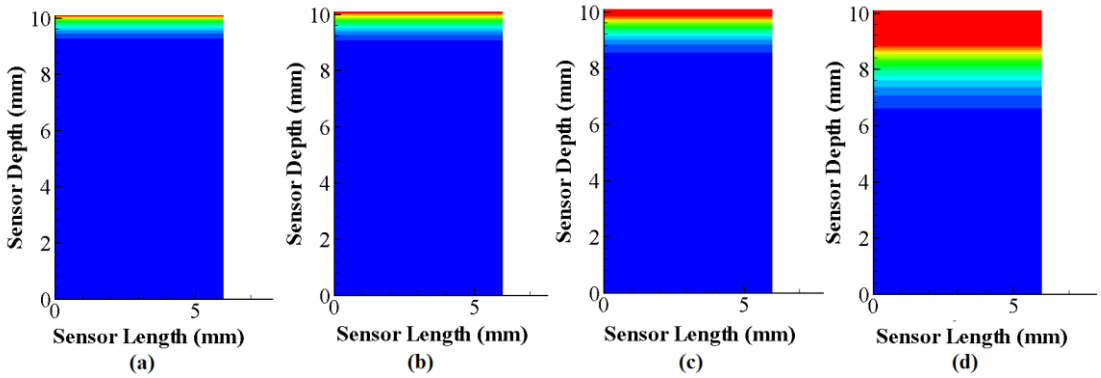

Fig. 3.5 Temperature contour showing heat penetration during different run-times (red being highest and blue being lowest)

3.3 Numerical simulation using ANSYS Thermal Transient (3D)

Similar computational analysis has been carried on the TFG using commercial ANSYS (Thermal Transient v. 14.5) package with an objective to re-analyzing the thermal penetration during experimental run-times. Simulation is carried out for similar simulation time as used in the 2D study.

3.3.1 Geometry, mesh and boundary conditions

As the film thickness is very small compared to the thickness of the substrate, special care has been taken to generate a uniform mesh in the substrate core and the film surface. Nodes and elements used for 3D simulations are 2518 and 330 respectively. MULTIZONE meshing has been applied (both cases) in the film as well as the substrate keeping in view that the solution converges to the nearest possible value. Boundary conditions are specified in the model as shown in Fig. 3.1.

3.3.2 Results and discussion

Fig. 3.6-3.7 shows the geometry, meshing and temperature contour for three-dimensional (3D) analysis of a typical TFG. The longitudinal variation (along depth) of temperature is studied for all of the simulation time and captured temperature vs. depth signal for 3D is plotted in Fig. 3.8. Temperature variation is noticed only at the vicinity of the film. The magnified view for the variation within a distance of 1 mm from surface of the gauge is shown in Fig. 3.8(b).

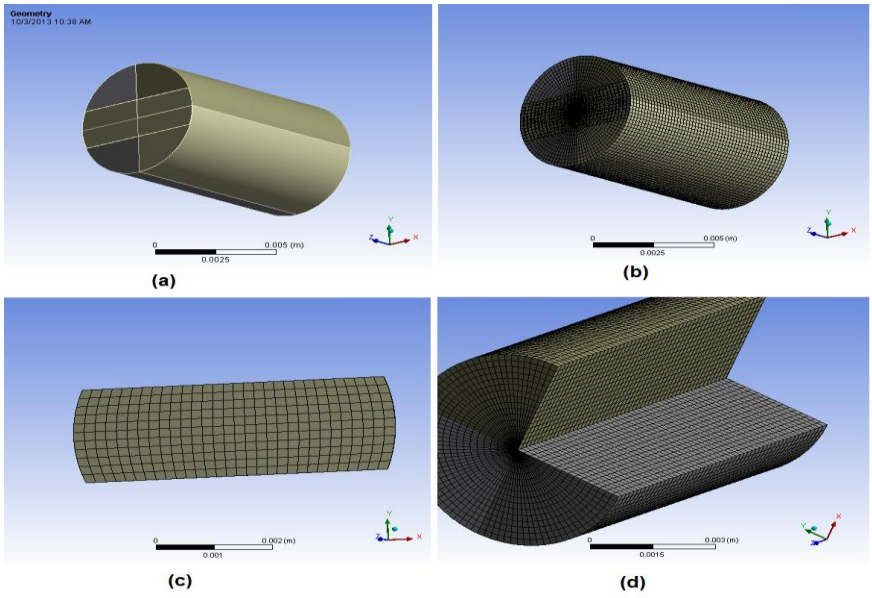

Fig. 3.6(a) Three-dimensional geometry of TFG (b) Multizone meshing (c) mesh pattern over the film (d) mesh pattern in the substrate core

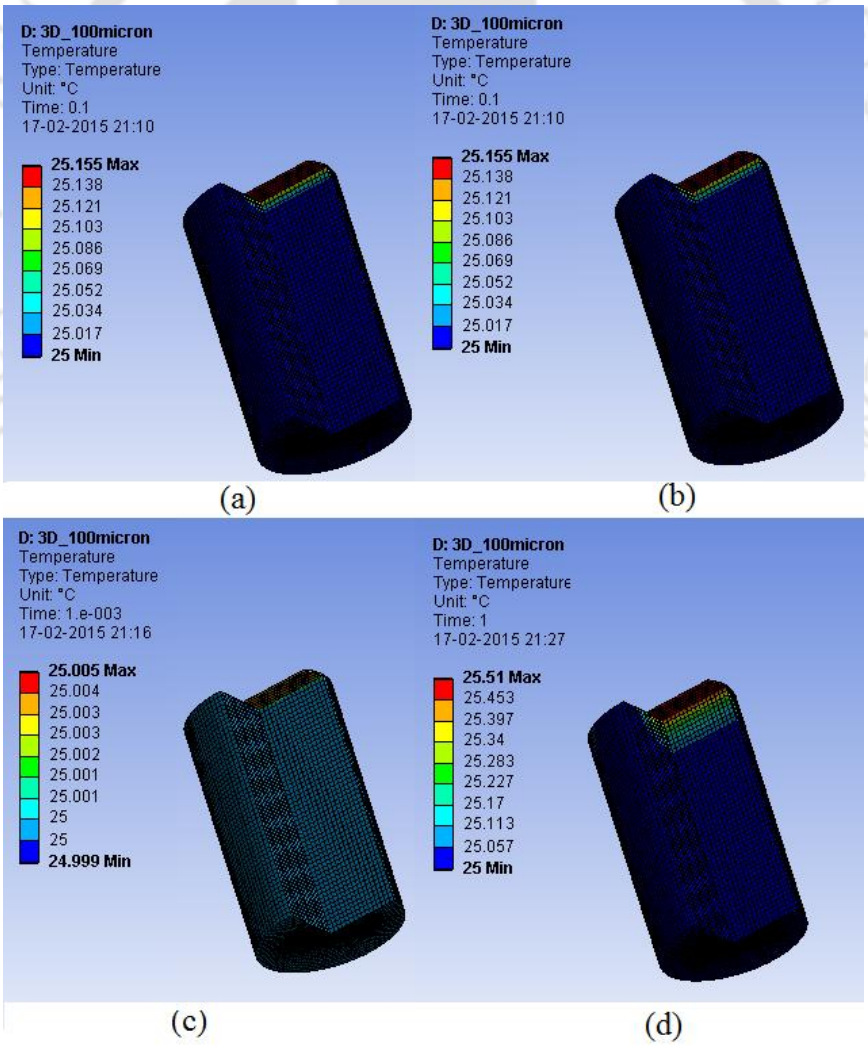

Fig. 3.7 Temperature contour for (a) 10 ms (b) 100 ms (c) 1 ms and (d) 1 s

Fig. 3.9 shows the radial variation of temperature for 3D at the gauge surface for two cases: along the film surface and across the film surface. Temperature variation for all of the simulation times are compared. Across the film surface, the curve shows a pattern where it first increases and then decreases until a stable temperature is reached. While along the film, temperature remains almost constant revealing the absence of any temperature gradient and thus assuring 1D heat transfer analysis for the thin film gauge model. However the peak attained by temperature is more in case of 1 sec simulation time.

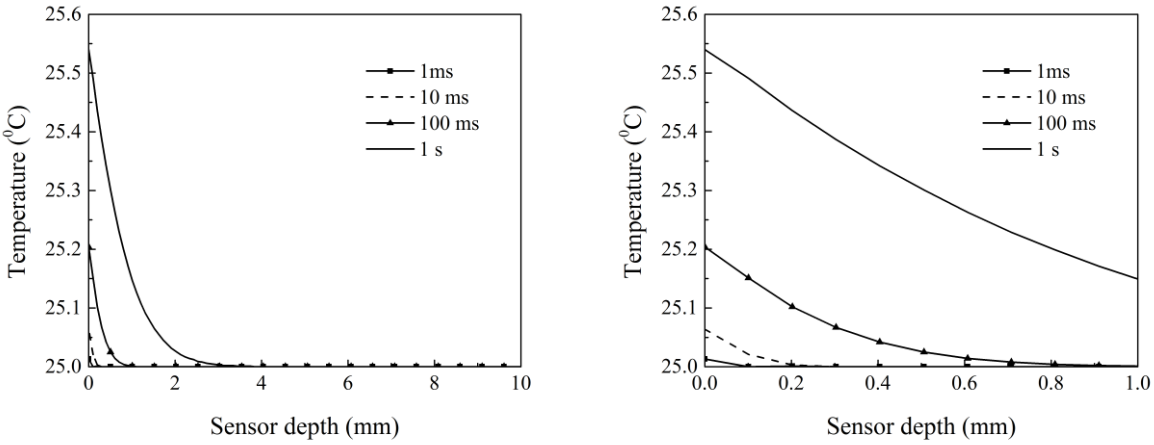

Fig. 3.8(a) Comparison of variation of temperature over substrate depth for different simulation time (b) magnified view of temperature variation (up to 1 mm from top)

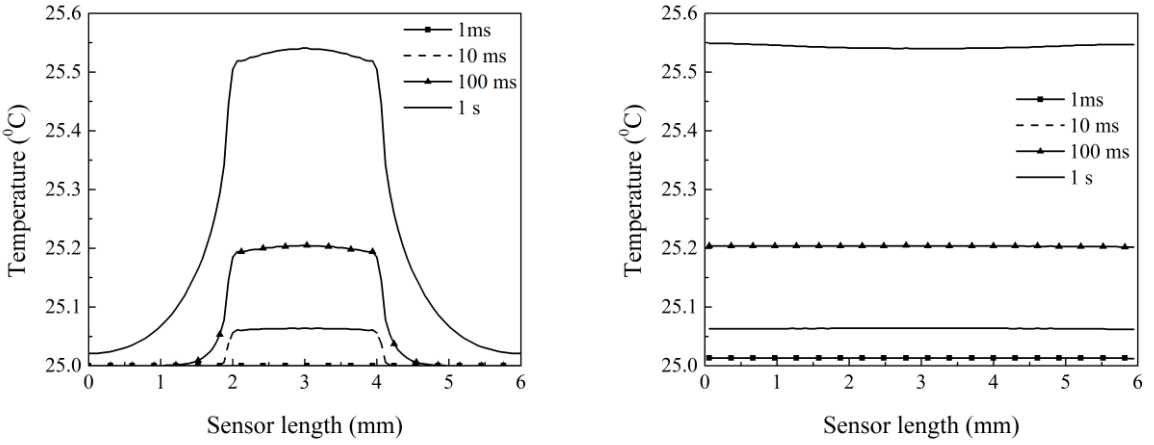

Fig. 3.9(a) Radial variation of temperature of thin film for different simulation time (a) along the thin film and (b) across the thin film

3.3.3 Validation of Numerical Model

In order to check the validity of the ANSYS model, the temperature signal obtained is fed to the MATLAB (v. 2012b) code, which uses inverse method of heat conduction for calculation of heat flux from a given temperature signal using [Taler 1996]. The method for extraction of heat flux from temperature is described in subsequent section. The temperature signal obtained by ANSYS simulation for 3D geometry under the simulation times of 1 ms to 1 s are given as input to the code of cubic spline [Taler 1996]. The method first generates a cubic spline approximated temperature signal which clearly overlaps the original imported signal as shown in Fig. 3.10(a). Now, this new approximated spline temperature signal is used to extract the heat flux signals as shown in Fig. 3.10(b). It is evident from these two graphs (Fig. 3.10) that for 1 ms and 1 s simulation time there is large deviation of heat flux value from the input of 1000 W/m^2 in comparison to simulation times of 10 ms and 100 ms. This might be due to fact that in 1 s heat gets enough time to penetrate through the sensing material and thus losses cannot be considered negligible anymore. On the other hand, 1ms time is way too small for the sensor to correctly predict the heat flux accurately.

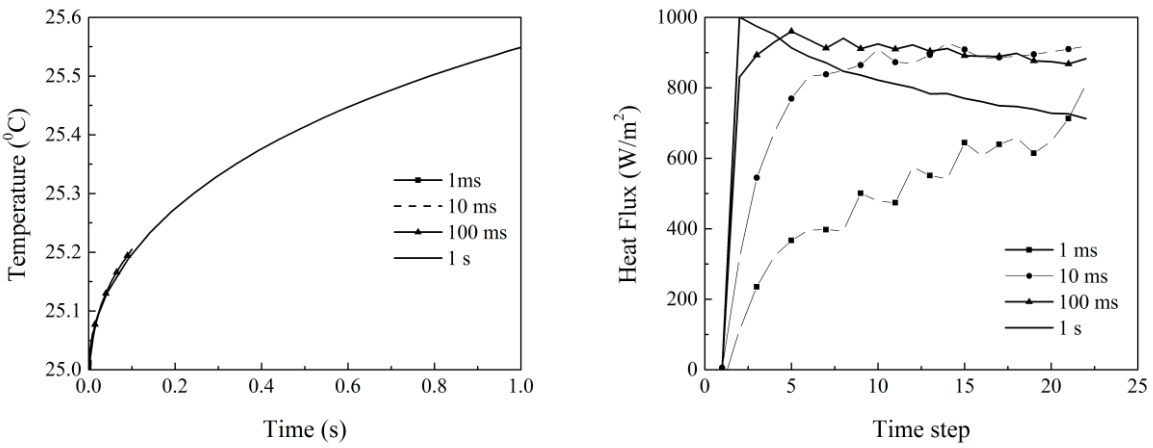

Fig. 3.10(a) Temperature history as recorded by gauge subjected to constant heat flux during various time scales (b) heat flux estimated from corresponding temperature history

3.4 Analytical Modeling of Heat Transfer Gauges

The semi-infinite gauge under consideration is shown in Fig. 3.11 and as is evident for a semi-infinite gauge there is no difference in temperature at the surface and at the interface of sensing film and substrate. The wall heat flux can be determined by unsteady solutions of the heat conduction inside the substrate.

Considering the substrate to be a semi-infinite solid (Fig. 3.11) maintained at initial temperature T_i, if it is suddenly exposed to a constant surface heat flux q_s, and the temperature distribution in the solid is assumed to be a function of time, then the temperature distribution may be used to determine the heat flux at any position x in the solid.

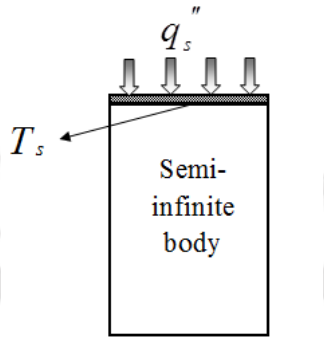

Fig. 3.11 TFG as semi-infinite gauge

As described [Holman 1986], differential form of temperature distribution may be written as follows:

$$\frac{\partial^2 T}{\partial x^2} = \frac{1}{\alpha'}\frac{\partial T}{\partial t} \tag{3.3}$$

The initial and boundary condition becomes:

$$T(x,0) = T_i \text{ and } q_s = -k\frac{\partial T}{\partial x}\bigg|_{x=0} \tag{3.4}$$

The solution is given by:

$$T - T_i = \frac{2q_s\sqrt{\frac{\alpha' t}{\pi}}}{k} e^{\left(\frac{-x^2}{4\alpha t}\right)} - \frac{q_s x}{k}\left(1 - erf\left(\frac{x}{2\sqrt{\alpha' t}}\right)\right) \tag{3.5}$$

Therefore, at the surface where x=0, the temperature is given by,

$$T_s = T_i + \left(\frac{2q_s}{k}\right)\sqrt{\frac{\alpha' t}{\pi}} \tag{3.6}$$

A temperature signal is generated in MATLAB (v. 2012b) using Eq. 3.6. A constant heat flux of 1 kW/m^2 is applied for total time duration of 1 s. The initial temperature of the substrate is considered to be 300 ºC. The properties viz. thermal diffusivity (α') and thermal conductivity (k) used in the equation are the properties of the substrate material. The time duration of 1 s, is then divided in to a thousand steps each equal to 1 ms. The temperature history is then obtained by calculating temperature at all the time steps. The temperature signal generated is shown in Fig. 3.12.

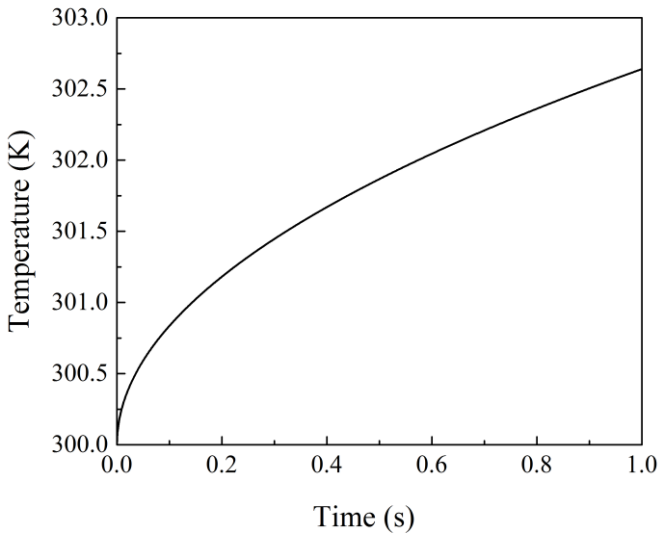

Fig. 3.12 Temperature history generated for a constant heat flux of 1 kW/m^2 (Eq. 3.6)

Duhamel rewrites Eq 3.6 to relate heat flux (q_s) and surface temperature (T_S) in form of an integral which is named as Duhamel's superposition integral:

$$q_s = \sqrt{\frac{\rho c k}{\pi}} \int_0^t \left(\frac{dT_s}{dt}\right) \frac{1}{\sqrt{t-\tau}}\, d\tau \tag{3.7}$$

where, ρ, c and k are the density, specific heat capacity and thermal conductivity of the substrate material, T_s is the surface temperature from TFG and t is the time. Here, the substrate thermal properties are treated as constant. This equation (Eq. 3.7) has been used throughout the thesis wherever heat flux has been calculated from transient temperature history.

3.4.1 Temperature Discretization

For estimating the surface heat flux, the temperature data needs to be discretized first. Out of various methods available, here only two of them are discussed viz. least square method and cubic-spline method.

In "Least Square (LS)" method, the temperature is considered at discrete time steps and is assumed to be a polynomial function of time [Taler 1996]. This can be represented mathematically as:

$$\left[T(t)\right]_{LS} = \sum_{i=0}^{m} A_i t^i \tag{3.8}$$

where, A_i are the coefficients in the polynomial equation. The given temperature history is used to determine these coefficients which are then used in following equations (Eq. 3.11) to determine the heat flux.

In "Cubic Spline (CS)" method, the temperature data are considered in small steps and cubic-spline approach is adopted for discretization. Here, unlike Least Square, the experimental temperature is represented by a third order spline [Taler 1996]:

$$\left[T(\tau)\right]_{CS} = C_{1,i} + C_{2,i}(\tau - \tau_i) + \frac{1}{2}C_{3,i}(\tau - \tau_i)^2 + \frac{1}{6}C_{4,i}(\tau - \tau_i)^3 \tag{3.9}$$

$$\tau_i \le \tau \le \tau_{i-1,} i = 1,2,.....M$$

where, $\tau = S_t t$ is scaled time and S_t is the scaling factor. Here, the scaling factor is considered as unity.

The co-efficient are calculated as follows:

$$C_{n,i} = dT^{n-1}(\tau_i)/d\tau \tag{3.10}$$

3.4.2 Heat Flux Estimation

The equations that are used to calibrate RTDs and to calculate the heat flux from the temperature history are based on three main assumptions.

The assumptions are:

1. The heat transfer is one-dimensional.

2. The substrate is semi-infinite.

3. The measuring surface film has a negligible effect on the heat conduction.

The third assumption is actually an approximation which introduces an error in the deduced heat flux. To calculate the heat flux accurately, the RTD must follow the one-dimensional theory as best as possible. For that, the substrates on which the thin film gauges are mounted must be thick enough so that the heat transfer into the substrate is similar to that into a semi-infinite solid. But, the film deposited on the substrate surface always affects the surface temperature history, however small it might be. Therefore this effect should be taken into consideration or else erroneous results may be encountered.

Using the equation (Eq. 3.8), the temperature data shown in Fig. 3.12 is expressed as closed form solution. Subsequently, the surface heat flux for Least Square is calculated (Eq. 3.11) using the methods given by Jan Taler [Taler 1996], Schultz and Jones [Schultz and Jones 1973] and W.J. Cook, E.J. Felderman [Cook and Felderman 1966]. However this method is of comparatively low accuracy.

$$q(t) = u\left(b_1 + \sum_{i=2}^{m} b_2 b_3 \right) \tag{3. 11}$$

$$u = 2\sqrt{\frac{\rho c k}{\pi}};$$

where,

$$b_1 = A_1\sqrt{t};\ b_2 = iAt^{\frac{(2i-1)}{2}};\ b_3 = \left[1 + (i-1)! \sum_{k=1}^{i-1} \frac{(-1)^k}{(2k+1)k!(i-1-k)!} \right]$$

when $m \le 5$, then the method is known as piecewise linear interpolation method.

The heat flux for the temperature data given by Eq. 3.9 is calculated using the following formula [Taler 1996].

$$q(\tau_{M+1}) = \left\{ 2\sqrt{\frac{\rho c k}{\pi}} \sum_{i=1}^{M-1} V_i \left(P_i^{\frac{1}{2}} - R_i^{\frac{1}{2}} \right) - \frac{W_i}{3} \left(P_i^{\frac{3}{2}} - R_i^{\frac{3}{2}} \right) + \frac{C_{4,i}}{10} \left(P_i^{\frac{5}{2}} - R_i^{\frac{5}{2}} \right) \right\} \sqrt{S_t} + 2\sqrt{\frac{\rho c k}{\pi}} \left(V_M P_M^{\frac{1}{2}} - \frac{W_M}{3} P_M^{\frac{3}{2}} + \frac{C_{4,M}}{10} P_M^{\frac{5}{2}} \right) \quad (3.12)$$

where, $M = 1, 2, \ldots\ldots\ldots, J-1$ and,

$$P_i = \tau_{M-1} - \tau_i;\ R_i = \tau_{M+1} - \tau_{i+1};\ F_i = C_{1,i} + C_{2,i} P_i + \frac{C_{3,i}}{2} P_i^2 + \frac{C_{4,i}}{6} P_i^3;\ V_i = \frac{dF_i}{d\tau_{M+1}};\ W_i = \frac{d^2 F_i}{d\tau^2_{M+1}}$$

The average error of prediction turns out to be 26% in terms of Least Square method whereas in case of Cubic Spline it is only 13%.

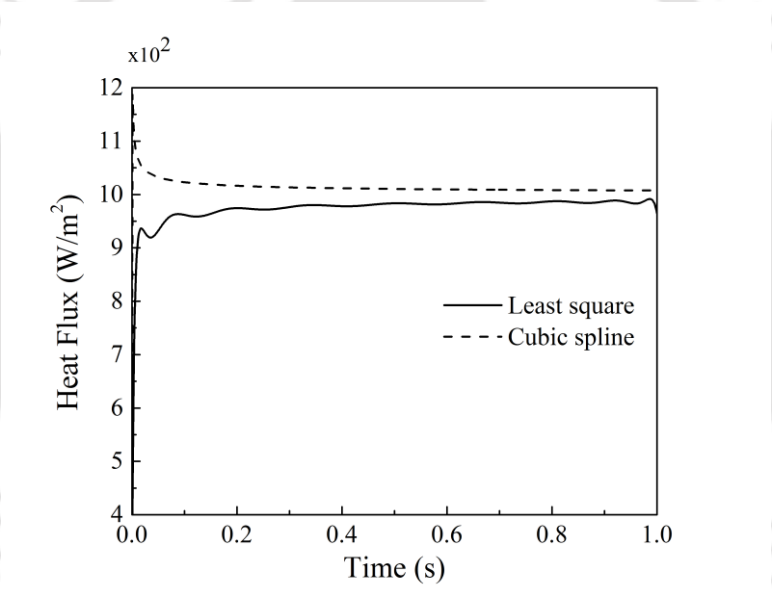

Fig. 3.13 Comparison of surface heat flux by various methods

Under certain conditions, the cubic spline regression can be shown to be a special case of the restricted least-square method as discussed by Buse and Lim [Buse and Lim 1977]. However for all practical purposes, say for example the temperature data collected within a shock tunnel during the occurrence of a shock, there will always be some noise attached to the raw signal. So, the use of time series cubic-spline fitting of temperature data would be more appropriate in such circumstances. When the time interval increases, cubic-spline technique does not consider all the data points. Rather, it takes two possible nearby points and fits a curve. This procedure is repeated throughout the domain, which is not the case in least square

fitting technique. In least square method, the entire data is considered altogether and a best fit curve is used to fit into the data.

In the present study, the temperature data is generated for a constant heat flux with fixed values of thermal properties of the materials. Hence, it is expected that both the technique will yield similar result (Fig. 3.13). For similar reasons, cubic spline method has been used elsewhere in this thesis wherever there is a need for heat flux reduction from temperature. Since the thermal penetration distance during experimental run times is small compared to the linear dimension of the gauge, the system can be modeled by considering unsteady, linear conduction of heat in a one-dimensional semi-infinite solid.

3.5 Conclusion

This study was mainly done to find out required dimensions of the gauge for valid assumption of semi-infinite gauge theory and also to obtain until what experimental time scales, semi-infinite assumption in the gauges will hold true. A preliminary computational study for modeling thermal penetration depth of TFG is done in 2D using Crank-Nicholson scheme and the same has been repeated through ANSYS in 3D. Both studies have clear implication of no remarkable temperature variation along the lateral direction and linear decrease in temperature along the longitudinal direction (depth of the substrate). Effect of film thickness on substrate surface temperature history is neglected owing to extremely less temperature gradient within the thin film (of the order of 0.0008 ºC) and semi-infinite validation hold true till experimental time scale of 1 s which is sufficient for the transient environments under consideration. In a nut shell, since the thermal penetration distance during experimental run times is small compared to the linear dimension of the gauge, modeling the system as a case of unsteady, linear conduction of heat in a one-dimensional semi-infinite solid is justified. Prediction of heat flux from temperature signals through Least Square method incurs an error of 26 % while through Cubic Spline it is only 13 %. Thus, Cubic Spline method is used throughout the thesis hereafter.

Chapter 4

Fabrication and characterization of thin film gauges

4.1 Introduction

The fabrication of conventional metallic thin film gauges is a well-known phenomenon and a number of techniques including hand painting, physical vapour deposition, chemical vapour deposition, spin coating, etching etc. have been proposed already. Starting from material selection for gauge to completing the connections for a closed circuit, the fabrication process needs more of reasoning and justification rather than mere trial. Fabrication of these sensors needs to be carried out in a clean environment while taking precautions for various steps associated in the process. Moreover, in an attempt to complete basic needs of temperature measurement, there has to be a continuing effort to enhance its performance keeping in mind the use of gauge in harsh and short duration transient environment. This chapter discusses different types of film deposition techniques carried out in the study.

Cases involving measurement of smaller magnitude of heat fluxes (about 1 W/m^2 or less) are intricate as well as crucial. This calls for gauges with enhanced thermal properties for accurate prediction of heat fluxes. With recent developments in material science and technology, it is possible to improve the thermal, electrical properties and sensitivity of gauge material for its viable applications for such requirements. The basic advantage of higher thermal conductivity is rapid heating/cooling of a material which in turn opens more scope for accurate estimation of heat transferred. Therefore, the high-conductivity materials are always favorable for better performing TFGs. Further, nanocomposite blends of well-dispersed nanometer sized solid particles in base metal matrix in proper concentration can be a well-sought solution for performance enhancement. The research findings in this area indicate about altering thermal properties of the base metal dramatically by nanofluid/nanocomposite blends [Gan et al. 2005, Hwang et al. 2006, Sun et al. 2007, Hossain et al. 2015]. Keeping this in view, the final part of the chapter focuses on the development of a nanocomposite gauge to reflect upon the change in sensitivity and TCR change of the composite gauge from conventional ones.

4.2 Fabrication of the TFG

A typical thin film gauge is comprised of an insulator as a substrate material painted or sputtered with a higher conducting thin film (platinum/nickel) as the sensing surface. Pure metals, of consistent quality, secure within given temperature range, and able to give reproducible electrical resistance-temperature readings qualify as thin film materials as the voltage signal is measured by the change in resistance of the film, which is a function of temperature. Therefore metals having high TCR or high sensitivity are preferred. Other desirable qualities include long term stability, repeatability of physical properties and structure, resistant to oxidation, no hysteresis, and high mechanical strength and ductility. Transition elements like platinum, copper, nickel and silver etc. thus qualify for use as thin films in TFGs. The thermal properties of some commonly used materials for TFGs are listed in Table C.1 (*Appendix C*).

4.2.1 Fabrication using hand painting

In this particular application, silver thin film gauges are prepared by hand painting with pyrex substrate having 6 mm diameter and 10 mm length. The whole fabrication procedure can be divided into following subheads.

4.2.1.1 Substrate preparation

Substrate surface must be smooth, highly polished and void of cracks for convenient application of sensing material over it. The Pyrex surface is first polished using 300 grain silicon carbide sand paper (wet or dry) [Kinnear and Lu 1999], followed by 600 grain sand papers. Keeping in view that the substrate surface remains flat and level, this procedure is continued for several minutes until the desired smoothness is achieved and the surface became visibly polished. The edge of the cylinder is then chamfered using sandpaper and the substrate is washed properly followed by adequate heating in an oven to make it moisture free. The smoothing process is very important since any geometric discontinuities in the substrate material such as fine cracks or cavities may produce faulty sensors. Also, polishing improves surface quality a lot. Therefore, enough emphasis has been laid on the substrate surface preparation.

4.2.1.2 Film deposition

First, a very thin film of the sensing material (silver/platinum/CNT-silver) is hand-painted on a well-polished pyrex surface. Immediately after application of it, gauges are allowed to dry in a clean environment to avoid the collection of dust or other impurities on the gauge surface. Then the whole pyrex substrates are supported on a steel base and introduced in an oven for a few minutes (10-15 min) at a desired temperature. After baking, the oven is allowed to cool down to room temperature before taking the gauges out. Afterwards, the resistance of the film is measured using a multimeter. If the resistance is not a desirable one, a second layer of thin film is coated over the previous layer and baked again. The procedure is repeated until the desired resistance is achieved (10-100 Ω). Care must be taken about the amount of thinner used, which if more, would result in poor adhesion and if less, would affect the resistance of the gauge. The temperature used for baking silver gauges is 350 ˚C. There are several methods of film deposition which includes spin coating, physical vapour deposition, chemical vapour deposition, sputtering etc.

4.2.1.3 Lead wire connections

Additional silver stripes on each side of the gauges are painted to ease lead wire connections. Care is also taken while applying the silver stripes since too much application of silver may lower the resistance by shortening the effective length of the film. After application of the silver strips, the piece is dried and baked as described above. The final step in gauge construction is making electrical connections to the silver stripes. The wire connections over the thin film sensor are soldered using a micro-soldering iron. Once the connecting wires are welded to the horizontal silver stripes, Teflon is used to secure the connections. It is ensured that both the connecting wires does not touch each other while wrapping teflon over them. The resistance of the gauge is measured at the ends of the conducting wire using a multimeter. The procedure is continued till the desirable resistance is obtained for the final thin film gauge. A schematic of the TFG is shown in Fig. 4.1(a) while typical silver TFG (STFG) fabricated in-house with above procedure is shown in Fig. 4.1(b). The resistance of the STFG in discussion is found to be 16 Ω.

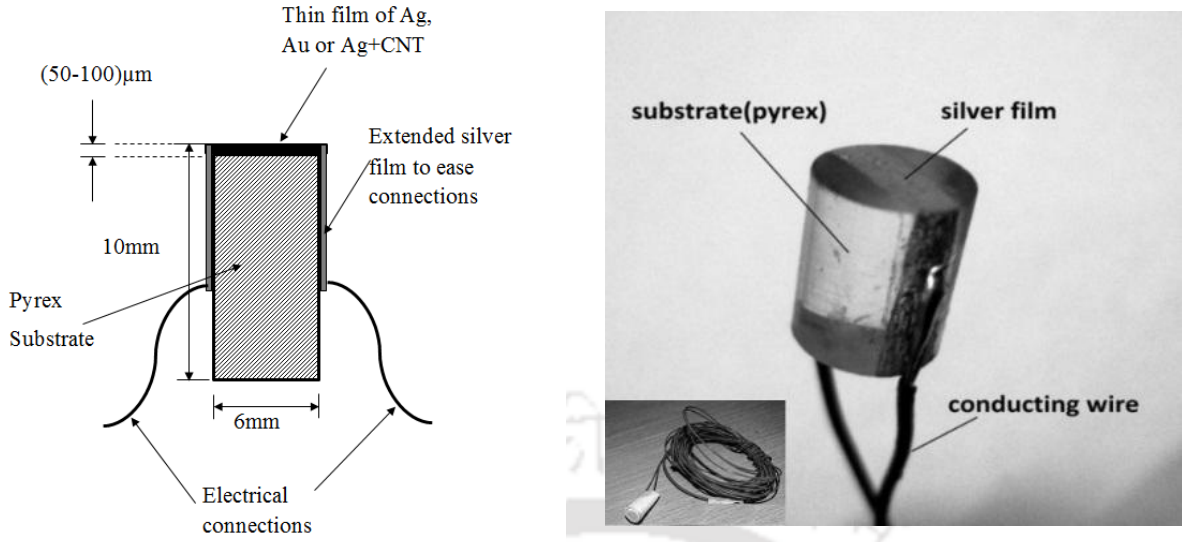

Fig. 4.1(a) Schematic and (b) photograph of a STFG fabricated in the laboratory

4.2.1.4 Surface profiling

The surface of the fabricated gauge is studied under a surface profilometer (Taylor Hobson). The specifications of the profilometer are listed in Table C.2 (*Appendix C*). Despite taking utmost care throughout, the surface of the thin film comes out uneven (Fig. 4.2).

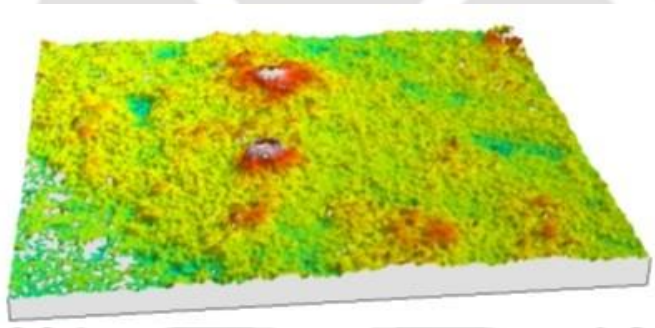

Fig. 4.2 Surface profile of the hand painted STFG

From surface profile, mean surface roughness (R_a) and maximum peak-to-valley height (R_z) are estimated to be 1.775 µm and 19.292 µm.

The evidence of the non-uniform film as supported by Fig. 4.2, is the motivation for exploring other superior methods of uniform film deposition like spin coating, vacuum coating etc. On the first attempt, spin coating method is adopted, the method for substrate selection and preparation being the same for all.

The smoothened substrate is placed over the rotating disk and made to rotate at a high constant speed (1000 rpm). Spin coating method works on the principle of uniform film distribution by centrifugal force. A droplet of the sensing material is poured on the center of the substrate through a hole. The centrifugal force acting on the gauge then leads to a uniform deposition of film material over the substrate material. Rotation is continued while the fluid spins off the edges of the substrate, until the desired thickness of the film is achieved. The applied solvent is usually volatile, and simultaneously evaporates. So, the higher the angular speed of spinning, the thinner the film. The thickness of the film also depends on the viscosity and concentration of the solution and the solvent. However, it is not possible to achieve a desired film in this study. Reasons for failure may be lesser adhesion or very less viscosity of the sensing material, which leads to yet another type of film deposition technique called vacuum coating-one type of physical vapor deposition.

4.2.2 TFG fabrication by physical vapor deposition (PVD)

The overall procedure of fabrication is almost same except for the step of film deposition i.e. mounting the sensing material on the substrate. The vacuum coating procedure is followed for fabricating conventional TFGs with pure silver and later with gold. Similar substrates have been used for both types of gauges i.e. cylindrical pyrex rods of length 10 mm and 6 mm diameter.

4.2.2.1 Vacuum coating

This is a physical vapor deposition (PVD) technique, which uses an electric resistance heater to melt the target material (silver and gold in solid form) and raise its vapor pressure to a useful range. This is done in high vacuum in order to allow the vapor to reach the substrate without reacting with or scattering against other gas-phase atoms in the chamber, and thus, reduces the interaction of impurities from the residual gas in the vacuum chamber. Typically, vacuum deposition takes place in the pressure range of 10^{-5} Torr to 10^{-9} Torr, depending on the level of gaseous contamination that can be tolerated in the deposition system. The base material to be deposited is placed in an energetic, entropic environment, such that particles of material escape from the surface (Fig. 4.3). A cooler surface (the substrate) is placed facing that energetic surface. As the particles arrive, the cooler surface draws energy from them allowing them to form a solid layer.

In the present study, a vacuum coating unit (Model: VT-ACG-03) has been used which consists of high vacuum pumping system, a metallic bell-jar, base plate fitted with low tension (LT) and high tension (HT) electrodes and a digital thickness monitor (DTM; Model: QCT-101). The system specifications and the acoustic impedance of various coating materials are detailed in Table C.3 and Table C.4, respectively (*Appendix C*). Solid targets of pure silver and gold are used for depositing as sensing element on the pyrex substrates. With PVD technique, various films of desired thickness (200 nm to 20 µm) are prepared and lead wire connections are soldered. The resistance of the gauge is measured at the ends of the conducting wires using a multimeter. The TFGs prepared with silver and gold by this method have an initial resistance of 16 Ω and 11 Ω, respectively. The coating procedure is as follows:

a) The chamber is lifted up using the switch provided and the substrate samples are attached to the sample holding plate with glue. The target metal is cut into small pieces and placed on the tungsten boat.
b) Opening the chamber valve the chamber is moved down using the switch provided. Once the chamber sits properly on the O-ring, the chamber valve is closed and the water supply valve is released to cool the chamber and other parts of coating unit.
c) Roughing Valve, Backing Valve, High Vacuum Valve are closed before starting the vacuum pump for evacuating.
d) The roughing valve is opened to release the exhaust from the vacuum pump. No air is allowed to leak into the chamber.
e) Pirani gauge is switched on (GH-1 meter) and reading (mbar) is checked. It takes around 30 min to build a vacuum of 0.05 mbar to 0.02 mbar. When a reading of above 0.05 mbar is attained, the roughing valve is closed and the backing valve is opened and pirani gauge switch is changed to GH-2.
f) It takes around 3 hrs to get vacuum of 0.01 to 0.0001 mbar.
g) When the pirani gauge reading reaches to 0.01 to 0.001 mbar HIVAC valve is opened and diffusion pump is switched on. At this time pirani gauge can be switched of and penning gauge can be switched on as the vacuum which gets created will be beyond the limit of pirani gauge.
h) It takes around 2 hrs to create vacuum of the order $2x10^{-5}$ mbar. When this value is reached, DTM is switched on and the penning gauge is closed. High vacuum valve and backing valve are kept open throughout.

i) Prior to setting the value of 100 on TFG, the DTM is stopped. The value to impedance and density of copper is set from the table (Table C.4, *Appendix C*). Finally after setting the value of film thickness on TL1 $\left(k\,\mathring{A}\right)$, STR (start) is clicked.

j) LT Voltage adjustment variac is slowly operated and the reading in the LT current meter is checked. LT current is changed in steps of 10 A with a gap in between to attain the steady state. Current is increased up to 70 A until the desired film thickness is attained or the DTM shows a constant value. Then voltage is decreased to zero, diffusion pump is stopped and the high vacuum and backing valves are closed. After waiting for 15 min, vacuum pump is turned off and the chamber is allowed to cool with running water for about an hour. Slowly the chamber valve is opened to bring it up to atmospheric pressure.

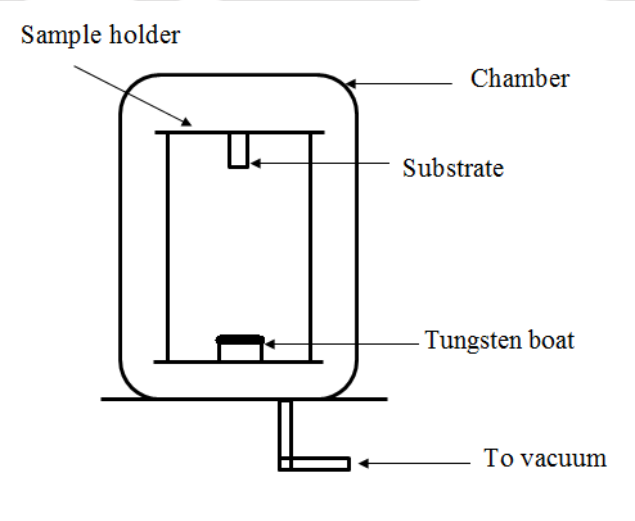

Fig. 4.3 Schematic representation of a vacuum coating chamber

4.2.3 Nanocomposite gauge preparation

The nanocomposite thin film gauge (NCTFG) is fabricated with a carbon nanotube (CNT) layer on silver as a laminated composite topping (Fig. 4.4). It has been reported that mixing nanoparticles of high thermal conductivity into base materials enhances thermal conductivity of the overall mixture [Liu et al. 2005, Gan et al. 2006, Tomar et al. 2011, Carpenter et al. 2011]. In this regard, CNTs have attracted much interest in sensing applications due to their unique electrical properties, high surface to volume ratio, low cost and their ability to enhance thermal properties when mixed with other metals [Liu et al. 2005, Kakac and Pramuanjaroenkij 2009, Wang and Mujumdar 2007]. The CNTs are also oxidative activated

to generate functional groups such as COOH, OH, and CO for better adhesion of sensing metal on substrate surface [Kumar and Sahoo 2012]. Considering these aspects, multi-walled carbon nanotubes (MWCNTs) are considered for this study and substantial thermal property enhancement is expected when CNT's (typically of sizes 1-100 nm) are added to the base metal silver. Composite sensing elements of TFGs are anticipated to help an ample amount for accurate determination of heat transfer from their voltage-time signals.

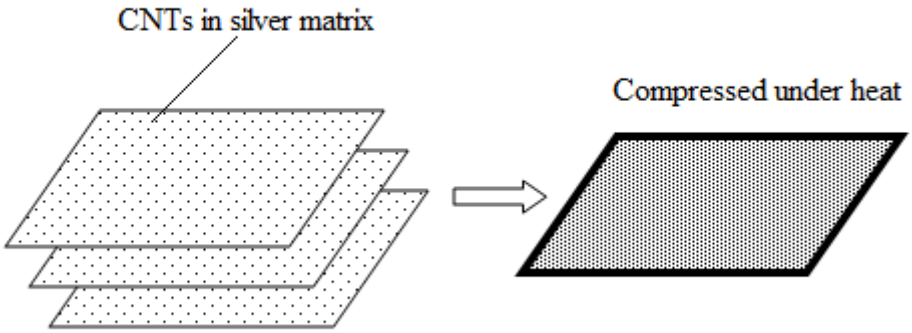

Fig. 4.4 Laminated composite made of silver and CNT

The conductive silver solution is prepared by adding 150 ml of thinning agent (acetone) to 2.65 gm of silver (conductive paste form). Then, desired quantity of CNTs (0.00265 gm; 0.1 wt.%) is added to the silver solution and subsequently the mixture is sonicated in an ultrasonic bath for an hour. The time for sonication is fixed keeping in view that no re-agglomeration arises. When the solution is homogenous and the CNT gets dispersed in the silver matrix well, the acetone is allowed to dry leaving behind a paste of the nanocomposite which can be applied on the substrate. Then, a very thin film of this composite paste is hand-painted on the well-polished pyrex substrate. Additional silver stripes are extended over the surface of the substrate in a horizontal position to ensure adequate material for conduction. The gauge is then kept in an oven, heated in ramp to 350ºC, and subsequently cooled down back to room temperature. This is done to allow self-annealing of the film and to avoid brittleness. After reaching room temperature, the resistance of the film is measured using a multimeter. If the electrical resistance of the film is not adequate, a second layer of coating can be painted on the top of the first one and the procedure is repeated until a desirable resistance value is attained. However, TFGs prepared from single stroke have better uniformity. Finally, wire connections over the thin film sensor are soldered using a micro-

soldering unit and the connections are secured by Teflon. A typical NCTFG prepared in this procedure has a resistance of 5 Ω.

4.4 Characterization of TFGs with XRD

About 95% of all solid materials are crystalline and when X-rays interact with a crystalline substance, a diffraction pattern appears. Every crystalline substance gives a unique pattern which can be observed even in a mixture of substances as the same substance would give the same pattern always. The scattering of X-rays from the atoms produces a diffraction pattern which contains information about the atomic arrangement within the crystal.

To find the Miller indices, atomic plane distances, and for phase analysis X-Ray Diffraction (XRD) tests are performed. For that, thin films are prepared on two separate samples of macor substrate hand painted with silver and CNT blended silver. Since the XRD facility is not equipped with thin film mounting, first XRD test is performed on macor substrate followed by, silver and nanocomposite thin films. Due to the absence of thin film mounting it is expected that thin film data would contain substrate data as well. The peaks of the substrate are later subtracted while calculating peaks for the films. Characterizing is an essential part of TFG usage as it helps to predict the performance of sensor prepared, for e.g. Vinod et al. in 2011 studied MWCNT in XRD analysis. The working principle of XRD and results obtained on samples has been described in the subsequent paragraphs.

4.4.1 XRD working principle and determination of crystal structure

A crystalline material consists of planes of atoms and when x-rays are directed at them, they will be diffracted by the planes of atoms in the crystal. Usually when a beam of x-rays strikes a set of crystal planes at some arbitrary angle, there will be no reflected beam because x-rays reflected from the crystal planes must travel different lengths and will tend to be out of phase or to cancel each other out. But at a particular angle known as the Bragg's angle θ, the reflected rays will be in phase because the distance travelled will be an integral number of wavelengths [Avner 2005]. Such a condition is shown in Fig. 4.5 where a wave is diffracted.

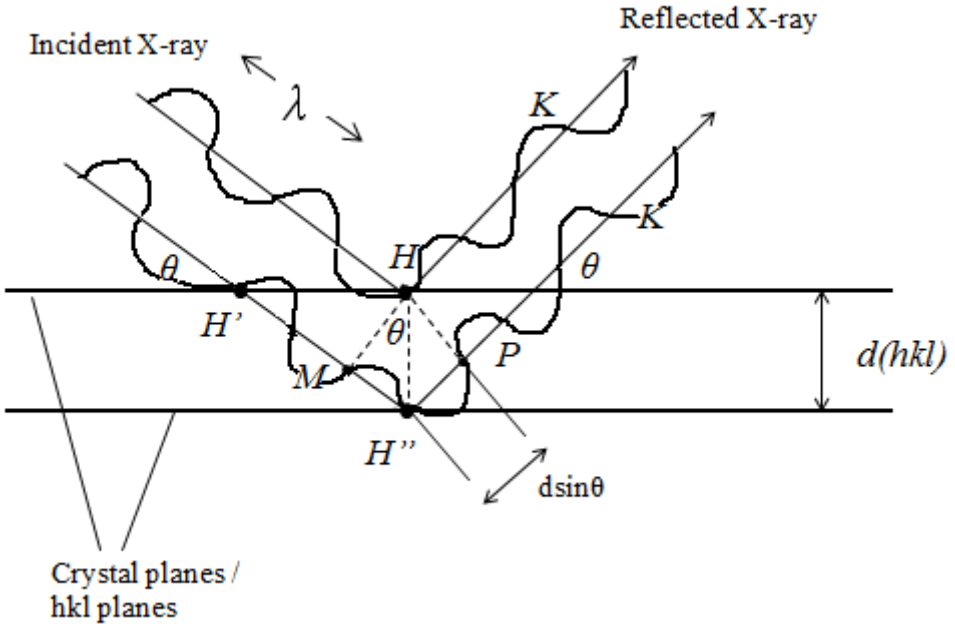

Fig. 4.5 X-ray reflection

The waves may be reflected from an atom at H or H′ and remain in phase at K. However, the reflected rays from atoms in subsurface planes, such as H″ must also be in phase at K. In order for this to occur, the distance MH″P must be equal to one or more integral wavelengths. If $d(hkl)$ is the spacing between planes and θ is the angle of incidence, the distance MH″ is equal to $d\sin\theta$ and the distance MH″P is equal to $2d\sin\theta$.

$$n\lambda = 2d\sin\theta \tag{4.1}$$

where, n is integer and λ is wavelength of incident electron beam and θ is half of Bragg's angle. Spacing between atomic planes d can be calculated by Eq. 4.1. From d-spacing lattice parameter a can be calculated using Eq. 4.2.

$$a = d_{hkl} \times \sqrt{h^2 + k^2 + l^2} \tag{4.2}$$

where, hkl are Miller indices and determined using Sadoway's five step program.

The Sadoway's Five Step Program to Determine Crystal Structure is as follows:

Step 1: Generate a set of $\sin^2\theta$ starting with 2 values

Step 2: Normalize the $\sin^2\theta$ values by generating $\frac{\sin^2\theta}{\sin^2\theta_1}$ where θ_1 corresponds to first peak in the XRD pattern

Step 3: Clear fractions from normalized column

Step 4: Speculate hkl values such that, if expressed as $h^2+k^2+l^2$, would generate the sequence of the clear fraction column

Step 5: Compute for each θ

Table 4.1 Selection rules for reflection in cubic crystals [Brent et al. 2008]

hkl	$h^2+k^2+l^2$	SC	BCC	FCC
100	1	A	NA	NA
110	2	A	A	NA
111	3	A	NA	A
200	4	A	A	A
210	5	A	NA	NA
211	6	A	A	NA
220	8	A	A	A
300	9	A	NA	NA
310	10	A	A	NA
311	11	A	NA	A
222	12	A	A	A
320	13	A	NA	NA
321	14	A	A	NA
400	16	A	A	A

Macor is cut into pieces of size 14 mm × 11 mm × 3 mm size one for base metal silver and another for nanocomposite. Pieces are polished for smooth surface using sand papers. Silver gauge material is applied on the surface (14 mm × 11 mm). Similarly nanocomposite (0.1wt.% CNT blended with silver) is applied on the other substrate piece's surface. The pieces are cured in oven by heating to 350 ˚C and then cooled downed to room temperature. XRD sample and test unit are shown in Fig. B.4 (*Appendix B*).

4.4.2 XRD test on samples

The substrate material MACOR, a machineable glass-ceramic is made up of fluorphlogopite mica in a borosilicate glass matrix. The composition macor is roughly 46% silica (SiO_2), 17% magnesium oxide (MgO), 16% aluminium oxide (Al_2O_3), 10% potassium oxide (K_2O), 7%

boron trioxide (B_2O_3), 4% fluorine (F). Macor can withstand temperatures upto 1000 ˚C and being ceramic it has very less thermal conductivity.

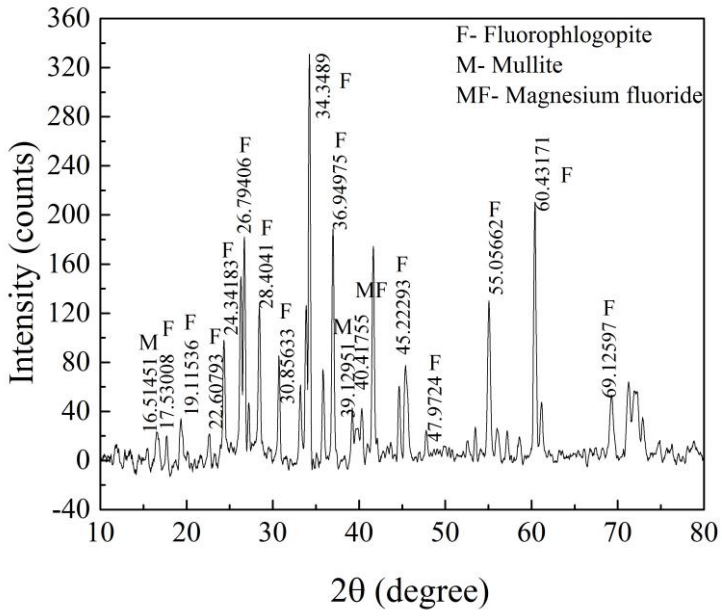

Fig. 4.6 XRD pattern for macor

XRD test unit lacks special mounting equipment for testing thin films for which it was required to test substrate material and find the peaks before actually testing the thin films. The XRD test unit is performed on X'Pert, purchased from PANalatical. The generator voltage of 40 kV and tube current of 30 mA are used for the test and test angle 2θ is set to 10˚ to 85˚ with scan step size of 0.03˚ and time per step 0.5 s. Data obtained is plotted and smoothened to find the peaks.

Fig. 4.6 shows the XRD pattern of macor, whereas Fig. 4.7 and Fig. 4.8 shows the XRD pattern of silver and nanocomposite films, respectively. The peaks at angle 26.79˚ and 34.35˚ in Fig. 4.6 are due to fluorphlogopite [Sazmal et al. 2011], the main constituent of macor. In Fig. 4.7 and Fig. 4.8, the peaks of macor are indicated as M and silver indicated as S. In the silver film, the macor peaks are formed at 26.405˚ and 33.935˚ whereas silver peaks started from 37.775˚ with rest three peaks at 43.985˚, 64.145˚ and 77.105˚. In case of nanocomposite film, the macor peaks occurred at 26.705˚ and 34.235˚ and the silver peaks at 38.045˚, 44.255˚, 64.405˚ and 77.405˚.The peaks for CNTs are expected around 25.9˚. By excluding macor peaks Miller indices, d-spacing and lattice parameter are calculated using Sadoways five step program which are presented in the Table 4.2.

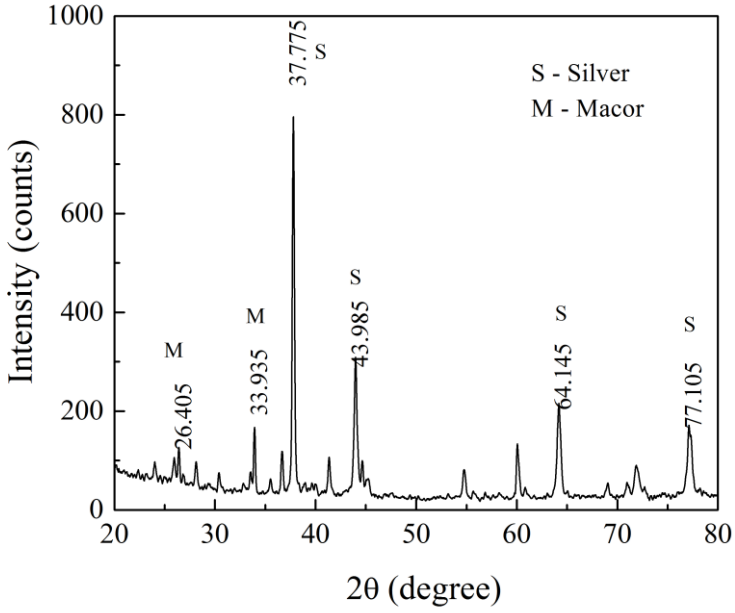

Fig. 4.7 XRD pattern for silver film over macor substrate

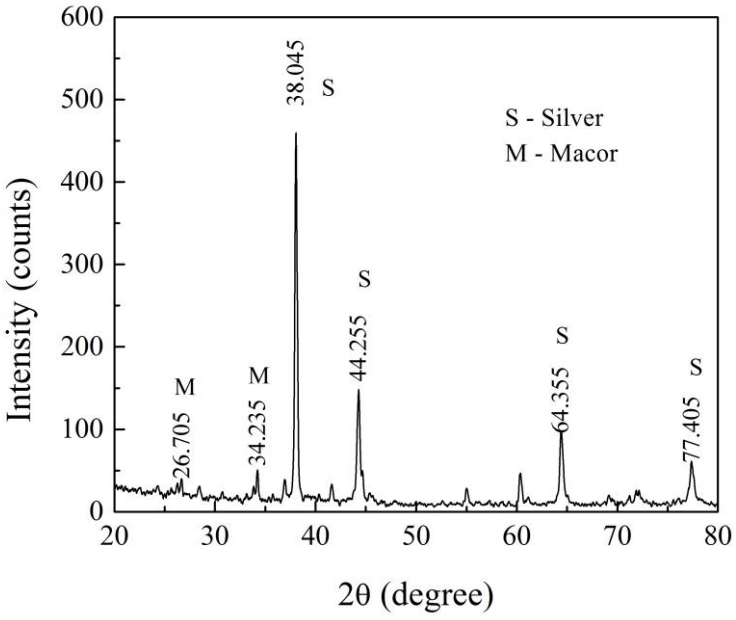

Fig. 4.8 XRD pattern for nanocomposite film over macor substrate

Table 4.2 Miller indices and d-spacing calculations for silver thin film prepared on macor

2θ (degree)	$\sin^2\theta$	$\frac{\sin^2\theta}{\sin^2\theta_1}$	$3\times\frac{\sin^2\theta}{\sin^2\theta_1}$	$h^2+k^2+l^2$	hkl	$d=\frac{n\lambda}{2\sin\theta}\left(\overset{0}{A}\right)$	$a\left(\overset{0}{A}\right)$
37.775	0.104	1	3	3	111	2.379	4.121
43.985	0.140	1.338	4.014	4	200	2.056	4.113
64.143	0.281	2.690	8.072	8	220	1.450	4.103
77.105	0.388	3.706	11.120	11	311	1.235	4.099

Table 4.3 Miller indices and d-spacing calculations for nanocomposite thin film prepared on macor

2θ (degree)	$\sin^2\theta$	$\frac{\sin^2\theta}{\sin^2\theta_1}$	$3\times\frac{\sin^2\theta}{\sin^2\theta_1}$	$h^2+k^2+l^2$	hkl	$d=\frac{n\lambda}{2\sin\theta}\left(\overset{0}{A}\right)$	$a\left(\overset{0}{A}\right)$
38.045	0.106	1	3	3	111	2.363	4.093
44.255	0.141	1.335	4.006	4	200	2.045	4.090
64.355	0.283	2.669	8.008	8	220	1.446	4.091
77.405	0.390	3.680	11.040	11	311	1.231	4.085

From the above calculations as tabulated in Table 4.2 and Table 4.3, a slight change in lattice parameter is noticed from $4.121\left(\overset{0}{A}\right)$ to $4.093\ \left(\overset{0}{A}\right)$ when CNT is added to Ag. This decrease in lattice parameter leads to change in the original properties of silver, making it more sensitive, which will be discussed in latter portion of the thesis. The carbon atoms dissolved in Ag lead to decrease in lattice constant [Zhang et al. 2009]. This phenomenon is consistent with the fact that carbon atoms have smaller radius than silver. The reason for CNT peak not appearing is very less amount added to silver base metal and homogeneous distribution of CNT in silver [Lubna et al. 2013]. It has been reported that detection of very small amount of CNT in composites is possible through FESEM and EDX analysis.

4.5 Resistivity vs. thickness

The dependence of resistivity on thickness of the films is studied using copper films (of different diameters) which are vacuum coated on pyrex substrates. Since, hand painted gauges do not have the scope of controlling thickness and uniformity of the film. A four point technique proposed by Van der Paw is used to find the resistivity of these thin films and determine the dependence of resistivity on thickness.

4.5.1 Van der Paw method of resistivity measurement

The method used to find the resistivity of thin films is four point technique proposed by Van der Paw [Vander Paw 1958]. This method works accurately for any arbitrary shape (Fig. 4.9).

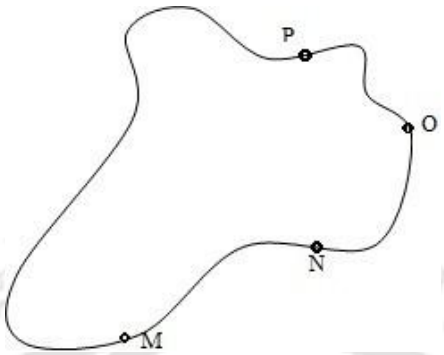

Fig. 4.9 A flat lamella of arbitrary shape, with four contacts M, N, O an P on the periphery

The lamella is considered to be free of holes and is provided with four small contacts, M, N, O and P, at arbitrary places on the periphery as shown in Fig. 4.9. A current i_{MN} is applied along contacts M and N and the potential difference $V_P - V_O$ is measured.

$$R_{MN,OP} = \frac{V_P - V_O}{i_{MN}} \tag{4.3}$$

Similarly current i_{NO} is applied along contacts N and O and the potential difference $V_M - V_P$ is measured

$$R_{NO,PM} = \frac{V_M - V_P}{i_{NO}} \tag{4.4}$$

Van der Paw method is based on the theorem that between $R_{MN,OP}$ and $R_{NO,PM}$, there exists the simple relation:

$$e^{\left(-\frac{\pi d}{\rho_r} R_{MN,OP}\right)} + e^{\left(-\frac{\pi d}{\rho_r} R_{NO,PM}\right)} = 1 \tag{4.5}$$

where, d is the thickness of lamella and ρ_r is the resistivity of the material. If d, $R_{MN,OP}$ and $R_{NO,PM}$ are known then above equation gives ρ_r. When M, O are placed on the line of symmetry while N and P are disposed symmetrically with respect to MO then

$$R_{MN,OP} = R_{NO,PM}$$

$$\therefore \quad 2e^{\left(-\frac{\pi d}{\rho_r} R_{MN,OP}\right)} = 1$$

$$\rho_r = \frac{\pi d}{\ln 2} R_{MN,OP} \tag{4.6}$$

where, ρ_r is the resistivity of lamella and d is the thickness of lamella.

4.5.2 Four probe technique procedure

The procedure followed for the technique can be summarized as follows:

- Ends of four copper wires are made thinner with sand paper and attached at four corners of the sample using silver paste.
- Samples are dried for a day to get until the silver paste bonded to the thin film surface rigidly.
- These four copper wires are soldered to the set up using lead wire.
- During the experiment, current of 1 μA is passed with positive and negative polarities and the voltage difference is noted down.
- Average value of absolute voltage difference is calculated and the experiment is repeated for other samples with different film thickness.
- The equipment used in this technique are listed in Table C.5 (*Appendix C*).

From experimental data it is clear that (Fig. 4.10) electrical resistivity of thin film decreases with increase in thickness. However, when the thickness crosses twice the value of mean free path of electrons of the metal, then the resistivity change with thickness becomes negligible. It can be said that the thickness has entered the bulk limit. In case of copper, the mean free path of electrons at room temperature is 39 nm [Barnat et al. 2002, Rossnagel and Kuan 2004], which is why there is major change in resistivity when the thickness is below 78nm.

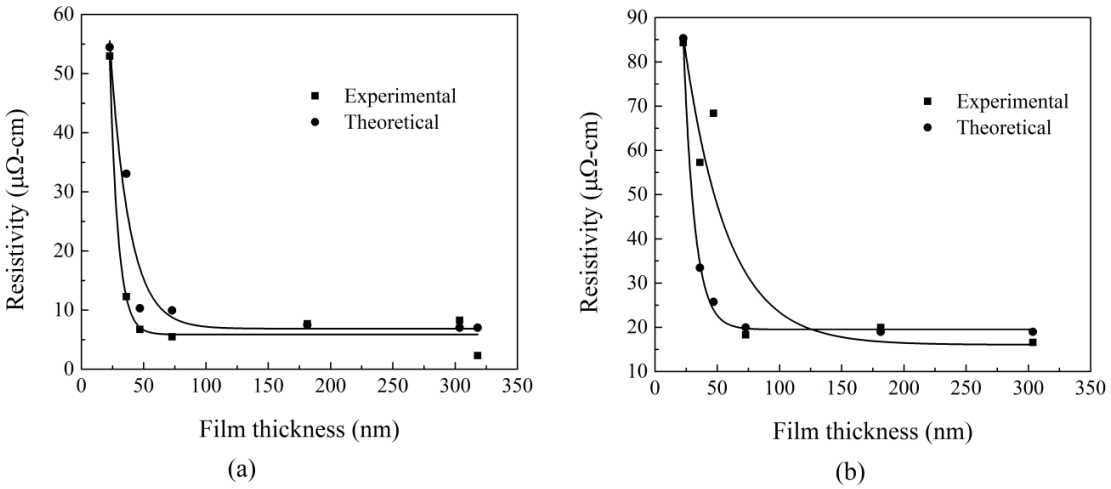

Fig. 4.10 Resistivity vs. thickness of copper film over (a) pyrex substrate and (b) macor substrate

Lacy developed the model to explain why and how the resistivity changes with respect to film thickness. He considered parameters like surface scattering effects and additional scattering effects due to grain boundaries [Lacy 2011-a] and divided the problem into two cases:

Case I: When thickness of the film is more than or equal to twice the bulk mean free path of material i.e. $\left(t' \geq 2l_{bulk}\right)$

In this case, measured reference resistivity is larger than the bulk material resistivity due to fabrication or processing technique as well as impurities in the material. A scaling factor is used to modify the bulk resistivity.

$$\rho' = C\rho_0' \tag{4.7}$$

where, C is a constant $C \geq 1$, ρ_0' is resistivity of bulk material, t' is the thickness of the film and l_{bulk} is bulk mean free path.

Case II: When the thickness of the film is less than two times the mean free path of material i.e. $\left(t' \leq 2l_{bulk}\right)$

In this case as well, fabrication technique and impurities increased the resistivity of film. Also, scattering due to grain boundaries and roughness could have significant role in

resistivity changes. Therefore, effective thickness has to be considered which is $t'' = t' - \eta$ where, η is the reduction factor.

$$\rho' = \frac{C\rho_0'}{k'\left[1-\ln k'\right]} \quad \text{and} \quad k' = \frac{t'-\eta}{2l_{bulk}} \qquad \text{(4.8(a) \& 4.8(b))}$$

Eq. 4.8(a) represents the thin film resistivity with all scattering effects taken into account when the thickness of the film is less than the two times the bulk mean free path of the gauge material. Lacy represented the formula relating resistivity of a film to its thickness:

$$\rho' = C\rho_0' \left[\frac{1}{\frac{\left[2\sqrt[\delta]{\gamma/KT} - b\right](\tau_1/\tau_2 - 1)}{2a+b} + 1} \right] \text{ when } t' \geq 2l_{bulk} \qquad \text{(4.9(a))}$$

$$\rho' = \frac{C\rho_0'}{k'\left[1-\ln k'\right]} \left[\frac{1}{\frac{\left[2\sqrt[\delta]{\gamma/KT} - b\right](\tau_1/\tau_2 - 1)}{2a+b} + 1} \right] \text{ when } t' \leq 2l_{bulk} \qquad \text{(4.9(b))}$$

All the values used in the equation depends on the film material except C and η which changes with the combination of film metal and the substrate. For the present experiments of copper over pyrex the values of C and η are calculated to be 2.96 and 20.5 nm respectively and for copper over macor the values are calculated as 8 and 18.2 nm. Fig. 4.10 shows that for the above mentioned values of C and η, the experimental values matches well with the theoretical values.

4.6 Conclusion

In this study, various thin film gauges made out of silver, gold and composite films are fabricated in the laboratory. The fabrication of conventional STFG is carried out using hand painting technique. Vacuum coating technique is adopted for developing a conventional STFG, gold TFG (GTFG) and finally a NCTFG made by mixing CNTs in silver has also been fabricated. Vacuum coating is confirmed as a better technique over hand painting or spin coating because of the obvious reasons of film thickness control and uniform coating,

except the requirement of a solid/powdered target and the coating chamber. The lowering of initial voltage/resistance noted in the NCTFG compared to pure STFG is attributed to enhanced electrical/thermal conductivity of the gauge due to CNT addition. Finally, the resistivity vs. thickness study on copper films reveal that resistivity decreases with increase in film thickness until a certain limit (bulk limit), after which the values does not change significantly with the change in film thickness.

Chapter 5

Calibration of thin film gauges

5.1 Introduction

Precise estimation of surface heat fluxes in high-speed flow environment is of paramount importance from the design point of view of thermal protection system or cooling system used in high-speed applications. Therefore the next most important step after fabrication of a gauge is its calibration, a measure of how accurate the gauge is able to respond when compared to standard data. Calibration is mainly of two types: static calibration and dynamic calibration. Static calibration or calibration for temperature is the first and most basic calibration requirement for TFGs as they are temperature detectors. Typically carried out in an oil-bath setup, this experiment allows one to measure the variation of resistance with temperature and thus calculate the TCR of the gauges which is the fingerprint of any particular gauge. The experimental setup and method of calibration have been described in this chapter.

The dynamic calibration can be carried out in any mode of heat transfer i.e. conduction, convection or radiation. In thin film based transient temperature/heat flux measurements in short duration time scales, the convective heat loads are the dominant mode of heat transfer. There are potential research areas in which the transient measurements with TFGs can be extended to other modes of heat transfer (i.e., conduction and radiation). At any case, the calibration methodologies with all basic modes of heat transfer are highly essential because they represent the uncertainties in measurement of temperature and subsequent determination of surface heat fluxes in actual applications of these sensors. The radiation based dynamic calibration techniques for such heat flux micro-sensors have been reported using heat lamp [Smith et al. 1999] and pulse laser source [Kumar et al. 2011]. In pure conduction mode of heat transfer experiments, the temperature history and subsequent predictions of surface heat fluxes have been reported for hand-made platinum TFGs [Kumar et al. 2012].

In order to justify the effectiveness of TFGs in applications where the basic mode of heat transfer is ‘convection/radiation’, it is essential to calibrate such sensors in similar

environments. In this backdrop, simple laboratory experiments are designed in which STFG is exposed with heated air flow generated by a "hot-air gun" of known wattage. Experiments are carried out by exposing the STFG to various known step heat load of known input wattage, for the duration of 200 ms. Then, the voltage signals are recorded due to change in temperature of air flow past the TFG. The one-dimensional heat conduction modeling is used to recover the heating loads for the transient temperature data and then compared with the known input heating loads. The numerical simulation using ANSYS-Fluent v. 14.5, is performed in the similar experimental environmental conditions, for same heating loads to obtain the expected convective heat load. The results of experiments and numerical simulation are compared for evaluating the performance of this STFG.

In the second part, the gauge performance is assessed through a radiation based calibration where a laser source of impulse load is used as the input. The experimental results have been compared with GTFG and NCTFG and the advantages of the best gauge are highlighted. Overall, the present investigation focuses on the setting up of different type of calibration methodologies for various TFGs and comments on the qualitative study of influence of CNTs on gauge performance when mixed with silver and used as a composite layer of silver and CNTs.

5.2 Static calibration

5.2.1 Temperature dependent resistance in TFGs

Basically, the TFGs are the temperature detectors for which the resistance increases with temperatures rise in the flow environment. This increase in resistance can be interpreted as rise in voltage, if a constant current is applied across the gauge. So, a voltage-temperature relation can be made through the parameter TCR for a particular TFG. Normally, the sensing element is chosen as pure metal, for which a linear relationship can be obtained between voltage and temperature. Thus, the slope of the voltage-temperature curve can be interpreted as sensitivity of the gauge and the sensitivity divided by the initial voltage gives the TCR of a particular gauge. The thermal properties of sensing material and the resistance of the thin film are the important parameters which affect the TCR of the thin film sensor. Mathematically, the linear relationship for resistance (R) at any arbitrary temperature (T) can be represented as follows:

$$R(T) = R_0\left[1+\alpha\left(T-T_0\right)\right] \tag{5.1}$$

Here, R_0 is the initial resistance of the gauge at temperature T_0 and α is the TCR of the gauge. Since, TFGs need to be activated using a constant current source, the resistance can be converted to voltage form by using Ohm's law and α can be represented by following expression;

$$\alpha = \frac{1}{V_0}\left(\frac{V-V_0}{T-T_0}\right) = \frac{1}{V_0}\left(\frac{\Delta V}{\Delta T}\right) \tag{5.2}$$

The voltage parameters $(V_0 \,\&\, V)$ represent the corresponding voltage values at their respective temperatures $(T_0 \,\&\, T)$. The parameter $\left(\frac{\Delta V}{\Delta T}\right)$ is called the sensitivity of the gauge. Higher the sensitivity of a gauge, lower is its response time. The choice of initial supply current or voltage (V_0) in the power source is such that it should neither be too low to make indistinguishable voltage change nor too high to cause self-heating of the gauge that may either degrade its performance or even damage it completely.

5.2.2 The oil-bath calibration setup

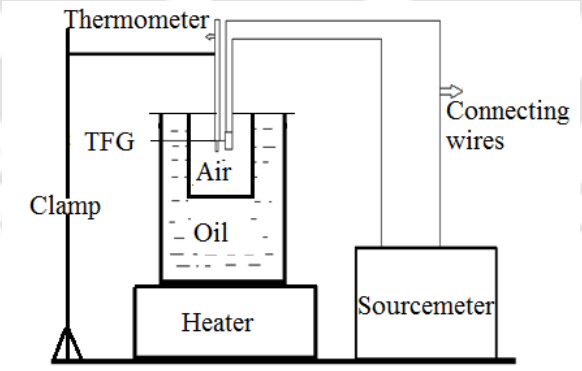

Fig. 5.1 Schematic diagram of oil-bath calibration experiment

The standard "oil-bath calibration procedure" is followed for determination of TCR of the TFGs [Skinner 1962]. For this purpose, an empty beaker containing the gauge is kept inside a silicon oil-bath and heat is supplied to the bath so that the TFG experiences temperature change through the hot air inside the empty beaker (Fig. 5.1). Side by side, a thermometer

(Fluke Hart Scientific 1523 thermometers) mounted in the beaker, is used to monitor the temperature of the hot air. The TFG and the thermometer are kept as close as possible and the top of the empty beaker is covered with aluminum foil in order to avoid any thermal gradient. The TFG is energized by a constant current of 5 mA using a source meter (*Appendix C, Table C.6*). In this environment, the experiments are performed and the readings from TFG are recorded in the same source meter.

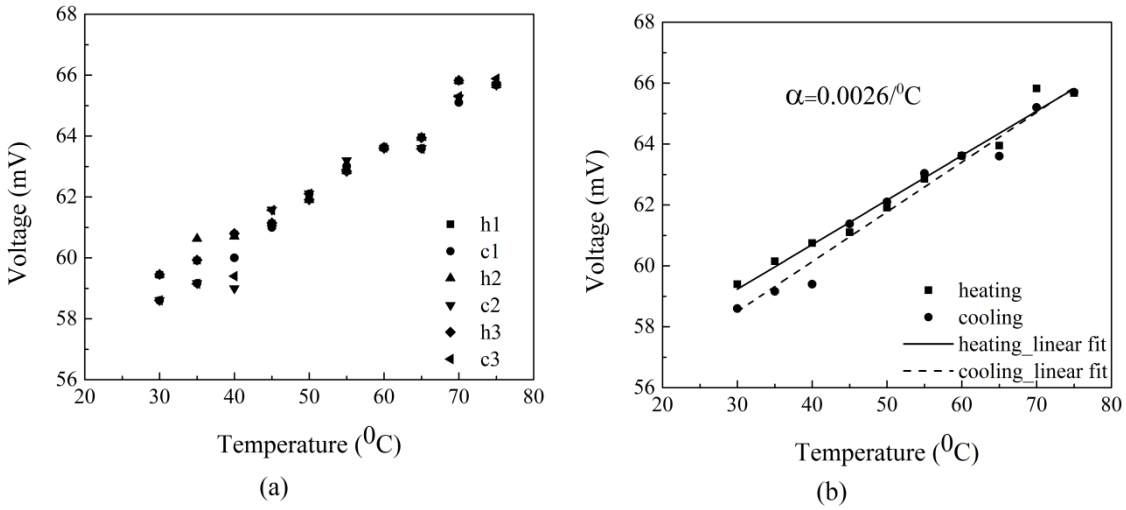

Fig. 5.2 Static calibration experiment of STFG: (a) all voltage-temperature data during heating and cooling process (b) average of all heating-cooling data for determination of TCR

The calibration curve for the STFG is shown in Fig. 5.2, in which the voltage values are plotted against temperature readings at an interval of 5 ºC, during heating (30 ºC to 70 ºC) and subsequent cooling (70 ºC to 30 ºC) process. In order to check the repeatability of data, three sets of readings are taken in the heating and cooling process (Fig. 5.2(a)). Then, the average value of voltage at each temperature is calculated and plotted in Fig. 5.2(b). The values shown in Fig. 5.2 are the average for three sets of data.

Fig. 5.3(a) and Fig. 5.3(b) are the calibration curves for the GTFG and NCTFG, respectively. A trend of the data shows a linear fit between temperature and voltage, which is an indicator for choice of sensing material of TFGs even for CNT blended silver gauge. The slope of the linear curve can be easily computed and is known as the 'sensitivity' of TFG. With known input voltage, (Eq. 5.2) is used to determine the TCR of each of the gauges as listed in Table 5.1. Thus, the determination of TCR for a TFG enables the user for inferring temperature data from the voltage readings. As shown in Fig. 5.3, a lowering of initial

voltage is noted for the NCTFG as compared to pure STFG which could be possibly because addition of 0.1 wt.% CNT on pure silver enhances its ability to augment electrical conductivity and thermal conductivity of the gauge.

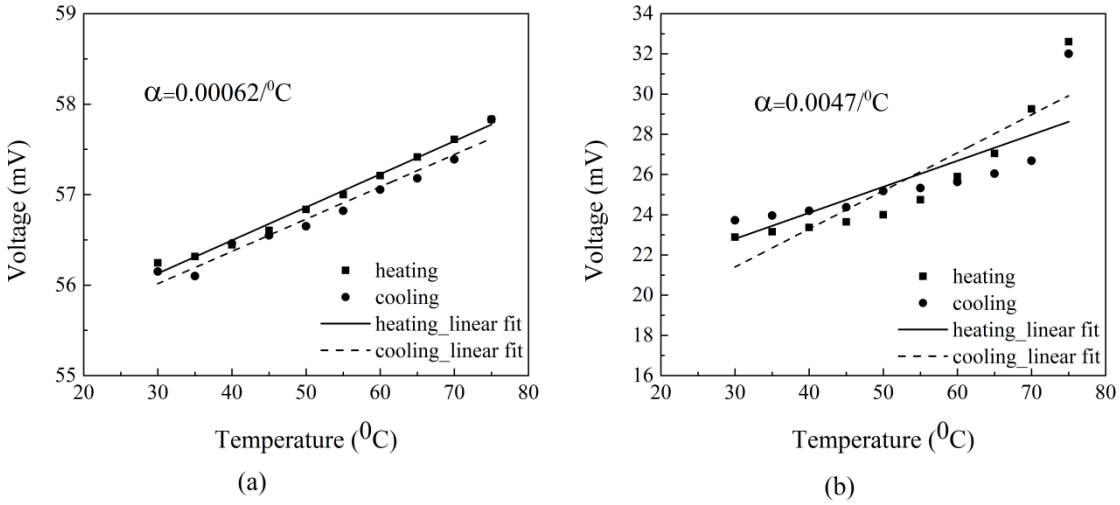

Fig. 5.3 Static calibration curves (a) GTFG (b) NCTFG

5.3 Dynamic calibration: Convection based

In most of the convective based experiments, the heat loads are typically step/impulsive in nature prevailing for a very short duration. Since, the TFGs have fast response time; they can be used for capturing short duration transient temperatures for unknown convective heat loads. In order to resemble the similar nature of heat load, a simple laboratory experiment is designed for calibrating this silver based TFG a for known heat load. Then, the transient temperature response is recorded and subsequently used to calculate surface heat flux with one-dimensional heat conduction modeling. Further, the numerical simulation is carried out to determine the heat flux by imposing boundary conditions with prevailing experimental parameters. This dynamic calibration essentially compares the recovery of the surface heat flux obtained through the hand-made STFG and heat flux predictions with various methods. The details of experimental setup, computation methodology and numerical simulations are discussed in this section.

5.3.1 Experiments with TFG for convective heat load

One of the important objectives of dynamic calibration is to expose the TFG in a heating environment of known heat load and subsequently acquiring its temperature response. For this purpose, the TFG is subjected to a step input heat load from a ‘hot air gun’ of known

wattage (Fig. 5.4). This instrument (Model: TGF 1500 W) has a heater embedded in it that supplies hot air jet to the atmosphere while operating in two modes (low and high). Based on manufacture's specification, it is supposed to generate a power of 1000 W in 'low mode' while the rated power in 'high mode' is 1500 W. The gun has a nozzle of 20 mm diameter and generates hot air at a constant flow rate. The TFG is fixed on a plate at a distance of 10 mm from the exit of the nozzle with its axis, aligned to the axis of the hot air gun (Fig. 5.4). The hot air from the gun is allowed to pass over the TFG surface as a jet for 200 ms duration so that the response from the TFG can be modeled as 'convective step heat load'.

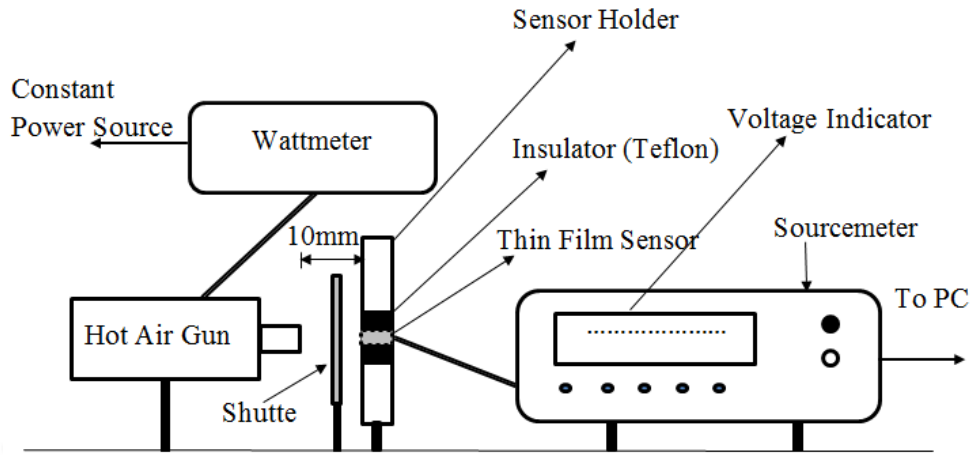

Fig. 5.4 Schematic diagram of hot-air gun calibration experimental setup

Prior to the experiment, the rated power of hot-air gun is measured in the laboratory by using the 'wattmeter' and its efficiency is found to be 90% leading to the powers of 750 W and 1350 W in low and high mode, respectively. Based on these values, the heat fluxes $(\dot{q}_{in})$ are calculated based on area calculated with the nozzle diameter of the hot air gun (Table 5.1). The TFGs are connected to the source meter, which performs the dual service of supplying fixed current (5 mA, to activate the gauges) and recording the output (voltage-time history) at an interval of 0.2 ms. Then, the voltage data is transferred through a terminal emulator (TeraTerm) and connecting the source meter to the computer with serial communicator (RS-232).

With repeated trials of experiments, the typical voltage signals captured from the STFG are shown in Fig. 5.5. It is seen that the gauge responds immediately as the hot air jet passes over it and the 'time constant (τ_c)' for both modes of operation are given in Table 5.1, which is calculated as the time taken by the system to reach 63.2% of the full scale average

[Doebelin 1990]. From Fig. 5.5, its value is calculated as 28 ms and 11 ms in low and high modes, respectively. From the voltage signal and with the knowledge of TCR, it is possible to obtain the rise in transient temperatures during the experimental time scale of 200 ms.

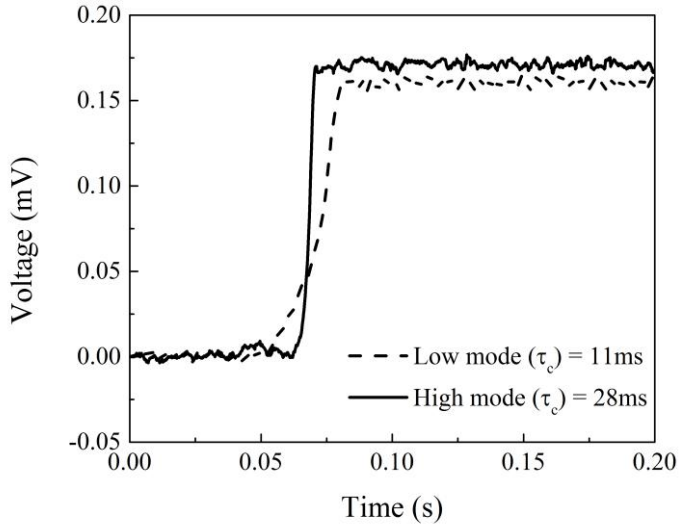

Fig. 5.5 A typical voltage-time history from STFG during hot-air gun calibration experiment

The surface heating rates from transient temperatures in short duration time scale can be recovered by using appropriate one-dimensional heat conduction modeling [Refer section 3.4 of Chapter 3]. The surface heat fluxes estimated from the temperature histories are shown in Fig. 5.6(a). After the initial period of 50 ms, there is sudden rise in surface heat flux and the rate of rise is faster when the gauge experiences higher heat load. The peak surface heat flux (1450 W/cm^2) is noticed immediately after 10 ms in 'high mode' while the peak value (750 W/cm^2) in 'low mode' is observed after 20 ms after application of heat. For convenient interpretation of the 'time constant' values in both modes, the magnified view of the heat flux plots during 0.05 s to 0.1 s, is also plotted in Fig. 5.6(b). In 'low mode' the rise in heat flux is gradual (i.e. 'ramp') and in other case, there is a sudden spike is observed. This shows the capability of TFGs for responding changes in temperatures in both cases. However, the 'step' nature of heat load is more analogous to situations in high enthalpy facilities where the test-flow durations are 1ms or less. In this short time scale, the convective heat load is typically 'step' in nature so that Eq. 3.7 can be used to obtain the time average values of heat flux from the transient temperatures. In this case, the values are calculated for both the mode of operations and given in Table 5.1.

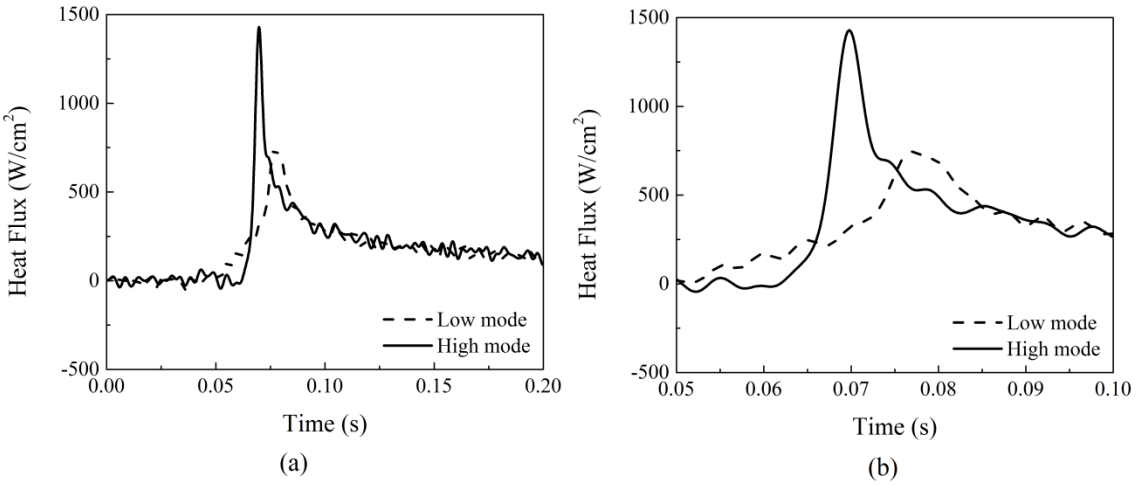

Fig. 5.6(a) Surface heat history from recovered through one-dimensional heat conduction modeling (b) magnified view of the peak heat flux

When compared with the input heat flux values based on the nozzle area, the deviation is seen to be larger (27%) in 'low mode' and smaller (9%) in 'high mode'. It essentially means that the sudden rise in convective heat load in short time is recovered more accurately through this one-dimensional modeling based on semi-infinite substrate assumption. The thermal penetration of heat into the substrate becomes significant when there is gradual rise in heat flux. Thus, the accuracy of predictions of surface heat flux drops through one-dimensional heat conduction modeling with semi-infinite assumption. The other possible cause of discrepancy may be the unaccountable convective losses, even though sufficient care has been taken during the experiments.

5.3.2 Numerical simulation

The aim of this investigation is to provide an insight about flow parameters and estimate heat flux at the senor location with prevailing experimental parameters. For this purpose, an empty half-domain with appropriate dimensions is chosen and experimental flow conditions are simulated for transient incompressible flow in an axisymmetric geometry (Fig. 5.7). Using the commercial package (ANSYS-FLUENT v.14.5), the flow is simulated as an axial jet of heated air entering to the domain. The inlet of the domain is modeled in two parts; 'inlet 1' having a mass flow inlet of 0.0018 kg/s and 'inlet 2' with no mass flow. (i.e. stagnant atmospheric inlet at temperature of 25 ºC). The total mass flow is considered only in the horizontal direction and any vertical velocity is neglected at inlet. The mass flow rate for

'inlet 1' is same for both modes of operation of hot air gun. But the inlet temperature is kept at 300 ºC and 500 ºC for low and high mode, respectively. The width of the 'inlet-1', is chosen based on the nozzle radius $(d = 10\ \text{mm})$ of the hot air gun while the choice of width of 'inlet-2' is arbitrary keeping in view that the upper boundary is far enough to be effected by the nozzle flow (Fig. 5.7).

A half domain is considered since the flow is symmetrical along the horizontal axis and also to reduce computation time. The computational half-domain has a length of 300 mm with height of 160 mm while maintaining symmetry along the axis. Uniform quad meshing has been applied over the domain and the mesh size is adapted as a result of mesh independent study. The time step size has been fixed at 1 ms with the number of steps as 50. The convergence criterion is fixed at 10^{-6} with number of iterations as 50 per step.

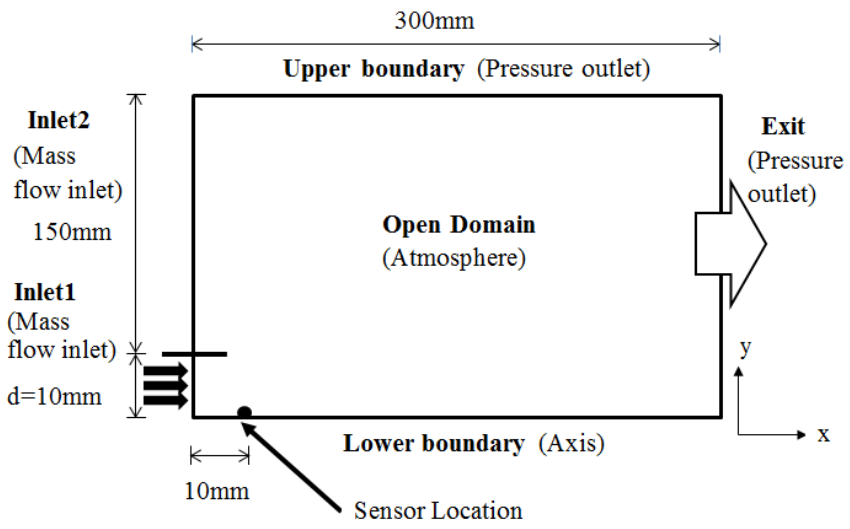

Fig. 5.7 Computational domain for flow field simulation

In order to validate the simulation study in terms of accuracy, the non-dimensional velocity profiles (u/u_c) are plotted (Fig. 5.8(a)) as a function of non-dimensional distance (y/y_d) at different axial locations (x/d). It replicates classical nature of self-similar velocity profiles with (y_d) as the half width of the jet-the distance from the jet axis where velocity is half the axial velocity (u_c). The present computation matches well with the Gaussian type structure as reported in literature [Otiigen and Namer 1988]. Further, the absolute values of velocity vectors along axial distance are plotted in Fig. 5.8(b). The jet velocity of 10 m/s as modeled in 'inlet 1' in 'high mode' seems to be unaffected till 50 mm from the axial distance. As the

axial distance increases, it interacts with the surrounding air and the velocity gradient in vertical direction becomes comparable to the axial velocity (Fig. 5.8(b)).

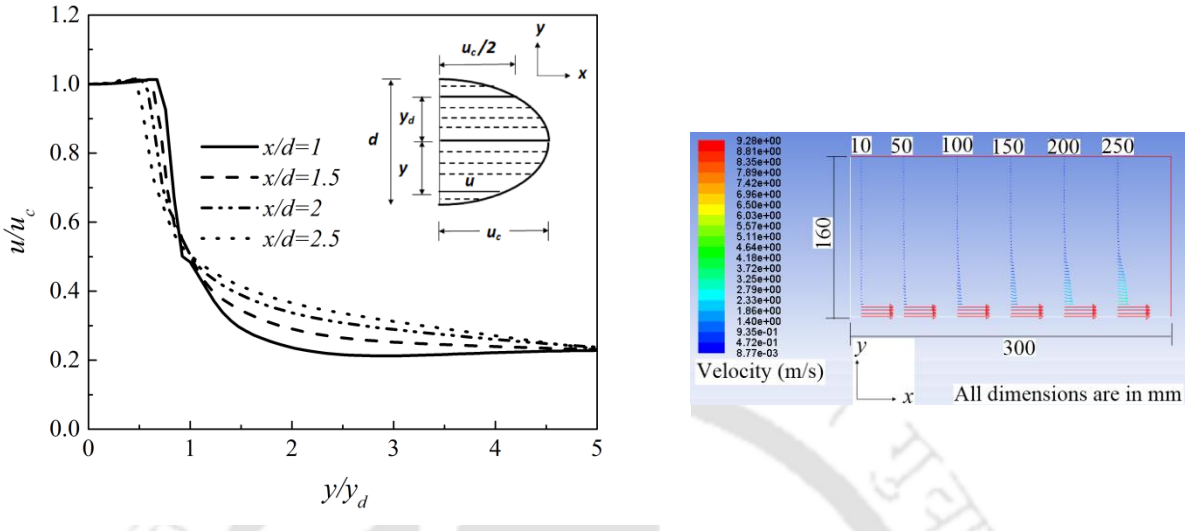

(a) (b)

Fig. 5.8 (a) Self-similar velocity profile (b) velocity vectors in the computational flow field

However, at the location of TFG during experiment (i.e. 10 mm in the axial direction), no significant entrainment of atmospheric air is noticed. It further reconfirms the accuracy of the simulation for the present investigation and resembles the behavior of classical velocity profile for a hot air jet expanding in atmosphere [Cziesla et al. 2001, Otiigen and Namer 1988]. The average heat fluxes $(\dot{q}_n)$ at the senor location (10 mm) are estimated to be 278 W/cm^2 and 411 W/cm^2, for low and high modes, respectively (Table 5.1). The deviation in terms of predictions of surface heat flux is seen to be small (i.e. 5%) for higher convective heat loads in short time scale. The accuracy of prediction drops when time scale of experiment increases for which there is gradual rise in convective heat load. It essentially highlights the fact of effectiveness of TFGs for inferring surface heat fluxes from transient temperatures in short duration experiments.

Table 5.1 Heat flux estimation for low and high mode for hot air gun experiment

Convective heating gun mode	Time constant τ_c (ms)	$\dot{q}_{in}$ $(\mathrm{W/cm^2})$	$\dot{q}_{\exp}$ $(\mathrm{W/cm^2})$	$\dot{q}_n$ $(\mathrm{W/cm^2})$	Deviation (%) $\left(\frac{\dot{q}_{in}-\dot{q}_{\exp}}{\dot{q}_{in}}\right)\times 100$	Deviation (%) $\left(\frac{\dot{q}_{n}-\dot{q}_{\exp}}{\dot{q}_{n}}\right)\times 100$
Low	28	287	210	278	27	24
High	11	430	390	411	9	5

5.4 Dynamic calibration: Radiation based

In order to study the effectiveness of TFGs for estimation of transient surface heat transfer, radiation based experiments are performed by applying impulse heat load from laser light of known input wattage. The experiments are performed by using a continuous type CO_2 laser machine and its schematic representation is shown in Fig. 5.9.

5.4.1Experimental setup

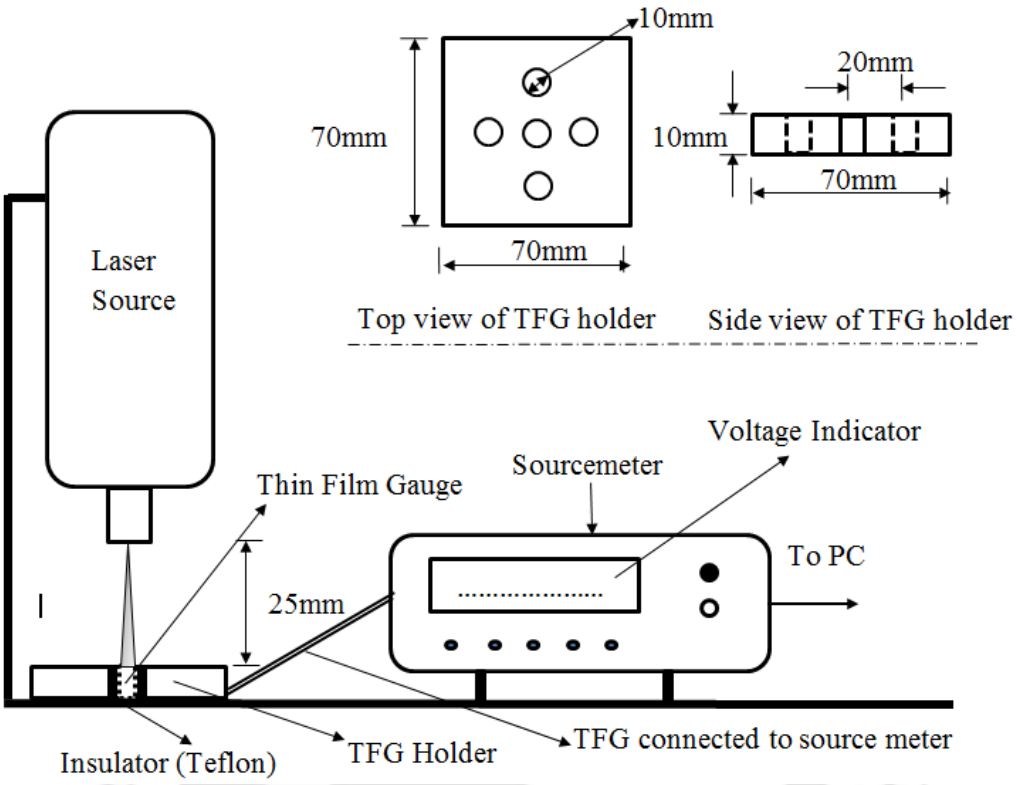

Fig. 5.9 The laser based experimental setup for calibration of heat loads

The experimental setup consists of the TFGs and their holder, source meter, a computer and the laser source. The TFG holder (i.e. an aluminum plate of 70 mm × 70 mm × 10 mm) wherein the gauges are embedded is designed specifically for this experiment. It has circular holes of 10 mm diameter and has a provision for mounting five sensors at a time (Fig. 5.9).

Due to experimental constrains, not all TFGs can be exposed to laser radiation simultaneously. Therefore, the current design of TFG holder allows the user to avoid repeated mountings of TFGs on the aluminum plate for reiterative measurements. The same source meter is an integral part of TFG instrumentation which performs the dual service of supplying fixed current and recording the output. A total of 1000 points are recorded at an interval of 5

ms that implies data capture for a total time of 5 s. The laser beam is irradiated over the specimen surface along the predefined path. During the experiments, few parameters such as, laser power, shutter open time, duty cycle, frequency etc. are fixed as listed in Table C.7 (*Appendix C*). Keeping every other parameters of the instrument fixed, the TFGs are exposed to impulse heat loads for a time scale of 0.1 s for two different power inputs of laser source (10 W and 20 W). Each set of process conditions (experiment) have been performed with five trials to check the repeatability of the gauges. 30 sets of reading are taken with 5 sets for each sensor. The source meter is then interfaced with a computer with serial communicator (RS-232) and the stored data is recovered through a terminal emulator (TeraTerm) installed in the computer.

5.4.2 Estimation of applied surface heat flux

Transient temperature responses from the TFGs are recorded through voltage signals for the known impulse heat load. Further, with similar one-dimensional heat conduction modelling as described before, the surface heat fluxes $(\dot{q}_r)$ are recovered from surface temperature histories. Comparison of recovered heat fluxes with input heat fluxes are carried out for studying the relative advantages of each TFG.

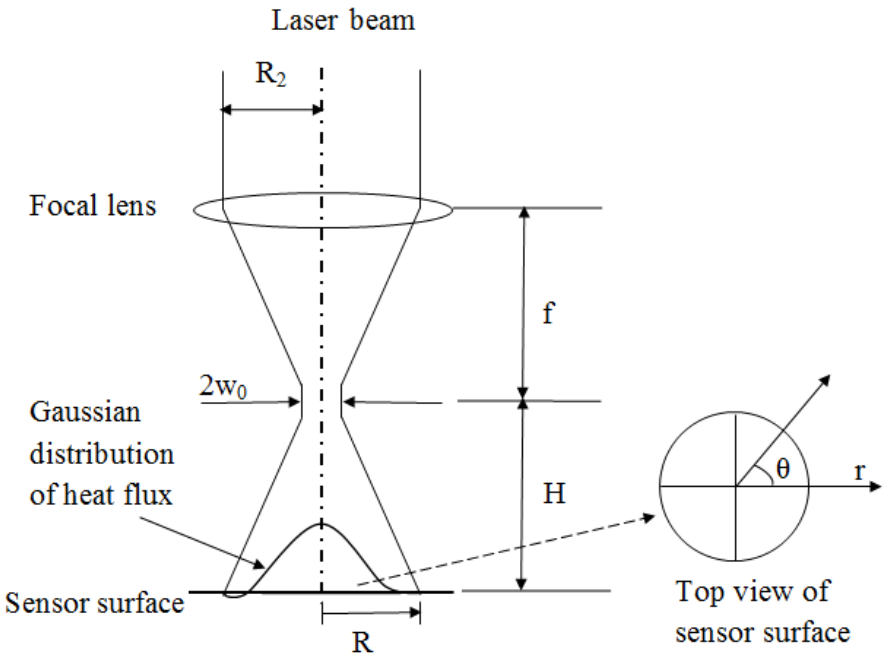

Fig. 5.10 Schematic of the laser beam showing Gaussian distribution of input heat flux

The laser beam in the experiment (Fig. 5.10) follows a "Gaussian distribution" and the beam diameter can be controlled by changing the "standoff distance (H)" between laser head and the specimen surface [Kant and Joshi 2013].

The beam radius (R) is calculated by using standard beam propagation equations as given below (Eq. 5.3);

$$R = w_0\left[1+\left(\frac{M^2\lambda H}{\pi w_0^{\,2}}\right)^2\right]^{\frac{1}{2}};\quad w_0 = \frac{2M^2\lambda f}{\pi D};\ D = 2R \tag{5.3}$$

Here, M^2 is assumed to be 1 while the other parameters, $\lambda = 10.6\ \mu\text{m};\ f = 127\ \text{mm};\ D = 4.84\ \text{mm}$ are considered from literature where the same laser machine has been used [Kant and Joshi 2013]. The locations of TFGs are fixed at the focal point of the laser beam so that the TFGs get exposed to the complete beam area. The Gaussian distribution of heat flux $\left(\dot{q}_{in,r}(r)\right)$ inside the circular laser beam is shown in Fig. 5.10 and the expression for heat flux at any radial location (r) is given by following equation [Ghatak 2009]:

$$\dot{q}_{in,r}(r) = \frac{2\eta P}{\pi R^2}\exp\left(\frac{-2r^2}{R^2}\right) \tag{5.4}$$

Here, P is the laser power and η is the absorption coefficient, which depends on the material on which the laser beam is focused. The values for P and η used in the present study are listed in Table 5.2. It may be noted that the value of η varies with laser wavelength up to a certain limit $(10\ \mu m)$ but becomes almost constant beyond this limit [Steen et al. 2010]. Hence, the laser wavelength of $10.6\ \mu m$ is chosen for the present case. However, while considering CNT based gauges, the effect of absorption of CNTs is neglected as the amount of CNT added is negligible compared to silver. Therefore, the value of η for NCTFG is kept equal to that of STFG.

The total input heat load during radiation experiment has been calculated by integrating the Gaussian heat distribution inside the laser beam (Eq. 5.4) over the complete

cross sectional area. Subsequently, the input heat flux $(\dot{q}_{in})$ is determined by dividing this total heat by the circular cross-sectional area of the incident beam (Eq. 5.5).

$$\dot{q}_{in} = \frac{\int_0^{2\pi}\int_0^{R} q_{in,r}(r)\, r\, dr\, d\bar{\theta}}{\pi R^2} \tag{5.5}$$

The method for recovering heat transfer rates $(\dot{q}_r)$ from transient temperature rise (T_s) during the test time is the same following one-dimensional heat conduction modeling. The recovery of heat flux $(\dot{q}_r)$ from the available voltage history or temperature history is made based on Duhamel's equation similar to the one used for the convection based calibration [Refer section 3.4 of Chapter 3].

5.4.3 Results and discussion

The sample time-voltage signals from all the gauges (STFG, GTFG and NCTFG) corresponding to 20 W input load of laser source is shown in Fig. 5.11.

These signals are obtained after post-processing the raw voltage signals digitally through low-pass filter without distorting the trends of the signals. Temperature histories are deduced from voltage signals after providing the initial applied voltage and the TCR values of respective gauges.

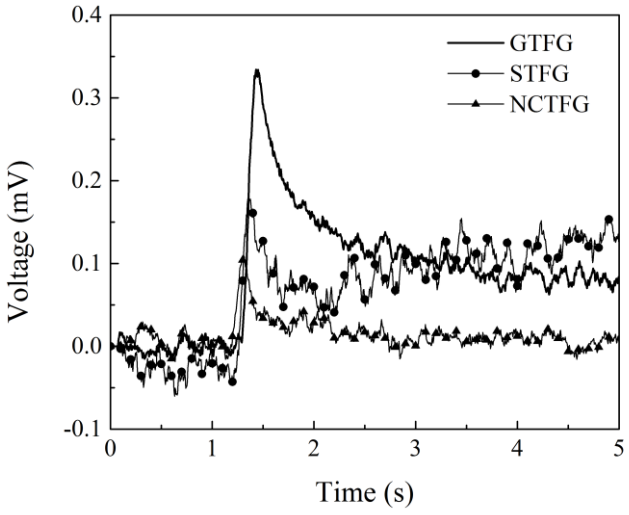

Fig. 5.11 Sample voltage signals obtained from all TFGs juxtaposed together subjected to impulse heat load of 20 W from laser source

It is clear that when all the gauges are subjected to same amount of input heat load for exactly same amount of time, the rise in voltage is less in case of the NCTFG as compared to STFG and GTFG (Fig. 5.11). Since all the gauges are activated by same amount of current (5 mA), a lower rise in voltage indicates a lower value of resistance. Hence, the composite gauge has lower value of electrical resistance. This can be owed to the fact that addition of CNT enhances the electrical conductivity (reciprocal of resistivity) of the gauge. Since an increment in electrical conductivity also implies an increment in thermal conductivity (Wiedemann-Franz Law), the composite gauge is also having a higher value of thermal conductivity [Tritt 2006]. This fact is re-assured by gold film, which has a higher peak than silver (thermal conductivity of silver is higher than gold) and the composite gauge has even lower peak, thus revealing highest thermal conductivity among all three gauges.

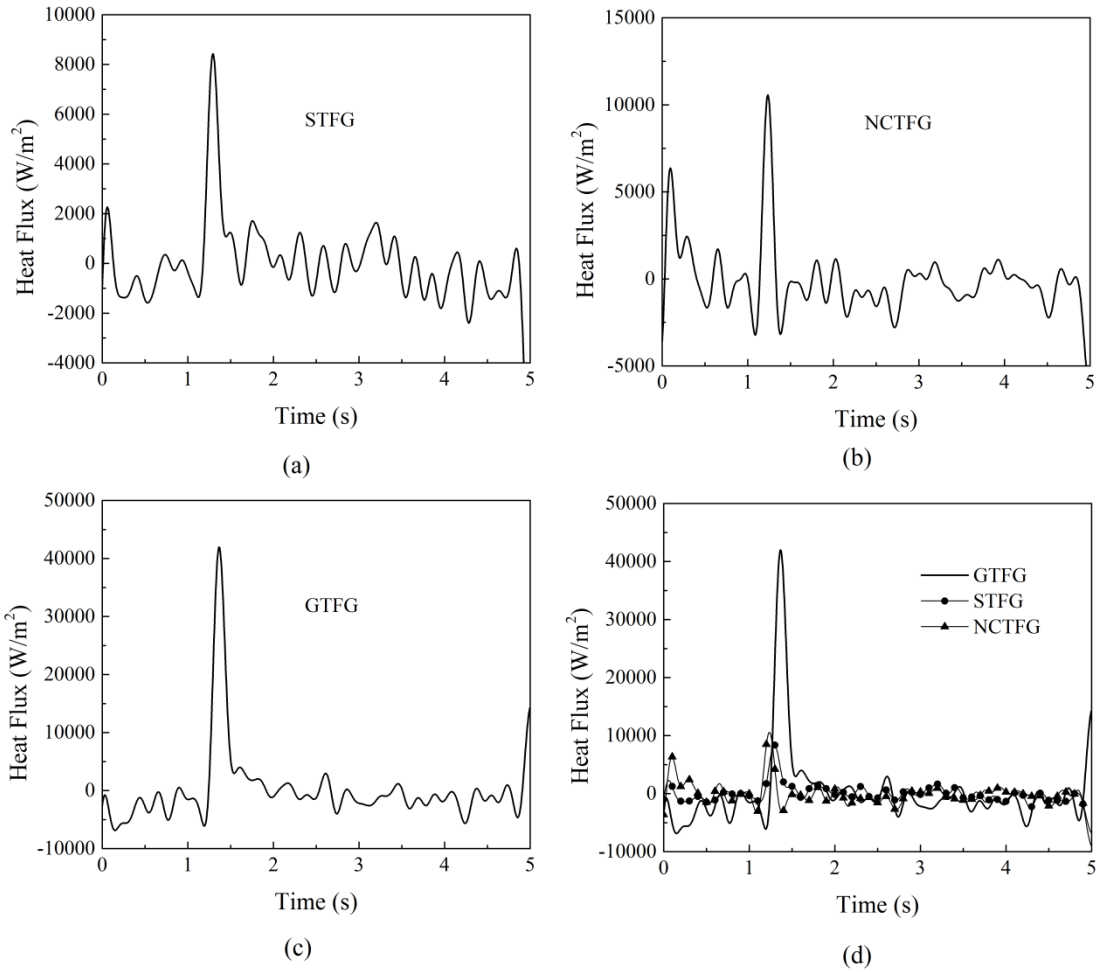

Fig. 5.12 Sample surface heat flux recovered from temperature history of TFGs subjected to impulse input of 20 W from laser source: (a) STFG (b) NCTFG (c) GTFG and (d) all juxtaposed together

The surface heat fluxes $(\dot{q}_r)$ recovered from transient temperatures for all the gauges are shown in Fig. 5.12. Careful inspection of the sample graphs reveal that the impulse heat loads are successfully recovered from the temperature signals of all the TFGs. A comparison between the recovered heat flux $(\dot{q}_r)$ and the input heat flux from laser source $(\dot{q}_{in})$ is shown in Table 5.2. It is indeed worth pointing out here that CNT based NCTFG is more reliable than its silver counterpart in predicting heat flux and quite comparable to GTFG. Hence, it is observed that small amount of CNT addition to base metals like silver can actually give better gauge in both ways i.e. better prediction of surface heat fluxes and cost-effective.

Table 5.2 Comparison of surface heat fluxes obtained from TFGs for laser experiment

Thin Film Gauges	TCR from Experiment (/°C)	Laser power (P) (W)	Input Heat Flux $(\dot{q}_{in})$ (W/m^2)	Recovered Heat Flux $(\dot{q}_r)$ (W/m^2)	Deviation (%) $\left(\frac{\dot{q}_{in}-\dot{q}_r}{\dot{q}_{in}}\right)\times 100$
STFG	0.0026	10	7000	4200	40
		20	13900	8400	39.6
NCTFG	0.0047	10	7000	8800	25.7
		20	13900	10600	23.7
GTFG	0.00062	10	21800	23000	5.5
		20	43800	41800	4.6

This accuracy in heat flux measurement is because of enhancement in thermal conductivity and thereby providing a better estimation of heat load. Higher the conductivity, sooner the heat gets transferred to the substrate surface from the film (lesser temperature difference between film surface and substrate surface) and hence helps in better prediction of heat applied. Further, it is important to mention increase in CNT wt. percentage in composite gauges might enhance the thermal property even more, but the voltage signal would be too low for recording, as the overall resistance would decrease significantly. Hence, a choice has to be made between enhancing thermal properties and maintaining proper signal when composite gauges are fabricated.

5.5 Uncertainty analysis

The difference between the measured value and true value is called “Error”. While experimenting, it is always important to know how close the measured value is to the true value. Since the total error includes random error, which are uncertain, errors are usually

referred to as uncertainties. For any experimental study, uncertainties analysis is a must and needs to be reported along with the measurements.

Kline and McClintock' Method is one of the most commonly used method for uncertainty calculation [Kline and McClintock' 1953]. The method is described below:

Consider a variable N (dependent) which is calculated from various measurements such as u_1, u_2, u_3, u_4…….u_n and governed by the function:

$$N = f\left(u_1, u_2, u_3, u_4, ...u_n\right) \tag{5.6}$$

The total uncertainty in N (Δn) would include uncertainties of u_i ; i.e. Δu_1, Δu_2, Δu_3, Δu_4, Δu_n

Therefore

$$N + \Delta N = f\left(u_1 + \Delta u_1, u_2 + \Delta u_2, u_3 + \Delta u_3, ...u_n + \Delta u_n\right) \tag{5.7}$$

Expanding $f\left(u_1, u_2, u_3, u_4, ...u_n\right)$ by Taylor's series:

$$f\left(u_1 + \Delta u_1, u_2 + \Delta u_2, ...u_n + \Delta u_n\right) = f\left(u_1, u_2, ...u_n\right) + \frac{\partial f}{\partial u_1}\Delta u_1 + \frac{\partial f}{\partial u_2}\Delta u_2 + ... + \frac{\partial f}{\partial u_n}\Delta u_n + O\left(\Delta u_1\right)^2 + O\left(\Delta u_1\right)^3 \tag{5.8}$$

Ignoring second and higher derivatives, overall error is given by:

$$\Delta N = \frac{\partial f}{\partial u_1}\Delta u_1 + \frac{\partial f}{\partial u_2}\Delta u_2 + ... + \frac{\partial f}{\partial u_n}\Delta u_n \tag{5.9}$$

Sometime systematic errors may have equal magnitude in opposite sign which may tend to cancel out each other. So, a reasonable estimate would be to calculate the Root Sum Square (RSS) error given by:

$$\Delta N = \sqrt{\left[\frac{\partial f}{\partial u_1}\Delta u_1\right]^2 + \left[\frac{\partial f}{\partial u_2}\Delta u_2\right]^2 + ... + \left[\frac{\partial f}{\partial u_n}\Delta u_n\right]^2} \tag{5.10}$$

The instruments used in the present investigations include thermometer, source meter, wattmeter, laser source, hot air gun, and oil-bath calibration unit. Based on the manufacturer's specification the accuracy for thermometer, source meter, wattmeter, laser wattage and hot air gun unit are ± 0.01˚C, ± 0.012%, ± 5%, ± 0.01% and ± 0.12% respectively. The uncertainty analysis has been performed by Kline and McClintock's

process (Eq. 5.10) for TCR, transient temperatures and heat flux calculations. Estimates of uncertainties have been listed in Table 5.3.

Table 5.3 Input parameters and uncertainty estimates

Experiments	Parameters	Uncertainty (%)
Static calibration	TCR	±1
Laser	Temperature history	±2
	Heat flux	±2
Hot air gun	Temperature history	±1.012
	Heat flux	±1.012

5.6 Conclusion

All gauges are calibrated for temperature using an oil bath calibration technique and TCR of the gauges calculated. Tests show the linear response of voltage with temperature in the range of 30 ºC to 75 ºC for all the gauges. The TCR values of these RTD type sensors are 0.0026/ ºC, 0.00062/ ºC and 0.0047/ ºC respectively for STFG, GTFG and NCTFG, respectively. The uncertainty in TCR calculation is around 1%.

In the convection experimental investigation, performance of a STFG fabricated in-house, is analysed by exposing it in a convective heating environment. The heat load resembles the nature of a ‘step’ in which the hot air flow prevails over the TFG for 200 ms. The convective experiments are performed with a hot-air gun of known wattage and voltage histories are obtained from the TFG. With the knowledge of TCR, the temperature history is obtained. The transient surface heat flux is recovered from the temperature history by using one-dimensional heat conduction modeling. Further, the numerical investigation is carried out under prevailing experimental conditions in an empty domain. The self-similarity profile of velocity verifies the accuracy of the simulation and the heat flux is computed. The results from all these investigations are compared critically and show a good agreement with reasonable deviation of 5% in ‘high mode’ and 25% in ‘low mode’ of hot-air gun operation.

In the latter part, impulse heat loads of known wattages are supplied to the gauges (silver, gold and nanocomposite) with the help of a laser source and their transient temperature responses are captured. The experimental observations reveal the fact that thermal and electrical conductivity of the nanocomposite gauge is higher than normal silver

TFG. In addition, composite gauge is more accurate in estimating heat flux compared to its silver counterpart. Addition of smaller proportions of CNT to silver can help in achieving better accuracy in terms of heat flux prediction. Further, improvements in thermal properties of the sensor are possible by using different methods of film deposition, having control on the alignment of CNTs and study the perfect proportion of CNT in silver matrix to get best results. This study reconfirms the ability of thin film gauges for their usages in practical purposes to recover convective/radiation heat fluxes for very short duration of transient experiments.

Chapter 6

Modeling thermo-electrical properties of TFG with soft computing

6.1 Introduction

As stated earlier, measuring heating rates on surface or interiors continue to thrill researchers, as no perfect gauge is still available to predict applied heat fluxes instantaneously with full accuracy. The usual method of determining heat flux from temperature history through one-dimensional heat conduction equation is based on assumptions like uni-directional heat flow, semi-infinite substrate etc. Various heat recovery techniques include polynomial fitting, cubic spline fitting, linear fitting etc. are in use. As an alternative to that, here we deal with application of intelligent system techniques namely artificial neural network (ANN) and adaptive neuro fuzzy inference system (ANFIS) to recover surface heat fluxes from a given temperature history. This technique is also favorable from the fact that it is timesaving and can handle any kind of data however "messy" trend it may have. Further, these heat fluxes are used to predict the non-linear relationship between thermal and electrical properties of the TFGs that are exceedingly pertinent to the design of efficient TFGs. Later it will be shown how a properly optimized soft computing model can predict the impulsive heat profiles with significant accuracy.

Over the past few decades, soft computing techniques have gained immense popularity in engineering. Their applications vary from control theory and pattern recognition to power and expert predictions systems [Jang and Gulley 1996, MacIntyre 2013]. Some recorded in literature over the last few span of years include application of ANN as diagnostic tool for machines [Zhong et al. 1998, Emmanouilidis 1998], analyzing vibrations [Unal and Wasserman 1990], condition monitoring [Wasserman et al. 1991, Addison et al. 2002], analyzing jerk fields in manufacturing etc. [Unal 1994]. Use of ANFIS is also repeatedly reported in modelling and forecasting data [Li et al. 2006, Mellit et al. 2009, Alasha'ary et al. 2009]. On top of that, ANFIS finds its extensive usage in manufacturing process modeling including turning, end milling, cutting, feeding etc. Usage of hybrid algorithm as training method and Gaussian functions as input membership functions are

found more common in modeling ANFIS predictors. Moreover, different fuzzy systems like ANFIS-GRID and ANFIS-SUB can be combined with ANFIS to get even better results [Wei et al. 2007].

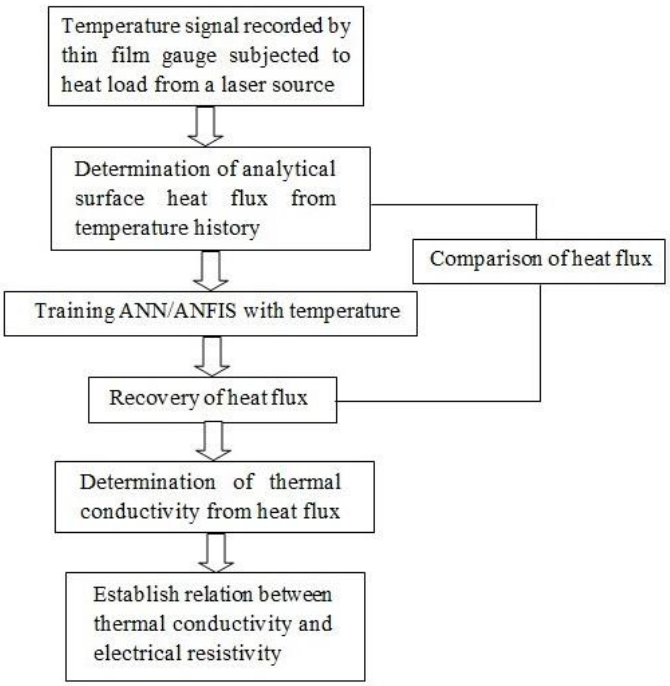

Fig. 6.1 Flow chart representing sequence of the strategy followed

In an attempt to build a smart system, which can predict heat fluxes from temperature history and at the same time intelligently support analysis of thermal and electrical properties of thin film gauges, the performance assessment of the TFGs are done using the laser based study described in the previous chapter. These data or lab observations are used as a training set into the soft computing model to train the network, which will eventually predict the nonlinear functionality inherent in the gauge with the help of this trained data. The objective of this paper is to examine the feasibility and applicability of soft computing in forecasting heat fluxes from temperature data, thereby bringing to light the non-linear relation between thermal and electrical properties of TFGs. The flow chart in Fig. 6.1 shows the strategy followed during the present study. This work thus shows the appropriateness of soft computing technique as a practically constructive replacement of tedious analytical formulation and henceforth effectively quantifies the modeling of TFGs. Soft computing encompasses number of different techniques, only two of which namely ANN and ANFIS are adopted for the present study. Later, it is established that ANFIS performs better than ANN and can be a superior tool for thermo-electrical property prediction in pre-design stage of TFG.

6.2 Experimental investigation:

The gauges are subjected to realistic environment of radiation based experiments applying impulse heat load from the laser light of known input wattage. The experimental setup is exactly the same as described in section 5.3.1 of chapter 5. Fig. 6.2 shows a portion of the laser experimental setup where, the TFG is fixed under the laser. The only difference is that this time four different inputs of power (10 W, 20 W, 30 W and 40 W) for a time scale of 0.1 s are applied as an impulse heat load by irradiating laser on the TFG surface (Fig. 6.2). The extraction of heat flux from voltage plots is also similar.

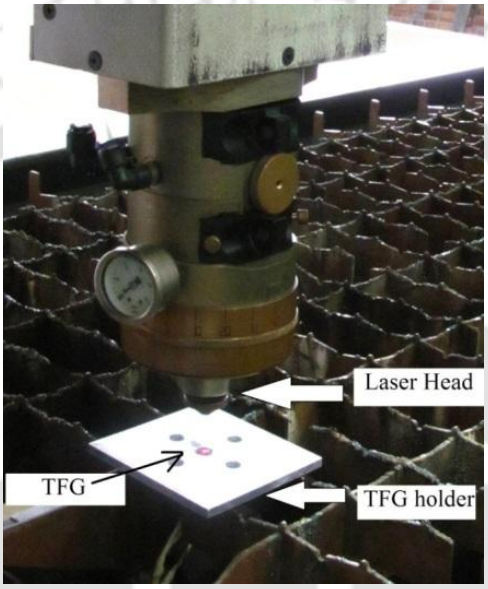

Fig. 6.2 Laser setup used

The extracted heat flux is compared to the input heat flux (experimental) and the values are found to match closely [Table 5.2, section 5.4.3]. Referring to Fourier's law of heat conduction, an effective way for estimating the thermal conductivity per unit length of the gauge ($\frac{k}{\Delta l}$) is to divide the heat flux (q''_{an}) by the corresponding temperature difference (ΔT) [Thirumaleshwar 2009]:

$$q''_{an} = k\frac{\Delta T}{\Delta l}; \Rightarrow \frac{q''_{an}}{\Delta T} = \frac{k}{\Delta l} \tag{6.1}$$

Moreover, with a known value of TCR, change in resistance can be obtained corresponding to change in temperature as [Sinclair 1987]:

$$\Delta R = R_0 \times \alpha \times \Delta T \tag{6.2}$$

where, ΔR is the change in resistance corresponding to a change in temperature of ΔT, R_0 is the initial gauge resistance and α is called the TCR which is calculated experimentally. Combining Eq. 6.1 and Eq. 6.2 we can write:

$$\frac{k}{\Delta l} = \frac{q''_{an}}{\Delta T} = \frac{q''_{an}}{\Delta R} \times R_0 \times \alpha \tag{6.3}$$

This relationship among the change in resistances, thermal conductivity and heat fluxes is non-linear (Eq. 6.3). Thus, soft computing techniques can be an effective tool for prediction of these behaviors from the experimental data. It has already been established through the previous work that the analytically extracted heat flux match well with the experimental input heat flux and hence the verification of soft computing results with the analytically extracted heat flux values would automatically prove its verification with experimentally input heat flux.

6.3 Implementation of soft computing

For developing the soft computing model, experimental data corresponding to an input heat load of 10 W and 40 W from laser source is fed to train the system and the data for an input heat load of 20 W and 30 W are used to validate the system. A data set is prepared by employing experimental temperature history found as a result from a laser beam irradiated on these gauges and extracting heat flux analytically from the corresponding temperature history, considering transient state one dimensional heat transfer within a semi-infinite gauge. The number of input parameters of the training/ testing dataset are two viz. time (t) and temperature (T) and the number of output is one i.e. heat flux (q''_{ann}). Since, soft computing methods, whether ANN or ANFIS can predict better in noiseless signals, therefore the data is filtered before feeding the training/ testing data. Various possible parametric variations are considered to find an optimum network while implementing these techniques for the recovery of the heat fluxes. The parameter optimizations of both the networks are described in detail below. This study is done through the neural network toolbox available in Matlab v. 13-b.

6.3.1 ANN as the prediction tool

ANN is a biologically inspired model for data approximation and is usually presented as systems of interconnected neurons that send messages to each other [Kishor and Das 2010].

Every neuron has an adaptable weight attached to it, which changes based on the learning capability of the network. The complexity of the network increases with the increase in the number of hidden layers as well as number of neurons per layer. The output of the network depends on various parameters like number of hidden layers, number of neurons per layer, transfer function between layers, learning algorithm, network type, number of inputs, number of outputs etc. and variation of any of these parameters would affect the output of the system significantly.

Several network types are available in the neural network toolbox of Matlab. The most common are Feed Forward Back Propagation (FFBP) and Cascade Forward Back Propagation (CFBP). FFBP derives its name from the fact that here the flow of information is only in one direction i.e. forward and the error in every layer is propagated back before sending the information forward further. It is the most common type of neural network used. CFBP are similar to feed-forward networks, but include a connection from the input and every previous layer to following layers. In order to fix the network type various schemes are attempted. However, only FFBP and CFBP are shown. After working out several combinations it is seen that FFBP can predict better compared to other schemes. This might be because in FFBP, in the forward pass, the difference between the output and target is back propagated to the input and the weight assigned to input changes accordingly unless the error is minimized to a certain level. Fig. 6.3(a) shows a comparison between heat flux corresponding to actual input load of 20 W, and the fluxes predicted using different network types of ANN.

Similarly, training function is chosen to be TRAINLM as it gives best output. TRAINLM is a network training function that updates weight as per Levenberg-Marquardt optimization [Jang and Gulley 1996]. Once the learning scheme and training function gets fixed, transfer functions are varied. Fig. 6.3(b) shows the comparison between data predicted with different transfer functions in the hidden layers to process input. Fig. 6.3(c) shows a comparison of heat flux predicted using single and double hidden layer network.

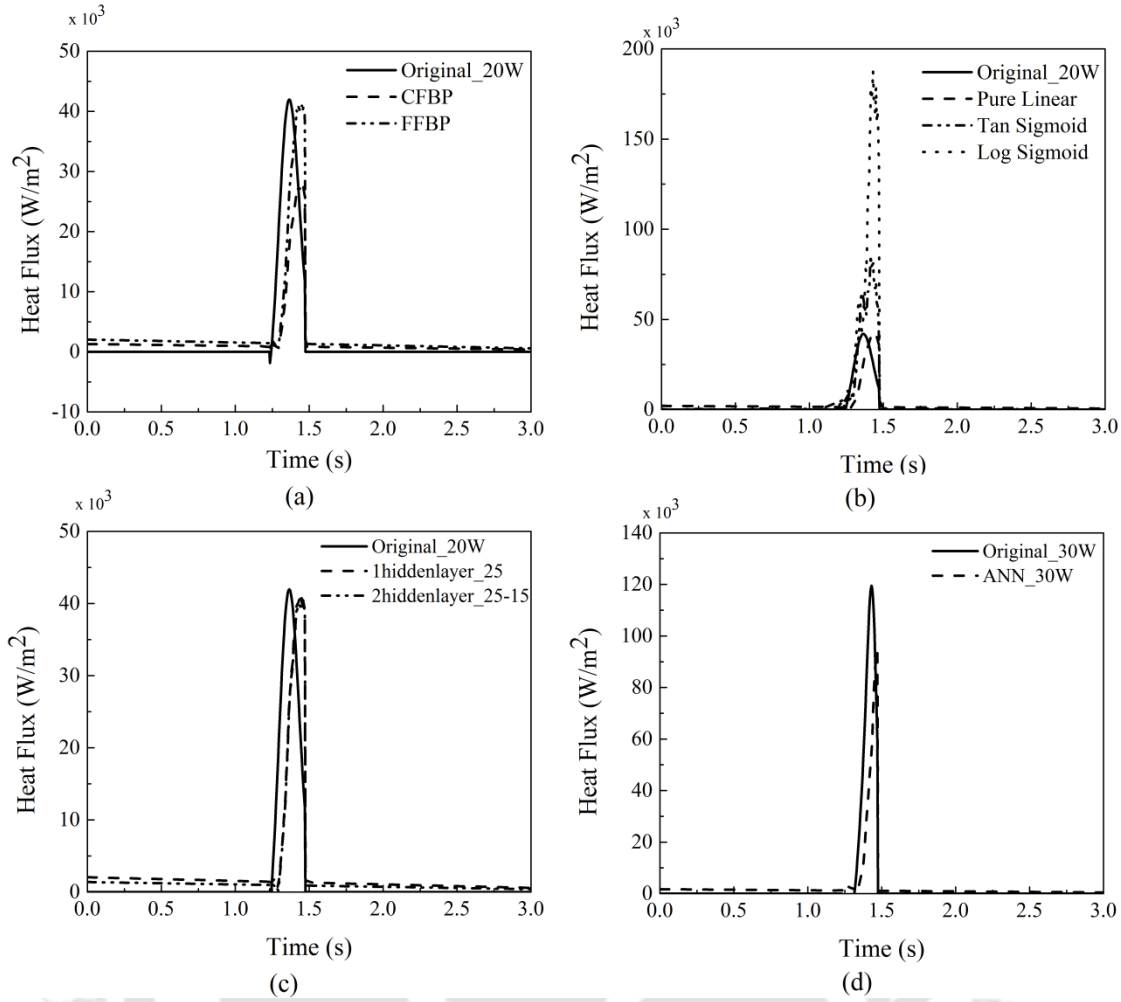

Fig. 6.3 Influence of variation of (a) network type (b) transfer function and (c) number of hidden layers on prediction result of ANN and (d) validation of model with testing data for 30 W heat load for GTFG

After going through number of trials by changing all possible parameters, it is realized that a single hidden layer system with 2 neurons in input layer, 1 neuron in output layer, 25 number of neurons in the hidden layer with pure linear transfer function (PURELIN) and working in FFBP scheme is the best suitable model. Performance function used is MSE (Mean Square Error) which is usually represented mathematically as:

$$MSE = \frac{1}{n}\sum_{i=1}^{n}\left(\hat{Y}_i - Y_i\right)^2 \tag{6.4}$$

Once the optimum model is determined, the same model is implemented to predict the heat flux corresponding to 30 W input heat load from laser. However, it is noticed that ANN is not reasonably successful in predicting the 30 W dataset, which is evident from Fig. 6.3(d). The amount of error involved in predicting peak heat flux is almost 21%. Since, ANN could not

speculate the heat flux corresponding to 30 W dataset correctly; therefore, attempt is made to model a network using ANFIS, which is even a higher adaptive version of ANN.

6.3.2 ANFIS as the prediction tool

ANFIS is a hybrid MISO (Multiple Input Single Output) system, which is created by fusing ANN with FIS (Fuzzy Inference System). Hence, it has the potential to capture the benefits of both in a single framework (adaptive capability from ANN and approximation capability from FIS). ANFIS is a five-layered structure consisting of adaptive nodes i.e. the output of these nodes constantly changes depending on the learning rule to minimize a prescribed error measure [Esen and Inalli 2010]. It tunes a fuzzy inference system based on collection of input/output data. The data used for training/ testing is normalized in order to make it suitable for processing. This is done with the help of membership functions (MF) which can map any function to a value between 0 and 1 depending on its shape.

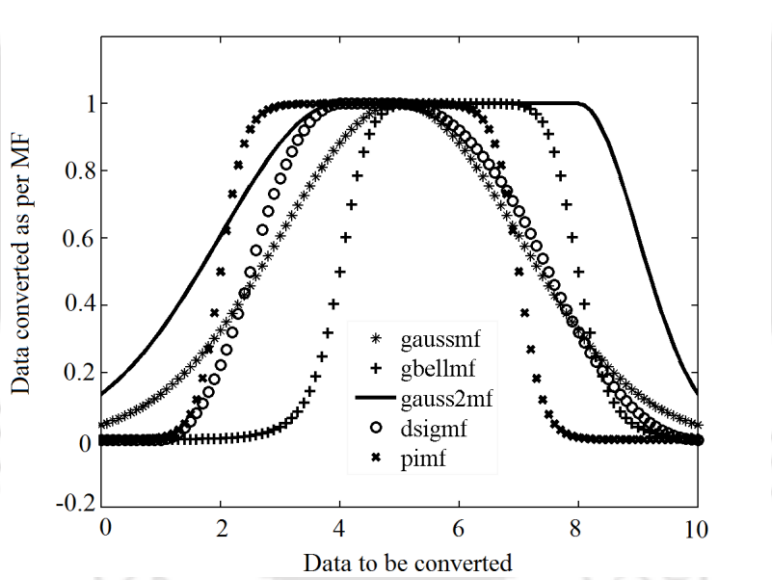

Fig. 6.4 Various types of membership functions (MFs)

The input MFs available are widely classified as Piecewise Linear Functions, Gaussian Functions, Bell-Shaped Functions, Sigmoidal Functions and Polynomial Based Functions and the output MFs as Linear and Constant. Out of these available input MFs, gauss MF, gauss2 MF, dsig MF, pi MF and gbell MF have been used in this study.

The gauss MF (Eq. 6.5) is of the shape of a Gaussian distribution, symmetric in nature and depends upon two parameters 'σ ', which is a measure of the width of the curve and '$\bar{c}$ ' that denotes peak value which is 1 in this case as shown in Fig. 6.4 .

$$f\left(x;\sigma,\bar{c}\right)=e^{\frac{-(x-\bar{c})^2}{2\sigma^2}} \tag{6.5}$$

Gauss2 MF is similar to gauss MF except that it is a combination of two 'σ ' and two '$\bar{c}$ '. The first 'σ ' and '$\bar{c}$ ' determines the shape of the left curve while the second 'σ ' and "$\bar{c}$ ' determines the right curve. A gauss MF facilitate obtaining smooth, continuously differentiable surface.

The generalized bell function or the gbell MF is also symmetric in nature and depends on three parameters $\bar{a}, \bar{b}, \bar{c}$ as (Eq. 6.6):

$$f\left(x;\bar{a},\bar{b},\bar{c}\right)=\frac{1}{1+\left|\frac{x-\bar{c}}{\bar{a}}\right|^{2\bar{b}}} \tag{6.6}$$

where, '$\bar{b}$ ' is usually positive and '$\bar{c}$ ' denotes the center of the curve.

A sigmoidal function depends on the two parameters '$\bar{a}$ ' and '$\bar{c}$ ' and is represented by (Eq. 6.7):

$$f\left(x;\bar{a},\bar{c}\right)=\frac{1}{1+e^{-\bar{a}(x-\bar{c})}} \tag{6.7}$$

Depending on the sign of '$\bar{a}$ ', the sigmoidal function is open to the right or to the left. The dsig MF is nothing but the difference between two such sigmoidal functions, which then looks more convenient.

The pi MF is a spline-based curve and derives its name from its Π shape. It depends on four parameters $\bar{a}, \bar{b}, \bar{c}, \bar{d}$. Parameters $\bar{a}$ and $\bar{d}$ determines the width at the bottom and $\bar{b}$ and $\bar{c}$ locates the shoulders. The membership function is represented by (Eq. 6.8):

$$f(x;\bar{a},\bar{b},\bar{c},\bar{d}) = \begin{cases} 0, & x \le \bar{a} \\ 2\left(\dfrac{x-\bar{a}}{\bar{b}-\bar{a}}\right)^2, & \bar{a} \le x \le \dfrac{\bar{a}+\bar{b}}{2} \\ 1-2\left(\dfrac{x-\bar{b}}{\bar{b}-\bar{a}}\right)^2, & \dfrac{\bar{a}+\bar{b}}{2} \le x \le \bar{b} \\ 1, & \bar{b} \le x \le \bar{c} \\ 1-2\left(\dfrac{x-\bar{c}}{\bar{d}-\bar{c}}\right)^2, & \bar{c} \le x \le \dfrac{\bar{c}+\bar{d}}{2} \\ 2\left(\dfrac{x-\bar{d}}{\bar{d}-\bar{c}}\right)^2, & \dfrac{\bar{c}+\bar{d}}{2} \le x \le \bar{d} \\ 0, & x \ge \bar{d} \end{cases} \quad (6.8)$$

All the MFs used in this study are shown in Fig. 6.4 which shows how data are mapped as per the shape of the MFs.

Besides MFs, various learning schemes like hybrid and back propagation are also available in ANFIS. Back propagation training method solely relies on the gradient descent technique whereas the basis for hybrid method includes least square method, apart from using gradient descent technique. The solution of back propagation method has a possibility of being misled by local minima but forward pass of hybrid algorithm uses least-squares method to identify the resultant parameters on the hidden layers and during backward pass, errors are propagated backward to update premise parameters by gradient descent.

Regulation of training of the ANFIS model can be done by either providing a minimum deviation between actual and targeted output or by putting constraint on the number of learning iterations, also known as epochs. During training, the weights associated with each neuron get updated with every iteration. Two types of fuzzy inference systems namely Mamdani-type and Sugeno-type are available in the Fuzzy Logic Toolbox of Matlab. The main difference between Mamdani and Sugeno is that the Sugeno output membership functions are either linear or constant. The present investigation deals with Sugeno type ANFIS network. A typical Sugeno Fuzy model works on the following principle [Jang and Gulley 1996]:

If x and y are two inputs then output is defined as:

$$z = \bar{a}x + \bar{b}y + \bar{c}\ . \tag{6.9}$$

For a zero-order Sugeno model, the output z is constant $\bar{c}\left(\bar{a}\ = \bar{b} = 0\right)$.

If w_i is the firing strength of a rule and the rule weighs the output level z_i by its firing strength, then for an AND rule associated with the inputs x and y, w_i is defined as:

$$w_i = AND\left(M_1(x), M_2(y)\right) \tag{6.10}$$

where, M_1 and M_2 are the membership functions for x and y.

Finally, the output of the system is the weighted average of all the rule output as:

$$Output = \frac{\sum_{i=1}^{N} w_i z_i}{\sum_{i=1}^{N} w_i} \tag{6.11}$$

where, N is the number of rules.

The parametric variation for determining optimum ANFIS model is described in detail in subsequent paragraphs.

6.3.2.1 Parameter variation in GTFG

Various types of input MFs are available in the ANFIS module of Matlab and a comparative study of the recovered heat fluxes using them is worth approaching. While the input MF is varied, all other parameters are affixed to certain constants to obtain the appropriate input MF for prediction purpose. The obtained result is plotted in Fig. 6.5(a).

The error in prediction of heat flux using pi MF is 3% however the obtained error are 33% and 30% using gauss MF and dsig MF, respectively. Therefore, pi MF has been able to represent the input data accurately and is accepted for further analysis. Similarly, the training algorithm comparison shows that hybrid algorithm is a better choice since error incurred using hybrid method is 3% while in FFBP the error is 25% (Fig. 6.5(b)). Finally, the comparison of output MF as in Fig. 6.5(c) shows that heat flux predicted with constant and

linear MF gives the same trend as the applied flux. However, the predicted peak value has an error of 3% using constant MF while linear MF shows an error of 38%.

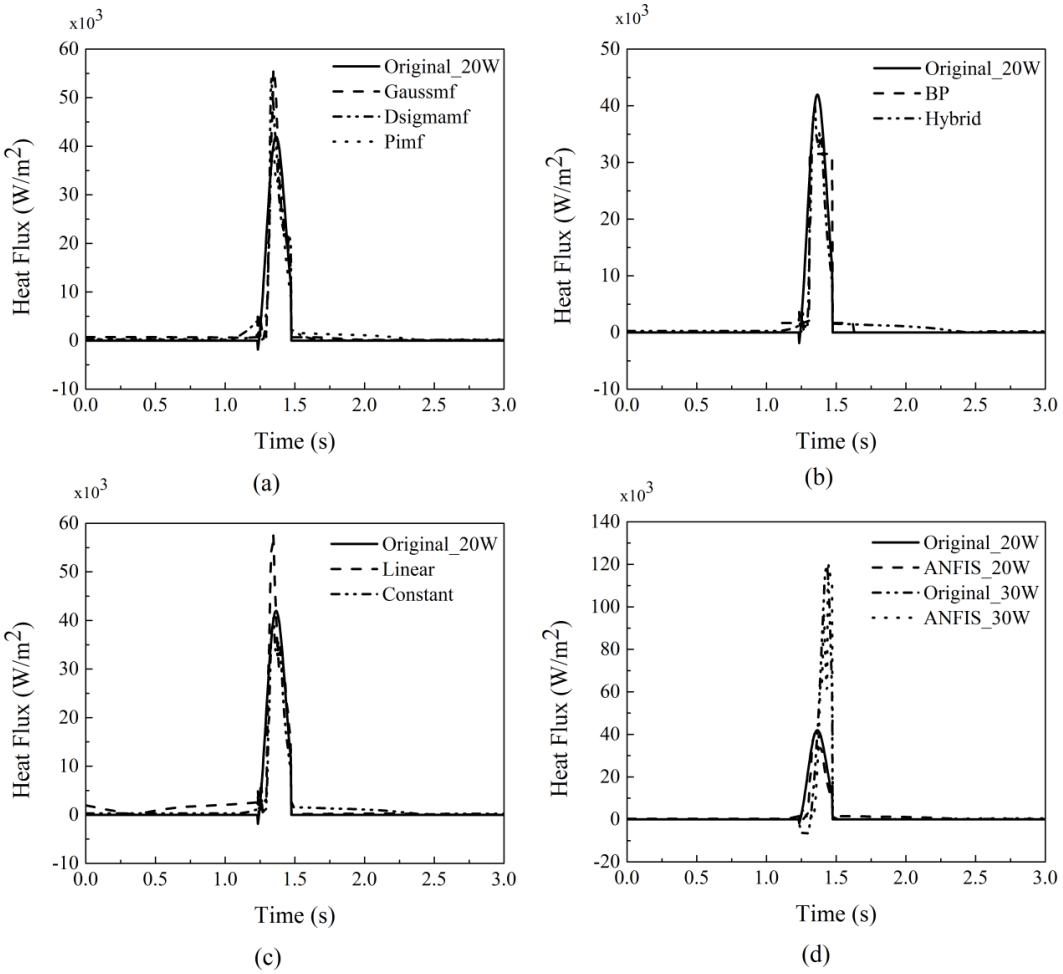

Fig. 6.5 Influence of variation of (a) input MF (b) training method and (c) output MF on prediction result of ANFIS and (d) validation of ANFIS model with testing data for 30 W heat load for GTFG

Hence, the optimum model for GTFG is fixed as pi MF as input MF, constant as output MF, hybrid as training method and number of epochs as 500. The optimum model of ANFIS designed by feeding 10 W and 40 W results as input and 20 W results as output is now used for predicting the heat flux (q''_{anfis}) corresponding to 30 W. It is seen from Fig. 6.5(d) that the model is successful in predicting the values with an error of less than even 1% in predicting 30 W heat load values.

6.3.2.2 Parameter variation in STFG

Similar to GTFG, parametric study is carried out for STFG as well. Comparison of influence of input MFs, training algorithm and output MFs in predicting output are shown in Fig. 6.6(a)

to Fig. 6.6(c). The peak heat flux predicted from gauss2 MF (two-sided Gaussian membership function) is the best choice and error in peak heat flux prediction is 2% compared to 20% and 22% in pi MF and gbell MF, respectively. Similarly, comparison of FFBP and hybrid learning algorithms ensures hybrid as a better choice to deal with as error incurred is 2% compared to 27% in FFBP. Taking gauss2 MF and hybrid method, when output MFs is varied, it shows that constant MF and linear MF has an error of 2% and 41% respectively.

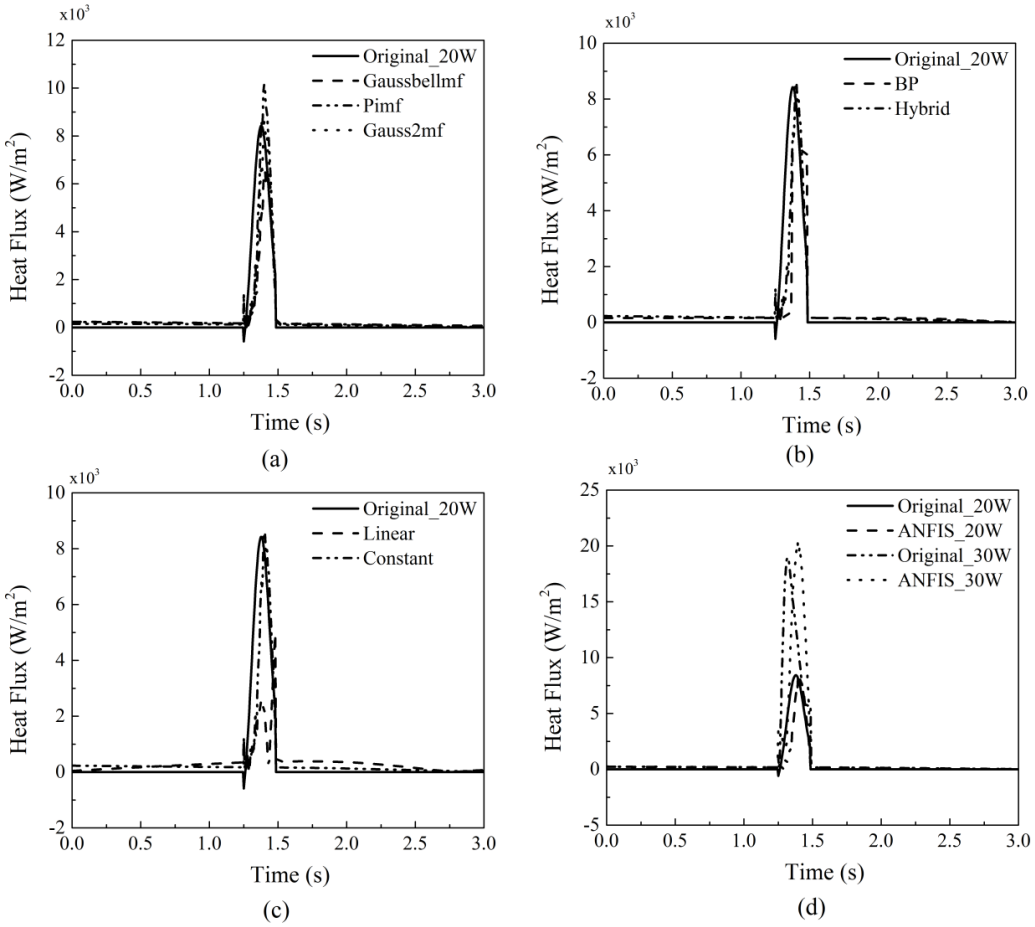

Fig. 6.6 Influence of variation of (a) input MF (b) training method and (c) output MF on prediction result of ANFIS and (d) validation of ANFIS model with testing data for 30 W heat load for STFG

Hence, the optimum ANFIS model for silver TFG is fixed as gauss2 MF as input MF, constant as output MF, and hybrid as learning algorithm where number of epochs is considered as 500. This optimum model of ANFIS designed for silver TFG, when fed with 30 W values as testing data shows nominal error of 7% in prediction of peak heat flux. The comparison of 20 W and 30 W data predicted by ANFIS optimized model and that obtained from experiment is plotted in Fig. 6.6(d).

6.3.2.3 Parameter variation in NCTFG

Identical parametric variations carried out on NCTFG conveyed that best results can be obtained when gbell MF is used as input MF (Fig. 6.7(a)).

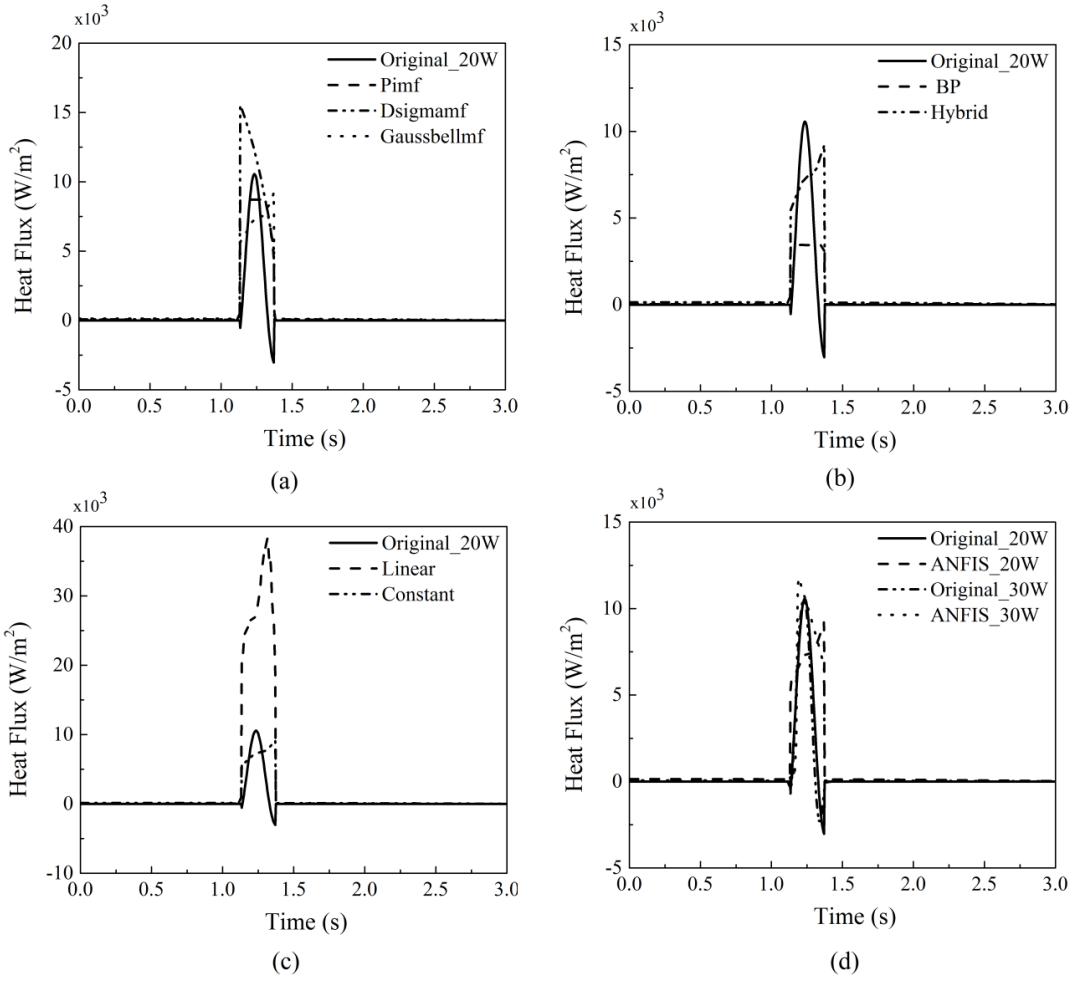

Fig. 6.7 Influence of variation of (a) input MF (b) training method and (c) output MF on prediction result of ANFIS and (d) validation of ANFIS model with testing data for 30W heat load for NCTFG

The deviation from the targeted peak value is found to be 12.5% when input MF is gbell MF as compared to 18% in case of pi MF and 47% in case of dsig MF as input MF. Similarly, consideration of FFBP as training algorithm results in an error of 67% while hybrid method shows an error of 12.5% for heat flux prediction. Finally fixing hybrid as learning algorithm and gbell MF as input MF, variation of output MF revealed an error of 12.5% attached with constant MF as output MF and an error of 257% attached with linear MF. Comparison of input MF, training algorithm and output MF for the composite TFG are shown in Fig. 6.7(a) to Fig. 6.7(c). Thus, after parametric study on the composite gauge, the optimum model is

frozen as: gbell MF as input MF, hybrid as the training algorithm and constant MF as the output MF and number of epochs as 500. The optimum model of ANFIS designed for composite gauge has been able to predict data for 30 W input values with an error of 11.5 % and the plot is shown in Fig. 6.7(d).

Table 6.1 Comparison of heat flux calculated analytically and predicted with optimum ANFIS model

TFG	Power Input (W)	Input Heat Flux (kW/m^2) (q''_{an})	Predicted Heat Flux (kW/m^2) (q''_{anfis})	% Deviation
GTFG	20	41.7	40.4	3
	30	119.9	119.4	4.2
STFG	20	8.4	8.57	2
	30	18.96	20.35	7
NCTFG	20	10.3	9	12.5
	30	10.52	11.73	11.5

During the present study, it is seen that constant MF and hybrid acts best as output MF and learning algorithm respectively, for all the gauges and the difference comes only in input MFs. In addition, it is noticed that after a certain number of epochs, hybrid learning becomes independent of number of epochs unlike in FFBP learning rule. The total time shown in heat flux prediction is 3 s since the subsequent 2 s data are all equivalent to 0. The peak values from prediction matches closely with experimental values. Values of heat flux predicted using ANFIS (q''_{anfis}) for all the TFGs are tabulated in Table 6. 1. However, slight deviation is observed in terms of trend prediction.

6.4 Prediction of thermo-electrical properties of TFG

The values predicted by the three optimized ANFIS model, one for each of the TFGs namely GTFG, STFG and NCTFG is now used to determine the relation between electrical and thermal properties of the respective TFGs. The performance of the ANFIS is benchmarked with the results of analytically calculated values of heat flux from transient surface temperature history of the thin film gauges. It is noted that testing case of ANFIS models are able to give a successful prediction rate of 97% ,93% and 87.5% on an average for heat fluxes in case of gold, silver and composite TFG, respectively. In order to show the relation between change in resistance and thermal conductivity per unit length with change in temperature of the gauges, surface plots have been generated where these three parameters

viz. “resistance”, “heat flux” and “thermal conductivity per unit length” are plotted along the three axes of the co-ordinate system.

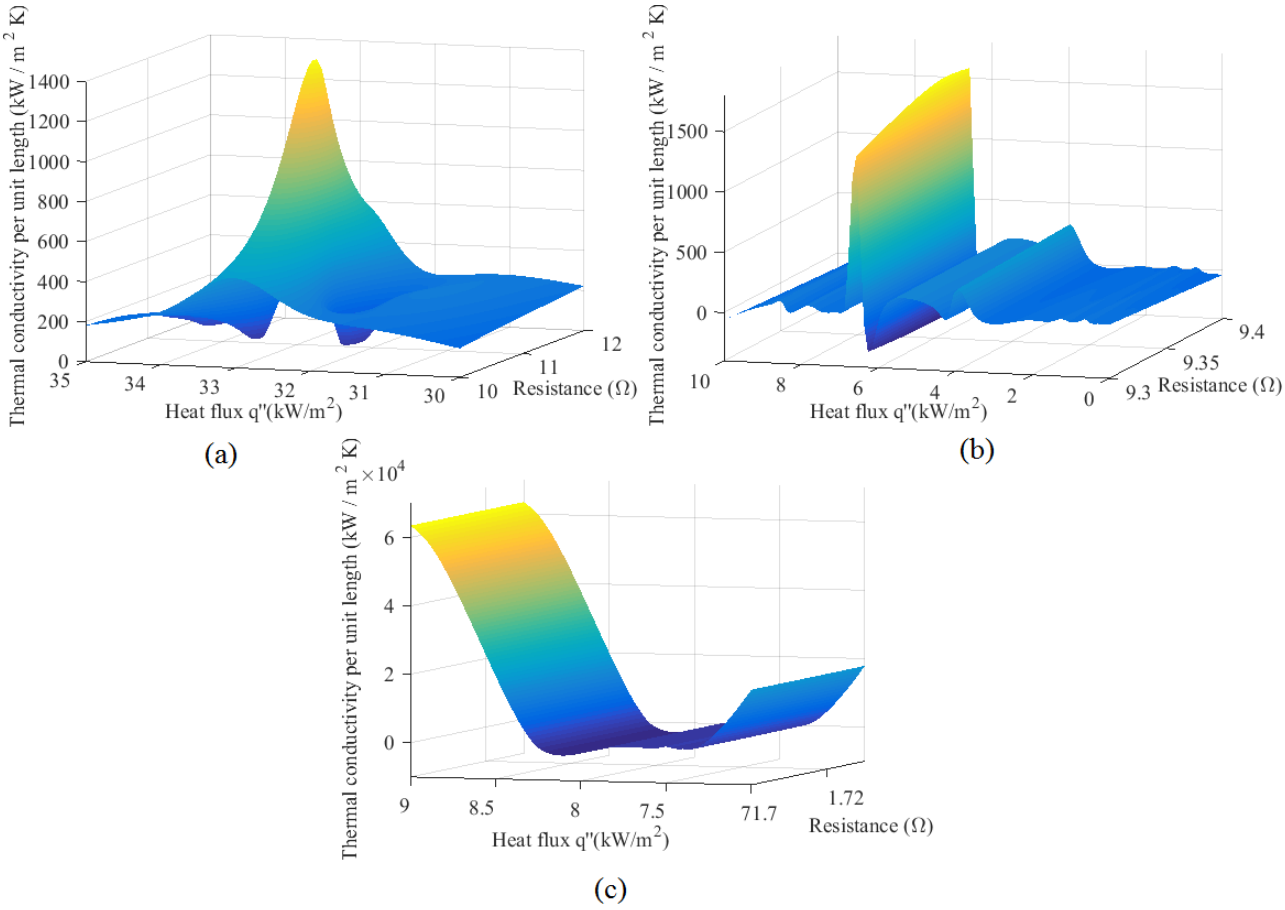

Fig. 6.8 Surface plot showing variation of temperature difference, resistance and thermal conductivity per unit length of (a) GTFG (b) STFG and (c) NCTFG

Fig. 6.8(a) to Fig. 6.8(c) shows the respective surface plots for gold, silver and composite TFG. Thus, any point on the temperature difference axis can immediately give the corresponding values of resistance and thermal conductivity per unit length of the gauge. The value of thermal conductivity can be calculated by multiplying thermal conductivity per unit length with the film thickness. Film thickness can be measured previously using surface profilometer or from the digital thickness monitor in a vacuum coating machine while coating the film itself. Thus, efficiency of ANFIS in predicting non-linear relations between electrical and thermal properties of TFGs at any temperature difference can be very well opined through this study.

6.5 Conclusion

An attempt has been made to develop a soft computing model to predict heat fluxes from temperature history and thereby revealing the non-linear relation between the thermal and electrical properties in TFGs. Two models, ANN based and ANFIS based have been worked out to predict heat flux with transient temperature history as input. Experimentally obtained transient temperatures and analytically deduced corresponding heat fluxes are used for training/testing the model. ANFIS model is found better than ANN in predicting heat fluxes. The values predicted are then used to relate the non-linear relation between thermal and electrical properties of thin film gauges. Finally, it is shown that ANFIS can be an apt tool in predicting the heat fluxes with an accuracy of 97%, 93% and 87.5% for GTFG, STFG and NCTFG, respectively. In addition, having the initial encouraging results from the ANFIS based thermo-electrical prediction model, further application of the model might be extended to other areas including multi-layer composite TFG.

Chapter 7

Synthesis and characterization of nanomaterials and multilayer TFGs

7.1 Introduction

Since their discovery by Ijima in 1991 [Ijima 1991], CNTs have persistently drawn attention from researchers worldwide due to their unique properties [Hone et al. 2002, Li et al. 2007]. Out of several possibilities of CNT growth, catalytic growth using CVD system is cited as the easiest and most confirming process [Kong et al. 1998, Kong et al. 1998, Ducati et al. 2002]. The catalyst layer, which is either sputtered or electrodeposited, plays a vital role in the growth and quality of the nanotubes formed. Researchers electrodeposited nickel nanodeposits on n-Si substrate in the presence of sulfuric acid and grew carbon nanotubes using CVD method [Zanganeh et al. 2014]. Out of several catalysts that assist in the growth of CNTs, Ni is the most effective and easily available one. Chemical vapor deposition (CVD) growth of carbon nanotubes directly on nickel substrates at different temperatures has been studied by Du and Ning with addition of Fe nanoparticles to enhance nanotube density [Du and Ning 2005]. In case of CNT/Me composites however, electrodeposition has received wide acclamation from the research community [Guo et al. 2008, Kim and Oh 2011, Diasio 2011, Lee 2012]. It is preferred for the obvious reason of being simple and cost-effective compared to vacuum coating and sputtering processes. Ni-CNT composite coatings, processed by electrodeposition were investigated for hardness and corrosion characteristics with variations of CNT concentration [Lee 2012]. In continuation with the previous work done, here a combination of CVD and electrodeposition is adopted to construct a multilayer composite film with alternate layers of Ni and CNT.

The quality and method of CNT formation is studied and the ability of a single CNT film and the multilayer composite film to serve as the sensing element in TFGs is also judged. Ni is chosen because it plays the dual role of being a good conductor and catalyzing CNT growth and CNTs are considered because of the obvious reason of bearing extraordinary thermal/electrical properties. A pure Ni layer and a DLC:Ni layer is used as catalyst to assist the CNT growth for the monolayer structure, however for the multilayer structure only electrodeposited Ni could succeed for the required purpose. A thin layer of Ni

is electrodeposited on p-Si and then alternate layers of CNT and Ni are grown with LPCVD and electrodeposition respectively. Several surface characterization techniques like Scanning Electron Microscopy (SEM), X-ray Photoelectron Spectroscopy (XPS), X-ray Auger Electron Spectroscopy (XAES), Raman spectroscopy, Optical Reflectivity and electrical measurements like TCR and Hall-coefficient measurements are carried out to check the quality of the films produced. The sensitivity of the composite film is found to increase with more CNT layers, despite the fall in TCR. On the other hand, the initial resistance is found to increase. Results indicate that these composite layer structures are appropriate for fabricating highly efficient Thin Film Gauges (TFGs). Fig. 7.1 shows the flowchart of the present work (Fig. 7.1(a)) and a schematic diagram (Fig. 7.1(b)) of the composite film under consideration.

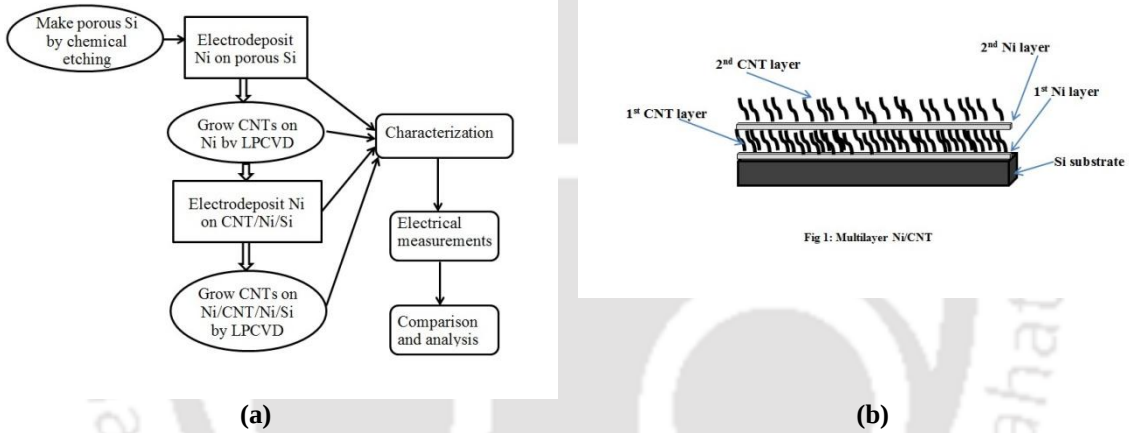

(a) **(b)**

Fig. 7. 1(a) Flowchart depicting the flow of present work (b) Schematic of the composite film

7.2 Experiment

7.2.1 Substrate preparation

Four types of substrates are used for the present study of CNTs which includes polished and unpolished p-type Si, DLC:Ni sputtered Si and porous Si. All the substrates are cut into small pieces of square shapes to facilitate their loading into the CVD chamber and on the Van der Paw probe for electrical measurements. The substrates are all cleaned in an ultrasonic bath in iso-propanol for 20 min to clear off any impurities that might stick to the surface.

The DLC:Ni substrates are prepared by sputtering a thin layer of DLC:Ni on Si with 5 W Ni and 50 W C simultaneously, on a rotating target for 30 min.

For the porous substrates, a thin layer of Ag of 10nm thickness is sputtered on a normal p-Si (100) wafer that is annealed at 300℃ for about 20 s to create Ag nanoparticles, the major

factor behind creating porous Si. The substrates are then etched in a 50ml solution of 4.8% HF and 0.6% H_2O_2 for different times (5, 10, 20 and 40 min). After etching, the samples are dried with a hand pump and made ready for galvanic deposition of Ni on it. However, except porous Si, the other three types were not successful enough in creating strong adhesion between the subsequent layers; hence, only porous Si substrates are accepted for the multilayer structures. The choice of a good substrate is explained in the subsequent heading of "Results and Discussion".

7.2.1.1 Deposition of catalyst films by galvanic deposition

An aqueous solution of Bright Nickel solution (Watts bath) with following ingredients are used for depositing Ni on the previous mentioned substrates: Nickel sulphate hexa hydrate ($NiSO_4.6H_2O$) 150g/L, Nickel Chloride hexa hydrate ($NiCl_2.6H_2O$) 60g/L and boric acid 37g/L. A pure Nickel wire is made the anode while the porous Si substrates serve as the cathode. While the solution is continuously stirred in the beaker, the applied voltage is fixed at 5V (DC) and the temperature is maintained in the range of 40˚C-60˚C. Several deposition times are tested; such as 0.5, 1, 2, 5 and 10min are tested on the porous Si substrates and 5, 10, 15, 20 and 30 min deposition are tried on polished and unpolished Si substrates. The films deposited for more than 20 min on polished/unpolished Si are very thick and wears out themselves. Similar is the case for films deposited for more than 5 min on the porous Si substrates. In case of polished/unpolished Si, films deposited for less than 10 mins are too thin and not continuous. After several trials, the polished/unpolished Si substrates with deposition time of 10, 15 and 20 min and porous Si substrates with 0.5, 1, 2 and 5 are selected for growing the first layer of CNTs on it. After the CNTs were grown, all of the substrates with Ni/CNT (Ni/polished Si, Ni/unpolished Si, Ni/DLC:Ni, Ni/porous Si) are again electrodeposited with Ni using the same Watt's solution.

7.2.2 Synthesis of CNT films by LPCVD

The LPCVD incorporating catalyst-assisted thermal decomposition of hydrocarbons is used for CNT growth. The LPCVD system consists of a quartz tube coupled with a furnace, a rotary pump for evacuating, two cylinders each for the process and carbon source gases and pressure sensors. In our case, Acetylene is the carbon source gas and Argon is the process gas. The Ni/Si substrates are positioned carefully in an alumina crucible and introduced into the quartz chamber. Subsequently, the system is evacuated down to a base pressure of 5.6 $x10^{-3}$ mbar. Once the pressure is stabilized, the chamber is heated in ramp up to 700˚C under

Argon flow. At such high temperature and low pressure, when acetylene encounters Ni, acetylene is broken apart at the surface of the catalyst (Ni) particle, and the carbon is transported to the edges of the particle, where it forms the nanotubes. A flowrate of 20 sccm of Acetylene and 100 sccm of Argon are used for a total time of 5, 15 and 40 mins for CNT growth.

7.2.3 Characterization

For obtaining morphological, microstructural and analytical information, the obtained composite film is observed at every step using a high-resolution Scanning Electron Microscope with a W filament (JEOL JSM-6390LV) and equipped with both an EDS and a WDS with an Oxford INCA microanalysis suite.

For Raman spectral analysis, the samples are examined in the back-scattering geometry using a LabRam HR spectrometer (HORIBA) equipped with Peltier - cooled charge coupled detectors. A 100X standard objective (1 μm focus spot) and laser power lower than 1 mW is used to avoid any laser heating induced effects or photodecomposition, with excitation provided by the 514.6 nm line of a diode laser.

The elemental composition, chemical structure and electronic state of the samples are measured with an X-ray Photoelectron Spectra (XPS) and X-ray-excited Auger Electron Spectra (XAES), which are acquired in an Axis Ultra DLD system by Kratos Analytical using a monochromated Al-Ka1 X-ray beam as the excitation source. The analyzed area has an elliptical shape with the two axes being 400 and 700 μm. The pass energy is 160 eV for survey scans and 20 eV for HR spectra; for the latter case, the pass energy results in a broadening (FWHM) of less than 500 meV for the Ag-3d line. Data interpretation is performed with the Kratos-Vision software.

A four-point probe setup is used to measure the electrical conductivity, mobility of the samples. The four probes hold the samples at the periphery with pressure instead of glue, which reduces contact resistance caused by conductive silver epoxy otherwise. The setup consists of a probe with four tungsten metal tips to hold the samples, a Teslameter along with a magnetic probe to measure the applied magnetic field, a variable current source to apply current through the samples, a multimeter (HP 34401 A), a high resolution data logger (PICO) to transfer the data into the PC. A PID controlled oven (PID-200) is connected to the four probe setup that allows heating of samples up to 200˚C in order to measure their TCR. Square samples of size 5mm × 5mm are used for the measurements (*Appendix B*). Current is

passed across two probes, the corresponding voltage across the other two probes is noted, and the sheet resistance is measured.

The optical reflectivity spectra are acquired in the range of (450-850) nm using a white light halogen source, a coaxial fiber-optic assembly and a detector. The reflectivity spectra are normalized using a reference mirror of silicon.

7.3 Results and discussion

7.3.1 Substrate selection

The initial notion was to grow Ni on polished p-type Si (100) substrates and grow alternate layers of CNT and Ni on it. However, it is observed that although the Ni grown on the polished substrates are successful to catalyze the CNT growth, yet the adhesion between layers becomes an issue of concern. Needless to mention that the second Ni layer could not be topped on the CNT/Ni layer and therefore the other measurement could not be repeated (Fig. 7.2). It has been reported that Ni-CNT coatings display poor adhesion of CNTs to the Ni matrix [Lee 2012]. They opine that the corrosion resistance of such composites fails dramatically due to the porous microstructure [Lee 2012].

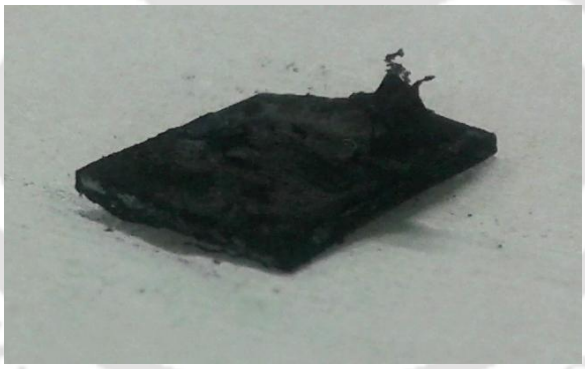

Fig. 7.2 Poor adhesion of CNT/Ni/CNT film

After several unsuccessful trials with normal Si, DLC:Ni substrates are chosen as an alternative yet the multilayer could not be achieved. Finally, the idea of making rougher substrates and thinner layers is adopted to increase adhesion between the layers. Therefore, unpolished and porous Si is opted as the next candidates. After several trials, porous Si is successful to hold firm the Ni and CNT layers on it. The substrates etched for 5 min are not sufficiently porous whereas those above 10 min are extremely porous with respect to our study and therefore 10 min etching is considered as the best option. Ultimately, the best possible option comes out as 30 s electrodeposition of Ni on the 10 min etched Si and 5 min

of CNT synthesis on the electroplated Ni layers. It is worth mentioning here that further reduction of deposition time results in discontinuous films of CNT. Fig. 7.3 shows the samples with porous substrate, Ni deposited substrate, single and bilayer CNT/Ni structure.

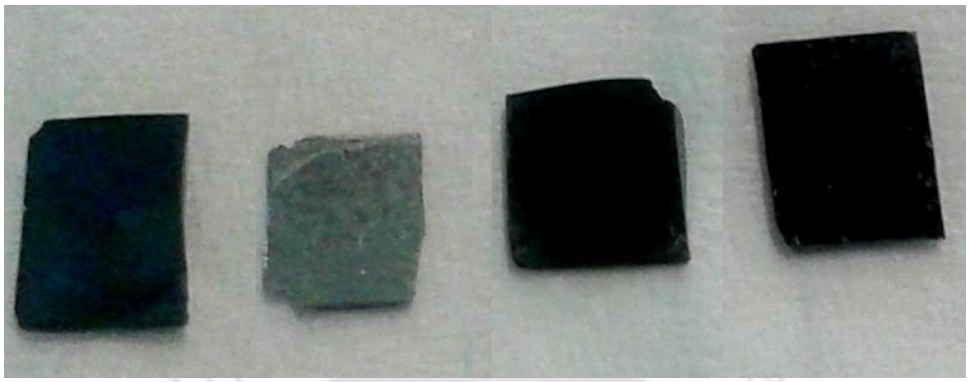

Fig. 7.3 From left porous Si substrate, Ni/Si, CNT/Ni/Si and CNT/Ni/CNT/Ni/Si films

7.3.2 Surface morphology

The surface morphology and thickness of all the CNT samples are studied with SEM. Fig. 7.4(a) and Fig. 7.4(b) shows the cross sectional view and planar view of porous Si at a magnification of 300 X and 50 kX, respectively. Pictures show the nanopores created by the Ag nanoparticles that are formed by annealing before etching the Si in the solution. The etching depth is calculated to be around 46 µm. Fig. 7.4(c) shows the surface of the electrodeposited Ni on the porous Si at a magnification of 50 kX. As is evident from the picture, the Ni grains are uniform and make a continuous film even for a short deposition time of 30 s. The size of the Ni grains varies in the range of 400 nm to 800 nm. The roughness created by the nanopores has alleviated the formation of Ni film on the Si substrate.

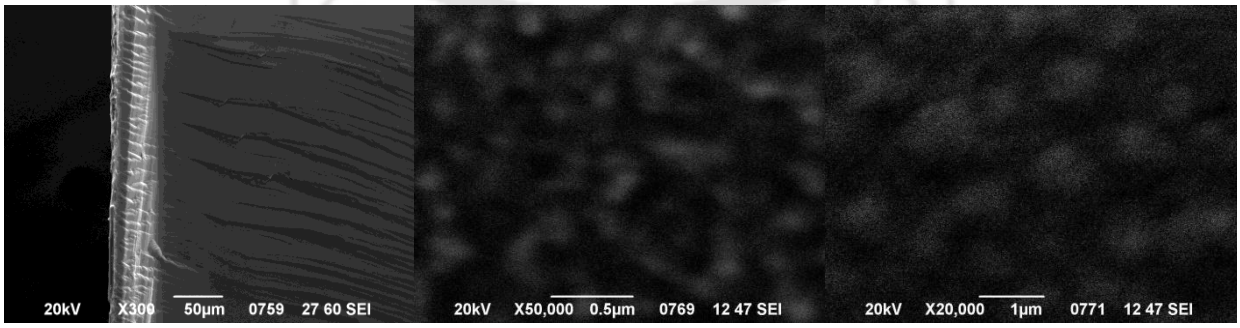

(a) (b) (c)

Fig. 7.4 SEM of (a) cross-sectional and (b) planar view of porous Si and (c) electroplated Ni/Si

Fig. 7.5(a) and Fig. 7.5(b) show the surface of the single layer CNT/Ni film at a magnification of 1 kx and 20 kx, respectively. Fig. 7.5(c) and, Fig. 7.5(d) show plane view of single layer CNT/Ni film grown over electroplated Ni at a magnification of 25 kX and 40 kX respectively while Fig. 7.5(e) and Fig. 7.5(f) show the surface of bilayer CNT/Ni film at a magnification of 10 kX and 20 kX respectively.

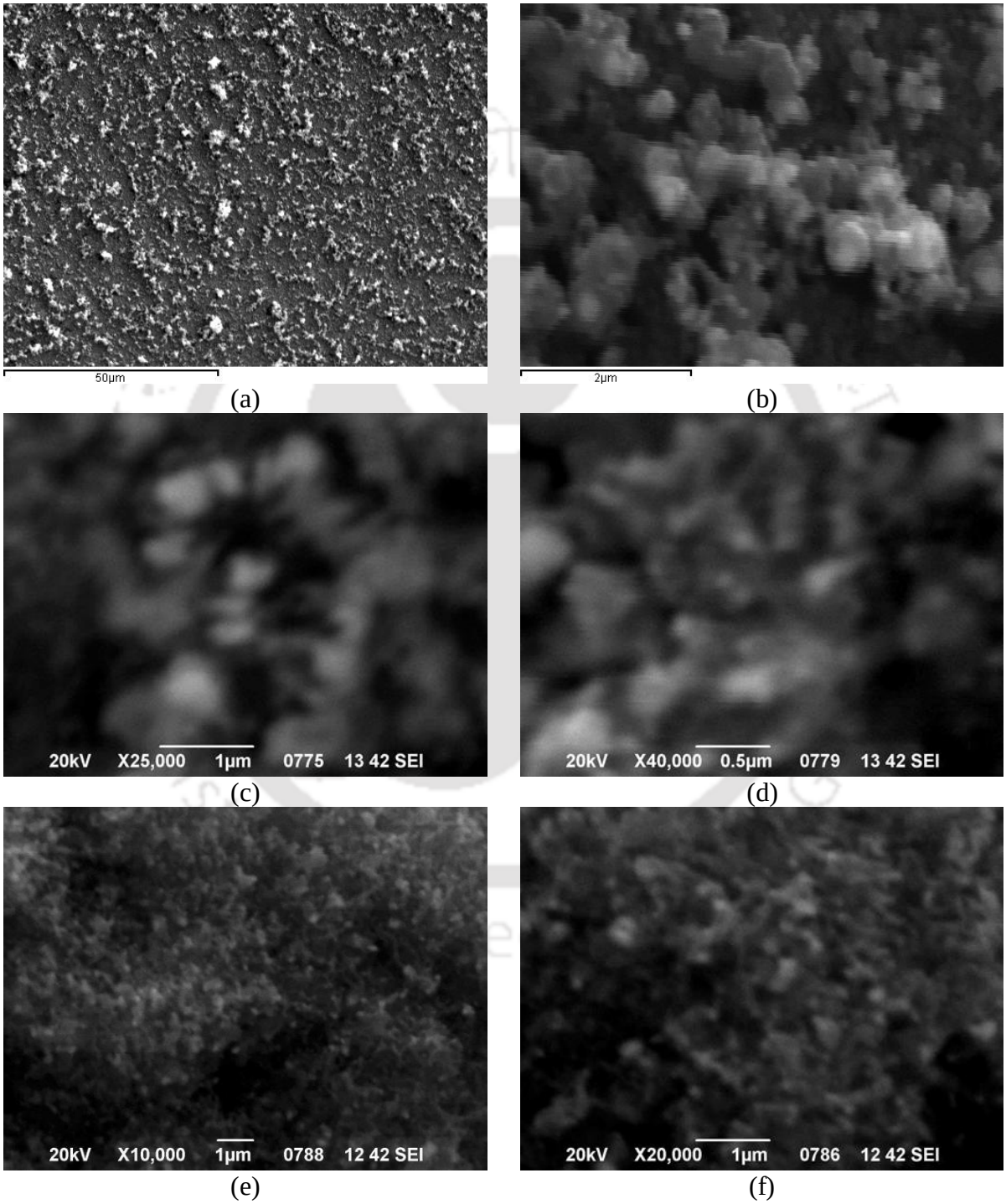

(a) (b) (c) (d) (e) (f)

Fig. 7.5 SEM photographs of (a/ b) single layer CNT/DLC: Ni at a magnification of 1 kx and 20 kx respectively, (c/ d) single layer CNT/Ni, and (e/ f) bilayer CNT/Ni films

Numerous nanotubes could be viewed in the photographs and the diameter of the CNTs in DLC: Ni substrates were 240 nm on an average while those on Ni substrates varied in a range of 100-400 nm in case of monolayer CNT/Ni film and 80-100 nm in case of the bilayer film, respectively.

7.3.3 Chemical structure (XPS/Raman/AES)

XPS is used for the identification of elements and the nature of bonds present within the composite multilayer structure. The pass energy is 20 eV. The C-1s and Ni-2p envelopes analyzed for the composite structures are detailed below. The presence of $Ni(OH)_2$ or NiO is confirmed by the presence of peaks at 856.5 eV (Fig. 7.6(a)) for the Ni $2p_{3/2}$ of the Ni/Si film (before annealing) [Kim and Winograd 1974, Mansour 1994]. The peaks at 861.8 is a satellite peak (could be created by strong interaction between metal and oxide interfaces) for the main peak of $Ni(OH)_2$ [Marchetti et al. 2015]. The other two peaks at 874.3 and 880.2 is the accompanying doublet because of spin orbit splitting which is supported by the peak ratios ($Ni2p_{1/2}$: $Ni2p_{3/2}$) = 1:2 and their equal FWHM [http://xpssimplified.com]. Similar accompanying doublets are also visible in the next two spectra (Fig. 7.6(b) and Fig. 7.6(c)). The peak at 856.5 disappears in the next 2 spectra (Fig. 7.6(b) and Fig. 7.6(c)) indicating desorption of the hydroxyl group after annealing. The peaks at 853.9 and 852.6 in Fig. 7.6(b) can be attributed to traces of residual oxides (NiO) left after annealing [Dickinson et al. 1977, Bianchi et al. 1993, Dube et al. 1995] and metallic Ni [Venezia et al. 1995, Li et al. 1984], respectively and the rest two peaks at 869.6 and 871.2 are the accompanying doublet. The peaks at 854.9 and 852.6 in the bilayer CNT/Ni structures (Fig. 7.6(c)) also imply the presence of residual NiO [Matienzo et al. 1973] and metallic Ni respectively [Venezia et al. 1995, Li et al. 1984, Cao et al. 2009] and the peak at 861.8 must be the satellite peak for the main peak of 854.9. Further, the C1s spectra for the monolayer and bilayer CNT/Ni structures are shown in Fig. 7.7(a) and Fig. 7.7(b) respectively. The peaks at 284.55 and 285.15 imply the presence of sp^2 and sp^3 bonded carbon respectively, whereas the other two peaks at 286.65 and 290.35 could be due to presence of C-O and C-OO from atmosphere [Kovacs et al. 2008] (Fig. 7.7(a)). Similar peaks for carbon are present in the bilayer structure (Fig. 7.7(b)) and the peaks at 286.35 and 290.55 are contribution from C-O and C=O (from ambience) respectively [Kovacs et al. 2008].

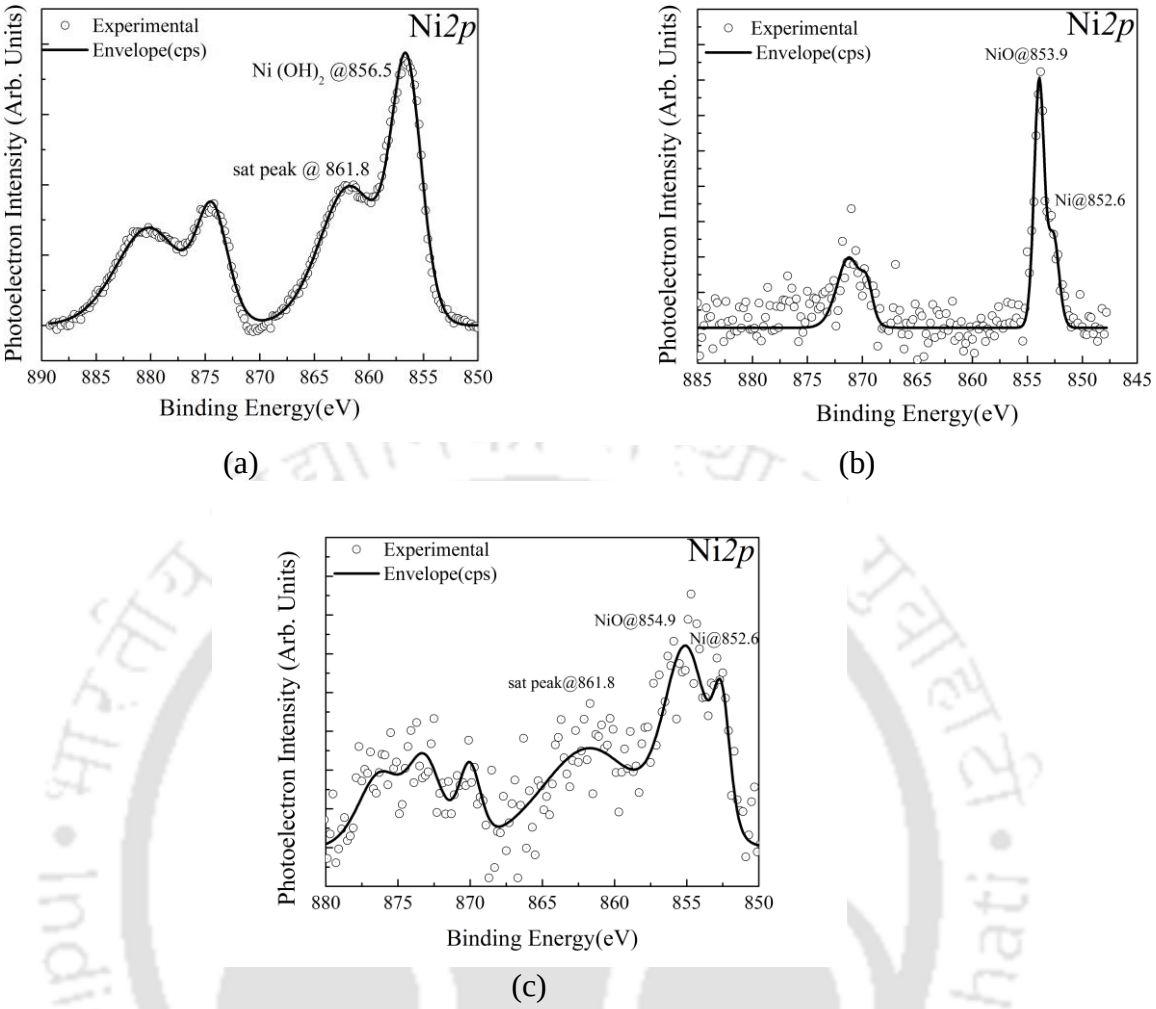

Fig. 7.6 XPS spectra of Ni 2p envelope for (a) only Ni (b) single layer CNT/Ni and (c) bilayer CNT/Ni films

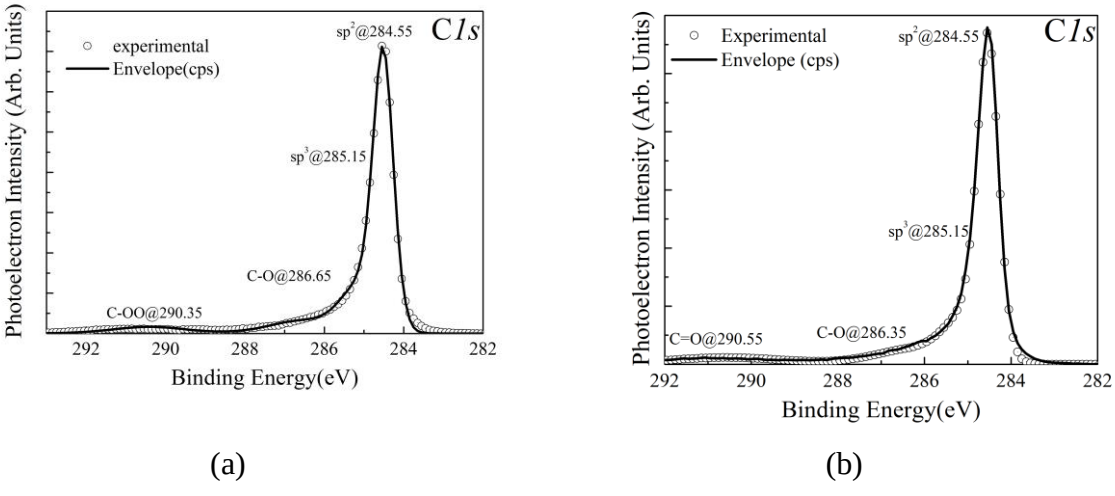

Fig. 7.7 XPS spectra of C-1s envelope of (a) single layer CNT/Ni and (b) bilayer CNT/Ni structure

The as-deposited sample exhibited predominantly sp^2 CC bonds and a minority of sp^3 CC bonds indicating lesser excellence in the quality of the CNTs grown which is also supported by the Auger and Raman spectra later. The peak assigned to the CC sp^2 bonds exhibits a broad full width at half-maximum (FWHM) of 1.6 eV which implies increase in surface deformations in CNT [Brzhezinskaya and Vinogradov 2010]. The reduction in oxygen however is quite evident (Table 7.1) as a direct result of annealing. NiO_2 decomposes after 600 ˚C and then Ni is wrapped into carbon and is protected from oxidation.

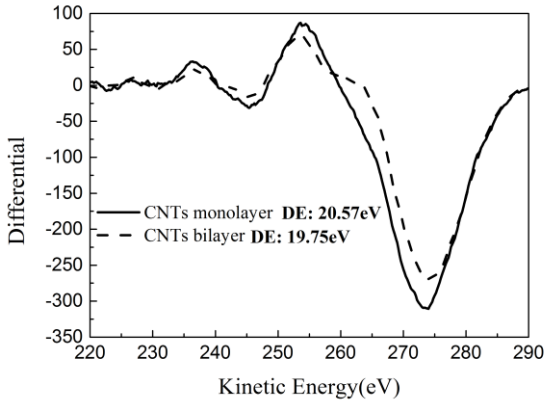

Fig. 7.8 X-ray Auger electron spectroscopy

Table 7.1 XPS spectra details of the as grown Ni/CNT samples

	Peak	Position	FWHM	Height	At. (%)
Ni	C1s	284.55	3.671	4895.7	30.37
	O1s	532.35	3.466	30648	62.86
	Ni2p	856.5	4.249	19229.3	6.77
CNT/Ni	C1s	284.55	0.642	71377.3	96.06
	O1s	533.6	1.727	8596.7	3.82
	Ni2p	853.9	0.911	1573.8	0.12
2CNT/Ni	C1s	284.55	0.607	57912.5	99.26
	O1s	532.7	3.531	1196.3	0.68
	Ni2p	854.9	3.568	654	0.06

The X-ray Auger electron spectrums for the monolayer and bilayer Ni/CNT composite films are shown in Fig. 7.8. Juxtaposition of the two spectra reveals that there is hardly any peak shift indicating that the quality of CNTs grown are of similar quality. Considering the D

factor (delta factor is the distance between the hill and valley in the Auger spectra) of graphene (purely sp^2; dE=21 eV) and diamond (purely sp^3; dE=13 eV), the sp^2 content in monolayer (20.57 eV) and bilayer structure (19.75 eV) comes out to be 94.6% and 84.4 % respectively.

Raman spectroscopy is also used to evaluate the structural quality of the produced CNTs. The spectra show two dominating features: two sharp Raman peaks, namely G (graphite)-, D (disorder)-bands are seen. The G band consists of two peaks, G and D´ (most prominent ones) which are related to the lattice vibration of sp^2 bonds of carbon. In our case, the modes G and D´ occurs at 1582.12 cm^{-1} and 1617.2 cm^{-1} while the D peak is observed at 1352.38 cm^{-1} for the monolayer CNT/DLC: Ni film. For monolayer CNT/Ni films, G and D´ peaks occurr at 1583 cm^{-1} and 1619 cm^{-1} respectively and for the bilayer CNT/Ni film; these are found at 1580 cm^{-1} and 1614 cm^{-1} respectively. The D band occurs around 1346 cm^{-1} and 1348 cm^{-1} respectively for the monolayer and bilayer structures (CNT/Ni). The ratio of D and G bands (I_D/I_G) reveals the degree of disorder in the graphitic sheets. The value of (I_D/I_G) is calculated as 0.42, 1.89 and 1.36 in the monolayer CNT/DLC: Ni, CNT/Ni and bilayer CNT/Ni films, confirming the best quality CNTs being synthesized on DLC:Ni substrates. The FWHM, peak position and the (I_D/I_G) ratios are listed in Table 7.2. Fig. 7.9(a), 7.9(b) and 7.9(c) shows the Raman spectra of the monolayer CNT/DLC:Ni, monolayer CNT/Ni and bilayer CNT/Ni films and Fig. 7.9(d) shows the two plots juxtaposed together (mono and bilayer CNT/Ni). Inspection of Fig. 7.9(d) displays that there is hardly any shift in the peak positions for both layers. This means that the quality of CNT grown is equivalent both the times and would not change with addition of new layers.

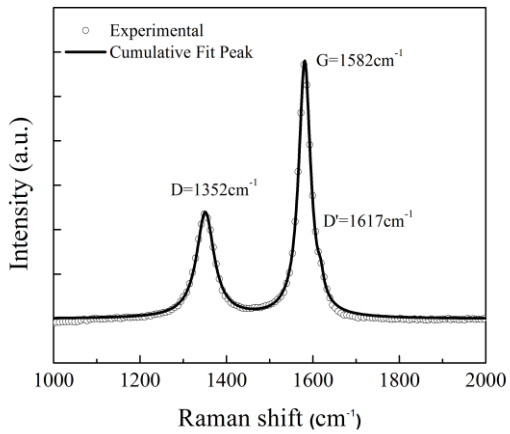

(a)

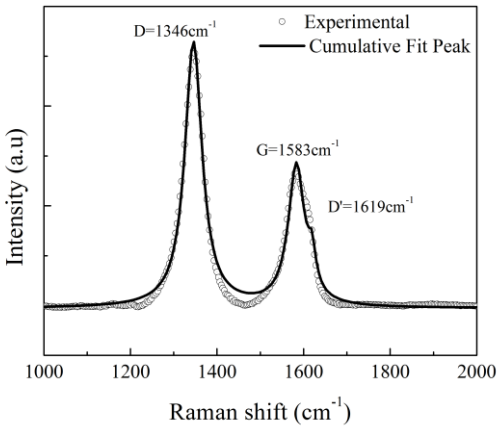

(b)

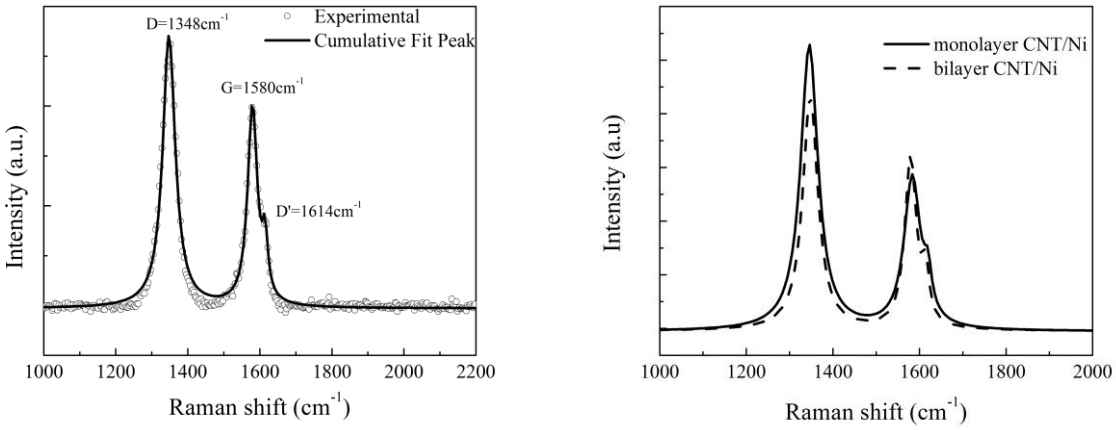

Fig. 7.9 Raman spectra of (a) monolayer CNT/DLC:Ni (b) monolayer CNT/Ni (c) bilayer CNT/Ni and (d) both juxtaposed

Table 7.2 Table showing peak position, FWHM and ID/IG ratios for the monolayer and bilayer films

		D	G	D'	I_D/I_G
Monolayer CNT/DLC:Ni	Peak center	1352.38	1582.12	1617.2	0.42
	FWHM	51.32	32.81	23.56	
Monolayer CNT/Ni	Peak center	1345.59	1583.2	1619	1.89
	FWHM	48.33	45.75	20.84	
Bilayer CNT/Ni	Peak center	1347.95	1579.55	1614.27	1.36
	FWHM	42.55	32.31	18.1	

As reported earlier, lower (I_D/I_G) ratios and sharper D, G peaks correspond to more aligned and ordered CNTs [Chhowalla et al. 2001] which is shown in CNTs on DLC: Ni substrates. In case of Ni substrates though, despite having sharper peaks, higher (I_D/I_G) ratios imply disordered/ unaligned CNTs. Position and intensity of the peaks are however, in agreement with literature [Chhowalla et al. 2001, Bokobza and Zhang 2012].

7.3.4 Electrical and optical properties

7.3.4.1 Van der Paw measurement

The sheet resistance and Hall coefficients of the films are measured using a Van der Paw setup with four leads attached on the four corners of 5 x 5 mm^2 square samples. Fig. 7.10 shows the change in resistance with respect to change in magnetic field of the samples.

The voltage-current relation is measured three times for each sample, each time using different probe (where the leads touches the sample) to pass the current and measure output voltage. The initial resistances of the CNT/DLC:Ni, Ni/Si, single CNT/Ni and double CNT/Ni films are measured as 0.64268 Ω, 0.00212 Ω, 0.00244 Ω and 0.1887 Ω, respectively. The presence of n-type carriers are detected through Hall measurement and the net carrier mobility decreases from -1607.3861 $cm^2/V.s$ in Ni/Si film to -89.6119 $cm^2/V.s$ in single layer CNT/Ni and to -71.1658 $cm^2/V.s$ in bilayer CNT/Ni film. The CNT/DLC:Ni holds a carrier mobility value as low as -28.5574 $cm^2/V.s$. These values justify the corresponding increase in initial resistance of the films. The resistances, hall coefficients, electron mobilities, resistivities, conductivities and sensitivities of the samples are listed in Table 7.3.

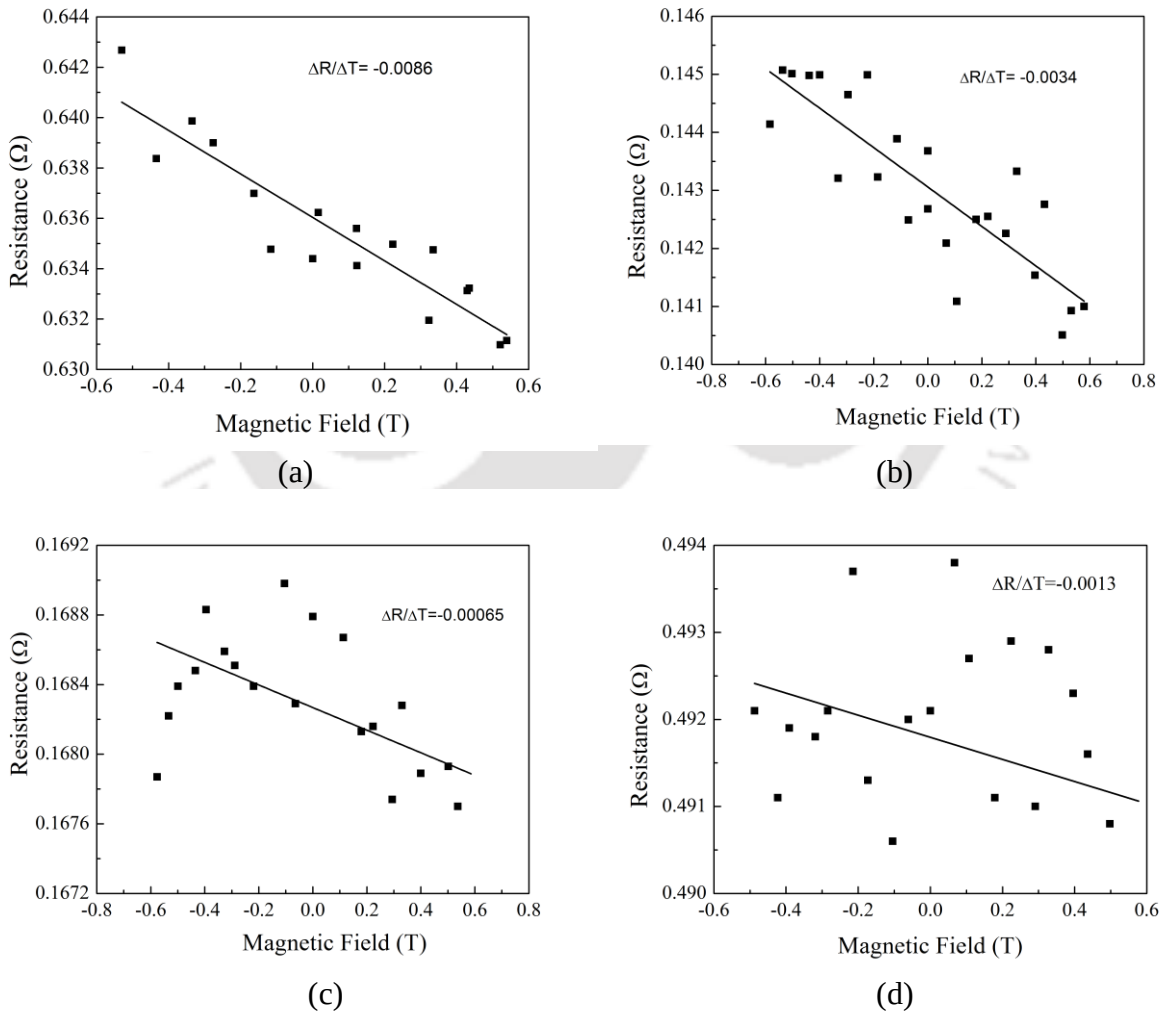

Fig. 7.10 Change in resistance of (a) single CNT/DLC:Ni (b) Ni/Si, (c) single CNT/Ni/Si and (d) double CNT/Ni/Si films with change in applied magnetic field

Table 7. 3 Table displaying resistivity, conductivity and carrier mobility of the films

Sample	Film thickness(m)	Resistivity (ρ) in Ω.cm	Sensitivity in V/°C	Conductivity (σ) in $\Omega.cm^{-1}$	Carrier mobility (μ) in $cm^2/V.s$
Monolayer CNT/DLC:Ni	2.70×10^{-6}	8.64×10^{-4}	3.3×10^{-3}	1157.41	-28.5574
Ni/Si	3.61×10^{-7}	7.64×10^{-7}	7×10^{-5}	1309586	-1607.39
Monolayer CNT/Ni	1.17×10^{-6}	7.81×10^{-6}	7×10^{-5}	128090.2	-89.6119
Bilayer CNT/Ni	1.71×10^{-6}	3.13×10^{-5}	2×10^{-4}	31938.68	-71.1658

7.3.4.2 Temperature Co-efficient of Resistance (TCR)

The sensitivity of a material determines its change in resistance with change in temperature and is a measure of its quality. However this time instead of the typical oil-bath calibration, a Van der Paw setup together with an oven is used to measure the TCR of the films. The highest temperature that can be applied is 200℃, as limited by the instrument. Keeping the temperature constant, the applied current is changed from 0 to 120 mA (as limited by the instrument) and the change in voltage is noted. The increase in sensitivity of the film is perceptible from Fig. 7.11, despite the fall in its TCR. For the films under consideration, the sensitivities of the double layer CNT/Ni/Si was seen to increase by 1.86% from the original Ni/Si film, whereas the sensitivity increase for the CNT/DLC:Ni film is 46.1% from the Ni/Si film. Moreover, there is a noticeable increase in initial resistance of the films with increase in CNT layers.

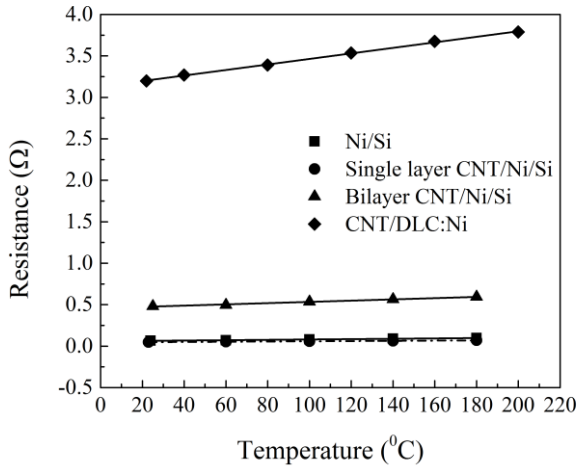

Fig. 7.11 TCR measurement of the composite films

The higher sensitivity and higher initial resistance for the CNT/DLC:Ni film is certainly due to the better quality of CNTs grown as confirmed by Raman spectroscopy (lower I_D/I_G value). Hence, the obvious question arises as in why DLC:Ni was not adopted for the multilayer study. The reason, as mentioned earlier is the poor adhesion of thin DLC:Ni layers on the CNTs. Therefore although it helped in synthesizing better quality CNTs, yet it would not have been able to hold together the subsequent layers (sputtering such a thin layer of Ni on CNT is itself very unstable). Thus, electroplated Ni is chosen as the alternative even at the risk of degrading the quality of the CNTs to some extent.

Initial resistance increase is due to the augmented pathways to travel for the heat wave and this might be used as the criterion to decide on the optimal number of layers. Moreover, the increasing size of the film must have also added to the initial resistance enhancement. Nevertheless, due to higher sensitivity, bilayer CNT/Ni seems more favorable for a TFG to sense lower heat fluxes with more accuracy.

7.3.4.3 Optical properties

The optical reflectivities of the films are studied in order to check their reflectivity, in the range of 400-850 nm wavelengths. The spectra of all the three films (Ni, monolayer CNT/Ni and bilayer CNT/Ni) are plotted in Fig. 7.12. The reflectivity of the electrodeposited Ni is in good agreement to the spectra reported in literature [Wang and Gallais 2013]. On the other hand, the monolayer and bilayer CNT/Ni films have zero reflectivity implying that they have full absorption.

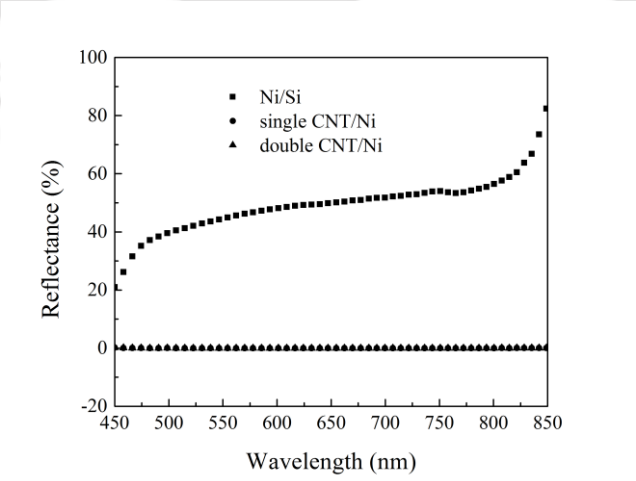

Fig. 7.12 Optical spectra of only Ni, single layer CNT/Ni and bilayer CNT/Ni films

7.4 Conclusion

A multilayer structure consisting of alternate layers of Ni and CNT films is developed. Ni films are electrodeposited and CNTs are directly grown on nickel substrates using CVD method. The effect of increase in number of CNT layers in the composite film is studied. Van der Paw measurements confirm that increase in layers of CNTs contributes to additional sensitivity of the composite film. Initial resistance, sensitivity and TCR of the final composite film are found to be 0.1887 Ω, 2 x 10^{-4} V/ ˚C and 1.06 x10^{-3}/℃, respectively. The electron mobility decreases from -1607.3861 cm^2/V.s in Ni/Si film, to -89.6119 cm^2/V.s and -71.1658 cm^2/V.s in the single and bilayer CNT/Ni films, respectively. The Raman spectra and SEM confirm the structural quality of the CNTs grown whereas the XPS and XAES spectra highlight the growth mechanism of the multilayer film. CNT/DLC:Ni has the least I_D/I_G ratio in Raman spectra and also is the highest sensitive towards temperature, confirming the fact that more aligned CNTs leads to more efficient (temperature sensing) film. However, in spite of giving the best quality CNTs, it is not successful in sticking the subsequent layers together. Hence, even at the cost of CNT quality electroplated Ni is chosen as the best option. Hence, through the study it is opined that this composite film could be used as TFGs to measure transient temperature in a relatively lower heat flux environment. Since the better conductivity of the film would help in more accurate deduction of heat flux from temperature histories sensed by the TFGs. To conclude, decrease of mobility and TCR with increased layers is expected but whether there are a critical number of layers where the decrease reaches a ceiling or the number reaches a plateau, is a matter of concern. Moreover, the number of layers is restricted by the dimensionality criterion of TFGs, superseding which would restrain the usage of one-dimensional heat flow condition assumed during the deduction of heat flux. Hence, it is expected that the optimal layers would get restricted to two or three layers. The exact number of layers required to have zero decrease eventually could be addressed in future work.

Chapter 8

Conclusion

8.1 Conclusion

The main objective of this study was to design and fabricate Thin Film Gauges having fast response time, high sensitivity and wide range of temperature sensing. These gauges developed were also sought for calibration in different mode of heat transfer like convection, radiation etc. Nanomaterials that could either be used directly or mixed with base materials were also explored for possible efficiency enhancement of the gauges. The characterizations of these materials or films were also a part. Finally, a relation between the thermal and electrical properties of the gauges was also a well sought target of this thesis. All of the objectives were fulfilled during the Ph. D. timeline. All the experimental results were validated through numerical simulation with reasonable accuracy.

Some of the important conclusions that could be drawn from this study are

i. The dimensions of the gauges are well within the assumption of semi-infinite gauges to be used for one-dimensional heat conduction analysis. As discussed in Chapter 3, for a gauge of 6 mm diameter and 10 mm height, semi-infinite assumption is valid for heat load even up to time duration of 1 s.
ii. Cubic spline is a better option compared to least square method as far as analytical deduction of heat flux from temperature signal is concerned. Confirmed through Fig. 3.13 in Chapter 3, the error involved in deducing the input heat load from temperature history through cubic spline is only 13% compared to a significant error of 26% in prediction through least square.
iii. Vacuum coating is established as a sophisticated and more reliable method of thin film deposition over hand painting and spin coating, for its ability to give uniform film and control film thickness. Moreover, it eliminates the steps of polishing and baking, which are ingrained tasks in hand-painting methods.
iv. Addition of CNTs to silver lowers down the initial resistance of the gauges due to enhanced conductivity (both electrical and thermal). This fact is reaffirmed in the

dynamic calibration through laser in Chapter 5, where a lesser peak in output voltage is indicated for application of same heat to the NCTFG compared to STFG.

v. In the study of resistivity vs. film thickness in Chapter 4, thinner films show variable resistivity unless the critical value (film size is twice the mean free path of electron in the material) is achieved. After that bulk limit, values of resistivity does not change significantly with change in film thickness. Thinner films also seem to have higher TCR (inconsistent) values but they have the tendency of getting oxidized in open atmosphere and thus lose resistance earlier. Also, silver films are more stable than copper films.

vi. The TFGs fabricated in lab are able to be used for practical purposes as confirmed by their dynamic calibration in convective and radiation environments in Chapter 5. They respond quickly and accurately in both convection (hot-air gun experiment) and radiation (laser experiment) environment.

vii. Soft computing technique is an apt alternative of deducing heat flux from temperature signal, compared to the tedious analytical methods. Method based on AI can be used for modeling temperature-heat flux relations by "learn and predict" method. From the analysis carried out in Chapter 6, for the concerned gauges, ANFIS based model performs better than ANN in estimating heat flux. The least and highest error involved in ANFIS model for STFG, GTFG and NCTFG come out to be around 1% and 13% respectively. The results also helped in successful establishment of relation between thermo-electrical properties of gauges with the aid of surface plots (Fig. 6.8).

viii. CNTs with lower I_D/I_G ratios are more sensitive towards temperature sensing i.e. more aligned (defect less) CNTs are better temperature sensors. As evident from Table 7.2 in Chapter 7, the I_D/I_G ratio is only 0.42 in case of CNT/DLC:Ni compared to a ratio of 1.89 for CNT/Ni, whereas both are single layer CNT structure. The idea of superior quality with decreasing ratio is later reinforced by the Raman spectra and film sensitivity of the samples calculated through Raman spectroscopy and Van der Paw measurements.

ix. Total resistance increases and film mobility decreases with more number of CNT layers in a multilayer CNT/Ni structure. Table 7.3 in Chapter 7 shows how increase in film thickness and addition of more CNTs can lead to additional scattering of electrons, further increasing overall resistance of the films and decreasing their mobility.

8.2 Future Work

The use of TFGs for measuring the surface heat flux has many limitations, like any other sensors. With prolonged use in high speed flow situations, the film can get easily worn out after a few shots making the gauges lose the adequate resistance, especially in case of hand-painted gauges. Besides, these are passive sensors that require a constant current to energize the system. When performing the measurements at stagnation point of a body, there are experimental difficulties in mounting them exactly at the stagnation point because of the finite area of the sensing film. After exhaustive studies on TFGs, it is seen that there are still ample room for improvement. A few recommendations are listed in the subsequent paragraphs.

Application of the gauges in real-time environments like gas turbine, to check their real-time efficiency in capturing temperature signals, can be a good start to begin with. The multilayer study of the Ni/CNT could be extended to obtain the optimum number of CNT layers that would result in the best possible nanocomposite sensor. Also the film could be replaced with carbon nanofibres instead of nanotubes, and the transition from nanotubes to nanofibres could be studied to highlight the implications that may arise during the study. A third idea could be to repeat the graphene growth to obtain a film instead of solo domains and compare the electrical and thermal characteristics with the CNTs.

Certain drawbacks in the experiments conducted could be sorted out. For e.g. the thermal product of each gauge can be calculated individually instead of taking manufacturer's specifications of substrate materials, since heat flux calculation requires accurate thermal product value of each gauge (Section 3.4, Chapter 3, Eq. 3.5). Sputtering technique could be adopted instead of vacuum coating or aligned growth of CNTs in the film could be attempted. While doing the dynamic calibration through hot air gun method, shutter opening could be automated and losses incurred during the experiments could be quantified.

References

Addison JFD, Wermter S, McGarry KJ, MacIntyre J (2002) Methods for integrating memory into neural networks in condition monitoring. Proc. International Conference on Artificial Intelligence and Soft Computing, Banff, Alberta, Canada.

Alasha'ary H, Moghtaderi B, Page A, Sugo H (2009). A neuro-fuzzy model for prediction of the indoor temperature in typical Australian residential buildings. Energy Buildings 41(7): 703–710. doi: 10.1016/j.enbuild.2009.02.002.

Aryasomayajula L, Wolter KJ (2013) Carbon nanotube composites for electronic packaging applications: a review. Journal of Nanotechnology. http://dx.doi.org/10.1155/2013/296517.

Avner SH (1997) Introduction to Physical Metallurgy, Tata McGraw-Hill Edition, Delhi, India.

Azari A, Poursina M, Poursina D (2014) Radial forging force prediction through MR, ANN, and ANFIS models. Neural Computing & Application 25: 849–858. doi: 10.1007/s00521-014-1562-8.

Balandin AA, Ghosh S, Bao W, Calizo I, Teweldebrhan D, Miao F and Lau CN (2008), Superior thermal conductivity of single-layer graphene, Nano Letters, 8(3): 902-907.

Barnat EV, Nagakura D, Wang PI, Lu TM (2002), Real time resistivity measurements during sputter deposition of ultrathin copper films, Journal of Applied Physics, 91(3): 1667-1672.

Bianchi CL, Cattania MG, Villa P (1993) XPS characterization of Ni and Mo oxides before and after insitu treatments. Applied Surface Science 70 (1): 211-216.

Blackwell BF (1981) Efficient technique for the numerical solution of the one-dimensional inverse problem of heat conduction. Numerical Heat Transfer, Part B: Fundamentals 4(2): 229-238. doi: 10.1080/10407798108547046.

Bokobza L, Zhang J (2012) Raman spectroscopic characterization of multiwall carbon nanotubes and of composites. eXPRESS Polymer Letters 6(7): 601–608. doi: 10.3144/expresspolymlett.2012.63.

Brent F, James MH (2008) Transmission Eletron Microscopy and Diffraction of Materials, Springer, New York.

Brzhezinskaya M, Vinogradov A (2010) Electronic structure of fluorinated carbon nanotubes. Carbon Nanotubes. Jose Mauricio Marulanda (Ed.). doi: 10.5772/39419. Available from: *http://www.intechopen.com/books/carbon-nanotubes/electronic-structure-of-fluorinated-carbon-nanotubes*

Buse A and Lim L (1977), Cubic splines as a special case of restricted least squares, Journal of the American Statistical Association, 72(357): 64-68.

Camacho JM, Oliva AI (2005), Morphology and electrical resistivity of metallic nanostructures, Microelectronics Journal, 36: 555–558.

Cao Y, Nyborg L, Jelvestam U (2009) XPS calibration study of thin-film nickel silicides. Surface and Interface Analysis 41: 471-483. doi: 10.1002/sia3050.

Carpenter CR, Shipway PH, Zhu Y (2011) Electrodeposition of nickel-carbon nanotube nanocomposite coatings for enhanced wear resistance. Wear, 271: 2100–2105.

Çaydas U, Hasçalık A, Ekici S (2009) An adaptive neuro-fuzzy inference system (ANFIS) model for wire-EDM. Expert Systems with Applications 36: 6135–6139. doi:10.1016/j.eswa.2008.07.019.

Chana KS, Jones TV, Wilson TS, Bryanston-Cross P and Burnett MM (2001), High bandwidth heat transfer measurements in an internal combustion engine under low load and motored conditions, Heat Transfer and Cooling in Propulsion and Power Systems, Norway 7 – 11 May.

Chantasiriwan S (2000), Inverse determination of steady-state heat transfer coefficient, International Communications in Heat and Mass Transfer, 27(8): 1155-1164.

Chhowalla M, Teo KBK, Ducati C, Rupesinghe NL, Amaratunga GAJ, Ferrari AC, Roy D, Robertson J, Milne WI (2001) Growth process conditions of vertically aligned carbon nanotubes using plasma enhanced chemical vapor deposition. Journal of Applied Physics 90(10): 5308-5317.

Chu PK, Li L (2006) Characterization of amorphous and nanocrystalline carbon films. Materials Chemistry and Physics 96: 253-277. doi:10.1016/j.matchemphys.2005.07.048.

Cook WJ and Felderman EJ (1966), Reduction of data from thin-film heat-transfer gages: a concise numerical technique. American Institute of Aeronautics and Astronautics Journal 4: 561-562. doi: 10.2514/3.3486.

Das MK, Kishor, N (2009) Adaptive fuzzy model identification to predict the heat transfer coefficient in pool boiling of distilled water. Expert System with Applications 36: 1142–1154. doi: 10.1016/j.eswa.2007.10.044.

Dau VT, Yamada T, Dao DV, Tung BT, Hata K and Sugiyama S (2010), Integrated CNTs thin film for MEMS mechanical sensors, Microelectronics Journal, 41: 860–864.

Dayal D, Rudolf P and Wibmann P (1981), Thickness dependence of the electrical resistivity of epitaxially grown silver films, Thin Solid Films, 79: 193-199.

Denai MA, Palis F, Zeghbib A (2004, October) ANFIS based modelling and control of non-linear systems: a tutorial. IEEE International Conference on Systems, Man and Cybernetics, The Hague, Netherlands.

Diasio M (2011) Electrodeposition behavior and characteristics of Ni-carbon nanotube composite coatings, NNIN Research Accomplishments: 190-191.

Diaz G, Sen M, Yang KT, McClain RL (2001) Dynamic prediction and control of heat exchangers using artificial neural networks. International Journal of Heat and Mass Transfer 44: 1671-1679.

Dickinson T, Povey AF, Sherwood PMA (1977) Dissolution and passivation of nickel-an X-ray photoelectron spectroscopy study. Journal of Chemical Society, Faraday Transactions I 73: 327- 343.

Doebelin EO (1990), 4th Ed. Measurement systems application and design. McGraw-Hill Publishing Company, Singapore.

Doorly JE and Oldfiled MLG (1987), The theory of advanced multi-layer thin film heat transfer gauges, International Journal of Heat and Mass Transfer, 30(6):1159-1168.

Dresselhaus MS, Dresselhaus G, Saito R, Jorio A (2005) Raman spectroscopy of carbon nanotubes. Physics Reports 409: 47-99. doi: 10.1016/j.physrep.2004.10.006.

Du C, Ning PT (2005) CVD growth of carbon nanotubes directly on nickel substrate. Materials Letters 59: 1678–1682.

Dube CE, Workie B, Kounaves SP, Robbat A, Aksu ML, Davies G (1995) Electrodeposition of metal alloy and mixed-oxide films using a single-precursor tetranuclear copper-nickel complex. Journal of Electrochemical Society 142: 3357–3365.

Ducati C, Alexandrou I, Chhowalla M, Amaratunga GAJ, Robertson J (2002) Temperature selective growth of carbon nanotubes by chemical vapor deposition. Journal of Applied Physics 92: 3299. doi: 10.1063/1.1499746.

Durkan C and Welland ME (2000), Size effects in the electrical resistivity of polycrystalline nanowires, Physical Review B, 61(20): 14215-14218.

Ekici BB, Aksoy UT (2011) Prediction of building energy needs in early stage of design by using ANFIS. Expert Systems with Applications 38: 5352–5358. doi: 10.1016/j.eswa.2010.10.021.

Emmanouilidis C, MacIntyre J, Cox C (1998) Neurofuzzy computing aided machine fault diagnosis. Proc. of JCIS'98, The Fourth Joint Conference on Information Sciences. Research Triangle Park, North Carolina, USA.

Esen H, Inalli M (2010) ANN and ANFIS models for performance evaluation of a vertical ground source heat pump system. Expert Systems with Applications 37: 8134–8147. doi: 10.1016/j.eswa.2010.05.074.

Ewing JA (2006), Development of a Direct-Measurement Thin-Film Heat Flux Array.

Ferrari AC (2007) Raman spectroscopy of graphene and graphite: Disorder, electron–phonon coupling, doping and nonadiabatic effects, Solid State Communications 143: 47–57. doi:10.1016/j.ssc.2007.03.052.

Ferrari AC, Basko DM (2013) Raman spectroscopy as a versatile tool for studying the properties of graphene. Nature Nanotechnology 8: 235-246. doi: 10.1038/NNANO.2013.46.

Ferrari AC, Meyer JC, Scardaci V, Casiraghi C, Lazzeri M, Mauri F, Piscanec S, Jiang D, Novoselov KS, Roth S, Geim AK (2006) Raman spectrum of graphene and graphene layers. Physical Review Letters 97: 187401. doi: 10.1103/PhysRevLett.97.187401.

Frankel JI and Keyhani M (2013), Theoretical development of a new surface heat flux calibration method for thin-film resistive temperature gauges and co-axial thermocouples, Shock Waves, 23: 177–188.

Fu L, Yu AM (2014) Carbon nanotubes based thin films: fabrication, characterization and applications. Reviews on Advanced Materials Science 36: 40-61.

Fuchs K and Wills HH (1938), The conductivity of thin metallic films according to the electron theory of metals, Cambridge Philosophical Society, 34: 100-108.

Gan Y, Lee D, Chen X, Kysar JW (2005) Structure and properties of electrocodeposited cu – al_2o_3 nanocomposite thin films. Journal of Engineering Materials and Technology 127: 451-456.

Gardarein JL, Battaglia JL, and Löhle S (2009), Heat flux sensor calibration using noninteger system identification: theory, experiment, and error analysis, Review of Scientific Instruments, 80(025103): 2-8.

George WK, Rae WJ and Woodward SH (1991), An evaluation of analog and numerical techniques for unsteady heat transfer measurement with thin-film gauges in transient facilities, Experimental Thermal and Fluid Science , 4: 333-342.

Ghadimi A, Saidur R, Metselaar HSC (2011) A review of nanofluid stability properties and characterization in stationary conditions. International Journal of Heat and Mass Transfer 54: 4051-4068. doi:10.1016/j.ijheatmasstransfer.2011.04.014.

Ghatak A (2009) Optics, Tata McGraw-Hill, New Delhi, India.

Guo C, Zuo Y, Zhao X, Zhao J, Xiong J (2008) Effects of surfactants on electrodeposition of nickel-carbon nanotubes composite coatings, Surface & Coatings Technology 202: 3385 – 3390.

Holman JP (1986) Heat transfer. McGraw-Hill Book Company, Singapore.

Hone J (2004) Carbon nanotubes: thermal properties. Dekker Encyclopedia of Nanoscience and Nanotechnology 603-610. doi: 10.1081/E-ENN 120009128.

Hone J, Llaguno MC, Biercuk MJ, Johnson AT, Batlogg B, Benes Z, Fischer JE (2002) Thermal properties of carbon nanotubes and nanotube-based materials. Applied Physics A 74(3): 339-343.

Hossain ME, Hossain MK, Hosur MV, Jeelani S (2015) Effect of dispersion conditions on the thermal and mechanical properties of carbon nanofiber–polyester nanocomposites. Journal of Engineering Materials and Technology 137(5): 1-9. doi: 10.1115/1.4030196.

Hwang YJ, Ahn YC, Shin HS, Lee CG, Kim GT, Park HS, Lee JK (2006) Investigation on characteristics of thermal conductivity enhancement of nanofluids. Current Applied Physics 6(6): 1068–1071.

Iijima S (1991) Helical microtubules of graphitic carbon. Nature 354: 56-58. doi:10.1038/354056a0

Jan T (1996) Theory of transient experimental techniques for surface heat transfer. International Journal of Heat and Mass Transfer 39(17): 3733-3748.

Jang JSR (1993) ANFIS: Adaptive-network-based fuzzy inference system. IEEE Transactions on Systems Man and Cybernetics 23(3): 665–685.

Jang JSR, Gulley N (1996) Fuzzy logic toolbox: Reference manual. The Mathworks Inc.

Jen SU, Yu CC, Liu CH and Lee GY (2003), Piezoresistance and electrical resistivity of Pd, Au, and Cu films, Thin Solid Films, 434: 316-322.

Jessen C and Groenig H (1991), A new method for manufacture of thin film heat flux gauges, Shock Waves, 1: 161-164.

Kakac C, Pramuanjaroenkij A (2009) Review of convective heat transfer enhancement with nanofluids. International Journal of Heat and Mass Transfer 52: 3187–3196. doi:10.1016/j.ijheatmasstransfer.2009.02.006.

Kant R, Joshi SN (2013) Finite element simulation of laser assisted bending with moving mechanical load. International Journal of Mechatronics and Manufacturing Systems 6(4): 351-366. doi: 10.1504/IJMMS.2013.057128.

Kawamura M, Mashima T, Abe Y and Sasaki K (2000), Formation of ultra-thin continuous Pt and Al films by RF sputtering, Thin Solid Films, 377: 537-542.

Kim KS, Winograd N (1974) X-ray photoelectron spectroscopic studies of nickel-oxygen surfaces using oxygen and argon ion-bombardment. Surface Science 43: 625-643.

Kim SK, Oh TS (2011) Electrodeposition behavior and characteristics of Ni-carbon nanotube composite coatings. Transactions of Nonferrous Metals Society of China 21: s68-s72.

Kinnear KM, Lu FK (1999) Characterization of thin-film heat-flux gauges. Journal of Thermophysics and Heat Transfer 13(4): 548-549. doi: 10.2514/2.6477.

Kishor N, Das MK (2010) Soft computing techniques for prediction of boiling heat transfer coefficient of liquids on copper-coated tubes. Applied Artificial Intelligence: An International Journal 24(3): 210-232. doi: 10.1080/08839510903549614.

Klar P, Lidorikis E, Eckmann A, Verzhbitskiy IA, Ferrari AC, Casiraghi C (2013) Raman scattering efficiency of graphene. Physical Review B 87: 205435. doi: 10.1103/PhysRevB.87.205435.

Kline SJ, McClintock FA (1953) Describing uncertainties in single sample experiments. Mechanical Engineering 75: 3–8.

Kong J, Cassell AM, Dai H (1998) Chemical vapor deposition of methane for single-walled carbon nanotubes, Chemical Physics Letters, 292: 567–574.

Kong J, Hyongsok TS, Cassell AM, Quate CF, Dai H (1998) Synthesis of individual single-walled carbon nanotubes on patterned silicon wafers, Nature, 395(6705): 878 - 881 http://dx.doi.org/10.1038/27632.

Kovács GJ, Bertóti I, Radnóczi G (2008) X-ray photoelectron spectroscopic study of magnetron sputtered carbon–nickel composite films. Thin Solid Films 516: 7942–7946.

Kumar R, Jayesh P, Sahoo N (2012) Analysis of one dimensional inverse heat conduction problem: a review. International Journal of Mechanical & Industrial Engineering 2(1): 2231-2239.

Kumar R, Sahoo N (2011) Enhancement of thermal properties for platinum thin film heat transfer gauges with nanofluids. In: Proceedings of 28th international symposium on shock waves, July 17–22, The University of Manchester, UK, ISSW28, p 2179.

Kumar R, Sahoo N, Kulkarni V (2012) Conduction based calibration of handmade platinum thin film heat transfer gauges for transient measurements. International Journal of Heat and Mass Transfer 55(9): 2707-2713. doi:10.1016/j.ijheatmasstransfer.2012.01.026.

Kumar R, Sahoo N, Kulkarni V, Singh A (2011) Laser based calibration technique for thin film sensors for short duration transient measurements. ASME Journal of Thermal Science and Engineering Applications 3(4): 0445041-0445046. doi:10.1115/1.4005075.

Kundu S, Hazra S, Banerjee S, Sanyal MK, Mandal SK, Chaudhuri S and Pal AK (1998), morphology of thin silver film grown by dc sputtering on Si (001), Journal of Physics D: Applied Physics, 31: 73–77.

Lacy F (2007), Investigating thin films for use as temperature sensors, Proceedings of the World Congress on Engineering & Computer Science: October 24-26, San Francisco: 441-444.

Lacy F (2009), Using nanometer platinum films as temperature sensors (constraints from experimental, mathematical, and finite-element analysis), IEEE Sensors Journal, 9(9): 1111-1117.

Lacy F (2011-a), Developing a theoretical relationship between electrical resistivity, temperature, and film thickness for conductors, Nanoscale Research Letters, 6(636): 1-14.

Lacy F (2011-b), Evaluating the resistivity-temperature relationship for RTDs and other conductors, IEEE Sensors Journal, 11(5): 1208-1213.

Lee CK (2012) Wear and corrosion behavior of electrodeposited nickel– carbon nanotube composite coatings on Ti–6Al –4V alloy in Hanks 0 solution, Tribology International 55: 7–14.

Lei JF, Martin LC and Will HA, Advances in thin film sensor technologies for engine applications, NASA Technical Memorandum 107418.

Li CP, Proctor A, Hercules DM (1984) Curve fitting analysis of ESCA Ni 2p spectra of nickel-oxygen compounds and Ni/Al_2O_3 catalysts. Applied Spectroscopy 38(6): 880-886.

Li QW, Li Y, Zhang XF, Chikkannanavar SB, Zhao YH, Dangelewicz AM, Zheng LX, Doorn SK, Jia QX, Peterson DE, Arendt PN and Zhu YT (2007) Structure-dependent electrical properties of carbon nanotube fibers. Advanced Materials 19: 3358–3363. doi:10.1002/adma.200602966.

Li X, Chen Y, Chen Z, Zhao J (2006) Thermal performances of different types underground heat exchangers. Energy and Buildings 38: 543–547. doi: 10.1016/j.enbuild.2005.09.002.

Liu HD, Zhao YP, Ramanath G, Murarka SP, Wang GC (2001), Thickness dependent electrical resistivity of ultrathin (< 40 nm) cu films, Thin Solid Films, 384: 151-156.

Liu MS, Lin MCC, Huang IT and Wang CC (2005), Enhancement of thermal conductivity with carbon nanotube for nanofluid, Int. Communications in Heat and Mass Transfer, 32: 1202–1210.

Loos MR, Coelho LAF, Pezzin SH, Amico SC (2008) Effect of carbon nanotubes addition on the mechanical and thermal properties of epoxy matrices. Materials Research 11(3): 347-352.

Lubna R, Rajneesh S, Vimal S (2013) Synthesis and structural characterization of Al-CNT metal matrix composite using physical matrix method, IOSR Journal of Applied Physics 5 (4): 54–57.

Lyons PRA and Gai SL (1988), A method for the accurate determination of the thermal product $(\rho ck)^{\frac{1}{2}}$ for thin film heat transfer or surface thermocouple gauges, Journal of Physics E: Scientific Instruments, 21: 445-448.

MacIntyre J (2013) Applications of neural computing in the twenty-first century and 21 years of Neural Computing & Applications. Neural Computing & Applications 23:657–665. doi: 10.1007/s00521-013-1471-2.

Mansour AN (1994) Characterization of NiO by XPS. Surface Science Spectra 3(3): 231-238. doi: 10.1116/1.1247751.

Mansur WJ, Vasconcellos CAB, Zambrozuski NJM, Filho OCR (2009) Numerical solution for the linear transien heat conduction equation using an explicit Green's approach. International Journal of Heat and Mass Transfer 52: 694-701. doi:10.1016/j.ijheatmasstransfer.2008.07.036.

Marchetti L, Miserque F, Perrin S, Pijolat M (2015) XPS study of Ni-base alloys oxide films formed in primary conditions of pressurized water reactor. Surface and Interface Analysis 47 (5): 632-642.

Marcq F, Demont P, Monfraix P, Peigney A, Laurent C, Falat T, Courtade F, Jamin T (2011) Carbon nanotubes and silver flakes filled epoxy resin for new hybrid conductive adhesives. Microelectronics Reliability 51: 1230-1234. doi:10.1016/j.microrel.2011.03.020.

Matienzo LJ, Yin LI, Grim SO, Swartz WE (1973) X-ray photoelectron spectroscopy of nickel compounds. Inorganic Chemistry 12(12): 2762-2769.

Mehta RC, Jayachandran T and Sastri VMK (1988), Finite element analysis of conductive and radiation heating of a thin skin calorimeter, Journal of Heat and Mass Transfer, 22: 227-230.

Mellit A, Kalogirou SA, Hontoria L, Shaari S (2009) Artificial intelligence techniques for sizing photovoltaic systems: A review. Renewable and Sustainable Energy Reviews 13: 406–419. doi: 10.1016/j.rser.2008.01.006.

Mert I, Arat HT (2014) Prediction of heat transfer coefficients by ANN for aluminum & steel material. International Journal of Scientific Knowledge 5(2): 53-63.

Mocikat H and Herwig H (2009), Heat Transfer Measurements with Surface Mounted Foil-Sensors in an Active Mode: A Comprehensive Review and a New Design, Sensors, 9: 3011-3032.

Monte F (2000), Transient heat conduction in one-dimensional composite slab, a 'natural' analytic approach, International Journal of Heat and Mass Transfer, 43: 3607-3619.

Namba Y (1970), Resistivity and temperature coefficient of thin metal films with rough surfaces, Japanese Journal of Applied Physics, 9(11): 1326-1329.

Nayak KC, Tripathy RK, Panda SR, Sahoo SN (2014) Prediction of cutting and feed forces for onventional milling process using adaptive neuro fuzzy inference system (ANFIS). IAES International Journal of Artificial Intelligence 3(1): 24-35. doi: 10.11591/ij-ai.v3i1.2908.

O'Brien JE (1990), A technique for measurement of instantaneous heat transfer in steady-flow ambient-temperature facilities, Experimental Thermal and Fluid Science, 3(4): 416-430.

Otiigen MV, Namer I (1988) Rayleigh scattering temperature measurements in a plane turbulent air jet at moderate Reynolds numbers. Experiments in Fluids 6: 461-466.

Patsalas P, Handrea M, Logothetidis S, Gioti M, Kennou S and Kautek W (2001) A complementary study of bonding and electronic structure of amorphous carbon films by electron spectroscopy and optical techniques. Diamond and Related Materials 10:960-964.

Piccini E , Guo SM and Jones TV (2000), The development of a new direct-heat-flux gauge for heat-transfer facilities, Measurement Science and Technology, 11: 342–349.

Rao AM, Jorio A, Pimenta MA, Dantas MSS, Saito R, Dresselhaus G, Dresselhaus MS (2000) Polarized raman study of aligned multiwalled carbon nanotubes. Physical Review Letters 84(8): 1820-1823.

Rath S, Singh AP, Bhaskar U, Krishna B, Santra BK, Rai D, Neogi N (2015) Artificial neural network modeling for prediction of roll force during plate rolling process. Materials and Manufacturing Processes 25: 149-153. doi: 10.1080/10426910903158249.

Rizal M, Ghani JA, Nuawi MZ, Haron CHC (2013) Online tool wear prediction system in the turning process using an adaptive neuro-fuzzy inference system. Applied Soft Computing 13: 1960–1968. doi: 10.1016/j.asoc.2012.11.043.

Rossnagel SM, Kuan TS and Sai JV (2004), Alterations of Cu conductivity in the size effect regime, Journal of Vacuum Science and Technology B, 22(1): 240-247.

Sahoo N, Peetala RK (2010) Transient temperature data analysis for a supersonic flight test. ASME Journal of Heat Transfer132: 310-315.

Saito T, Menezes V, Kuribayashi T, Sun M, Jagadeesh G and Takayama K (2004), Unsteady convective surface heat flux measurements on cylinder for CFD code validation, Shock Waves, 13: 327–337.

Saravanan S, Jagadeesh G and Reddy KPJ (2009), Convective heat-transfer rate distributions over a missile shaped body flying at hypersonic speeds, Experimental Thermal and Fluid Science, 33: 782–790.

Sazmal EA, William EL, Peter FJ (2011) Commercial silicate glass-ceramics: Characterization by XRD and TEM on crystallization, Borneo Science 29: 10–22.

Scalabrin G, Condosta M, Marchi P (2006). Flow boiling of pure fluids: local heat transfer and flow pattern modeling through artificial neural networks. International Journal of Thermal Sciences 45: 739–751. doi: 10.1016/j.ijthermalsci.2005.09.010.

Schultz DL, Jones TV (1973) Heat transfers measurements in short duration hypersonic facilities AGARDograph-AG-165.

Sinclair IR (1987) Electronics for electricians and engineers. Industrial Press Inc.

Skinner GT (1962) A new method of calibrating thin film gauge backing materials. Cornell Aeronautical Laboratory, Buffalo, New York, CAL – 105.

Smith DE, Bubb JV, Popp O, Diller TE, Hevey SJ (1999) A comparison of radiation versus convection calibration of thin-film heat flux gauges. Proceedings of the ASME Heat Transfer Division, HTD 364: 79-84.

Steen W, Watkins KG, Mazumdaer J (2010) Laser material processing, 4th Ed., Springer Science & Business Media. Springer-Verlag London. doi: 10.1007/978-1-84996-062-5.

Sumant AV, Grierson DS, Gerbi JE, Carlisle JA, Auciello O, Carpick RW (2007) Surface chemistry and bonding configuration of ultrananocrystalline diamond surfaces and their effects on nanotribological properties. Physical Review B 76: 235429. doi: 10.1103/PhysRevB.76.235429.

Sun X, Tao R, Lin L, Li Z, Zhang Z, Feng J (2011) Fabrication and characterization of polycrystalline silicon nanowires with silver-assistance by electroless deposition. Applied Surface Science 257: 3861–3866. doi:10.1016/j.apsusc.2010.11.058.

Sun Y, Sun J, Liu M and Chen Q (2007) Mechanical strength of carbon nanotube–nickel nanocomposites. Nanotechnology, 18(50): 505-704.

Taler J (1996) Theory of transient experimental techniques for surface heat transfer. International Journal of Heat Mass Transfer 39(17): 3733-3748. doi:10.1016/0017-9310(96)00015-4.

Talib ARA, Neely AJ, Mullender AJ and Jaafar AA (2005), Computational study on conduction heat transfer through a thin film gauge, International Journal of Engineering and Technology, 2(1): 1-7.

Thirumaleshwar M (2009) Fundamentals of heat and mass transfer. Pearson Education: India.

Tomar V, Samvedi V (2011) Correlation of thermal conduction properties with mechanical deformation characteristics of a set of SiC–Si_3N_4 nanocomposites. Journal of Engineering Materials and Technology 133(13): 1-7. doi: 10.1115/1.4002646.

Tritt TM (2006) Thermal conductivity: theory, properties, and applications. Springer Science & Business Media. Springer US. doi: 10.1007/b136496.

Unal A (1994) Jerk fields and artificial neural networks in manufacturing. Proceedings of the 1994 Symposium on Intelligent Systems in Communications and Power, 293, University of Puerto Rico.

Unal A, Bush JJ, Vaidya UK, Crocker M (1991) Acoustic emissions as diagnostic tools for complex systems. The Journal of the Acoustical Society of America 90 (4): 2323.

Unal A, Herrmann G (1975) On the effect of bonding in a laminated composite. SUDAM 75(2).

Unal A, Wasserman PD (1990) Vibration signature analysis using artificial neural networks. The Journal of the Acoustical Society of America 88: S20.

Van der Puaw LJ (1958), A method of measuring the specific resistivity and hall effect of discs of arbitrary shape, Philips Research Reports 13(1): pp.1-9.

Venezia AM, Bertoncello R, Deganello G (1995) X-ray photoelectron-spectroscopy investigation of pumice-supported nickel-catalysts. Surface Interface Analysis 23(4): 239-247.

Vinod KG, Tawfik AS (2011) Synthesis of carbon nanotube-metal oxides composites; adsorption and photo-degradation, Carbon Nanotubes - From Research to Applications 295–312. doi:10.5772/18009.

Waduge P, Larkin J, Upmanyu M, Kar S, Wanunu M (2015) Programmed synthesis of freestanding graphene nano-membrane arrays, Small 11(5): 597-609.doi: 10.1002/smll.201402230.

Walker DG and Scottt EP (1998), Evaluation of estimation methods for high unsteady heat fluxes from surface measurements, Journal of Thermophysics and Heat Transfer, 12(4): 543-551.

Wang B, Gallais L (2013) A theoretical investigation of the laser damage threshold of metal multi-dielectric mirrors for high power ultrashort applications. Optics Express 21(12): 14698-14711. doi: 10.1364/OE.21.014698.

Wang XQ, Mujumdar AS (2007) Heat transfer characteristics of nanofluids: a review. International Journal of Thermal Sciences, 46:1–19. doi:10.1016/j.ijthermalsci.2006.06.010.

Wang XW, Fei GT, Zheng K, Jin Z and Zhang LD (2006), Size dependent melting behavior of Zn nanowire arrays, Applied Physics Letters , 88(173114).

Wasserman PD, Unal A, Haddad S (1991). Neural networks for on-line machine condition monitoring. Intelligent Engineering Systems Through Artificial Neural Networks 693-699.

Wei M, Bai B, Sung AH, Liu Q, Wang J, Cather ME (2007) Predicting injection profiles using ANFIS. Information Sciences 177: 4445–4461. doi: 10.1016/j.ins.2007.03.021.

Wiegand DA, Owens FJ, Goyal A and Iqbal Z (2008) Fabrication of high strength metal-carbon nanotube composites, US Army Research, Development and Engineering Center, Picatinny, New Jersey 07806.

Xuan Y and Li Q (1999), Heat transfer enhancement of nano fluids, International Journal of Heat and Fluid Flow, 21: 58-64.

You SM, Kim JH and Kim KH (2003), Effect of nanoparticles on critical heat flux of water in pool boiling heat transfer, Applied Physics Letters, 83(16): 3374-3376.

Zanganeh N, Rajabi A, Torabi M, Allahkarami M, Moghaddas A, Sadrnezhaad SK (2014) Growth and microstructural investigation of multiwall carbon nanotubes fabricated using electrodeposited nickel nanodeposits and chemical vapor deposition method. Journal of Molecular Structure 1074 : 250–254.

Zhang S, Li L, Kumar A (2009) Materials Characterization Techniques, Taylor & Francis.

Zhang W, Brongersma SH, Richard O, Brijs B, Palmans R, Froyen L and Maex K (2004), Influence of the electron mean free path on the resistivity of thin metal films, Microelectronic Engineering, 76: 146–152.

Zhong B, MacIntyre J, He Y, Tait J (1998) High Order Neural Networks for Simultaneous Diagnosis of Multiple Faults in Rotating Machines. Neural Computing& Applications 8:189–195.

Zhu F, Wu Y (2014) A rapid structural damage detection method using integrated ANFIS and interval modeling technique. Applied Soft Computing 25: 473–484. http://dx.doi.org/10.1016/j.asoc.2014.08.043.

APPENDIX A

Experiments with graphene

Graphene, another allotrope of carbon is also attempted to adjudge if it's a better choice than the CNTs. However since the graphene formed in separate domains instead of a continuous film, the electrical measurements had no point although its formation, structure and number of layers could be successfully obtained through various analysis. In addition, we investigate the smooth growth of graphene on electroplated Cu film and not on Cu foil (most common) on Si without any prior smoothing or polishing process

A.1 Substrate preparation

In case of graphene however Cu is used as the catalyst. A thin layer of Cu is electroplated on a SiO_2/Si substrate. The Si substrate has a native oxide layer of around 10 nm. No seed layer is sputtered for deposition of Cu on Si in this study. The electrodeposition is done in a plating bath with the following additives in the aqueous solution: ammonium fluoride (NH_4F 40%) 50 vol.%, copper sulfate ($CuSO_4 \cdot 5H_2O$) 0.01 M, ascorbic acid ($C_6H_8O_6$) 0.01 M, sodium potassium tartrate ($KNaC_4H_4O_6 \cdot 4H_2O$) 0.005 M, and methanol 30 vol.% (percentages are referred to the final solution volume). Initially the substrates are cleaned in acetone in an ultrasonic bath for 10 min, followed by cleansing in iso-propanol for next 10 min. Then the substrates are tickled in 1M HF solution for 10 min to remove the native oxide layer. The anode is made up of a pure copper wire, dipped into the solution. Keeping the solution stirred continuously on a magnetic stirrer, the substrates are dipped in the solution that serves as the cathode. A constant voltage of 10 V DC is applied and the current density is kept around ~4A/dm^2. Different time of deposition are carried out for e.g. for 2, 3, 5, 7 and 10 min etc. The water on the electroplated substrates is quickly dried using a hand-pump and inserted in to the CVD chamber (vacuum) to avoid oxidation of copper films and for further annealing.

A.2 Synthesis of graphene

The procedure is almost similar with the above except that for graphene growth the optimum C_2H_2: Ar ratio is found to be 15:100 and the time of growth is kept at 6 min. The system is evacuated down to a base pressure of 5.6×10^{-3} mbar for deposition. Three different growth

temperatures are tried viz. 750℃, 850℃ and 950℃. The samples are unloaded when the temperature is well below 80℃.

A.3 Characterization

Two types of characterization are done with the graphene samples: SEM for surface morphology study, Raman spectroscopy for confirmation of graphene formation and number of layers and optical reflectivity to check the reflectivity of the Cu substrates.

A.3.1 SEM study

Fig. A.1 shows the low magnification SEM photograph of graphene domains grown on electroplated Cu surface (2, 7 and 10 min deposition) at 950˚C. The graphene domains are randomly formed on the electroplated Cu, the electroplated Cu either consisting of single or coalesced grains. The graphene domain sized in the range of 150 nm to 700 nm.

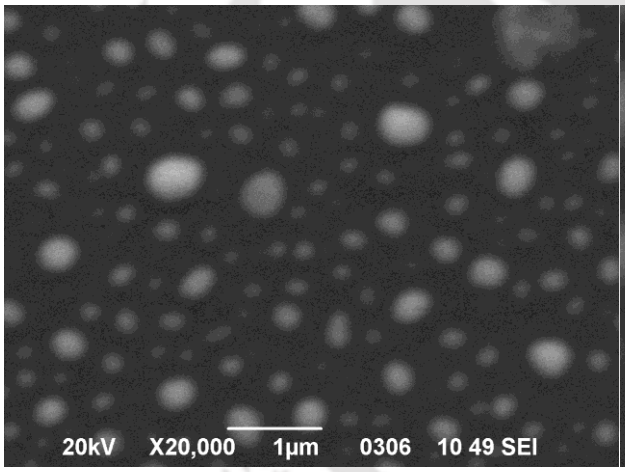

(a) 20 kX

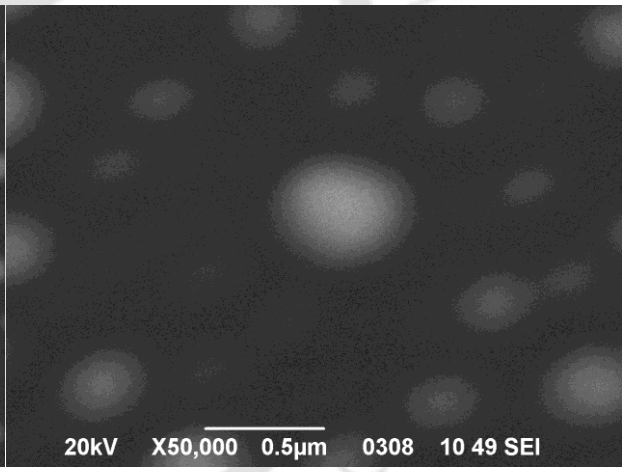

(b) 50 kX

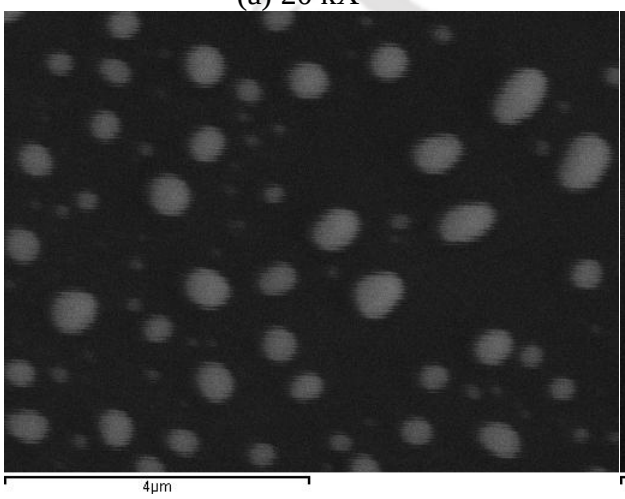

(c) 14 kX

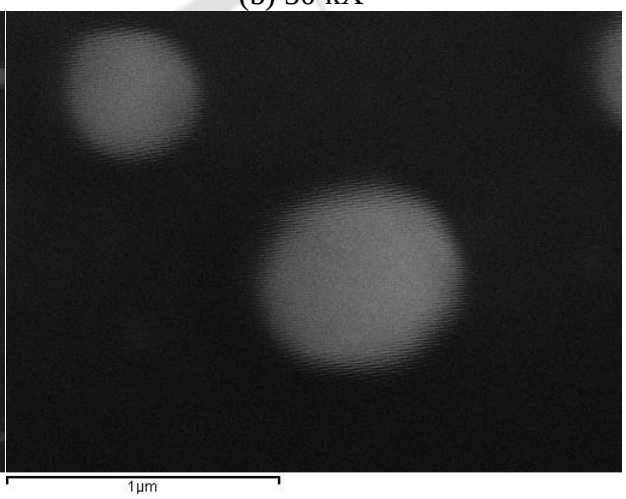

(d) 50 kX

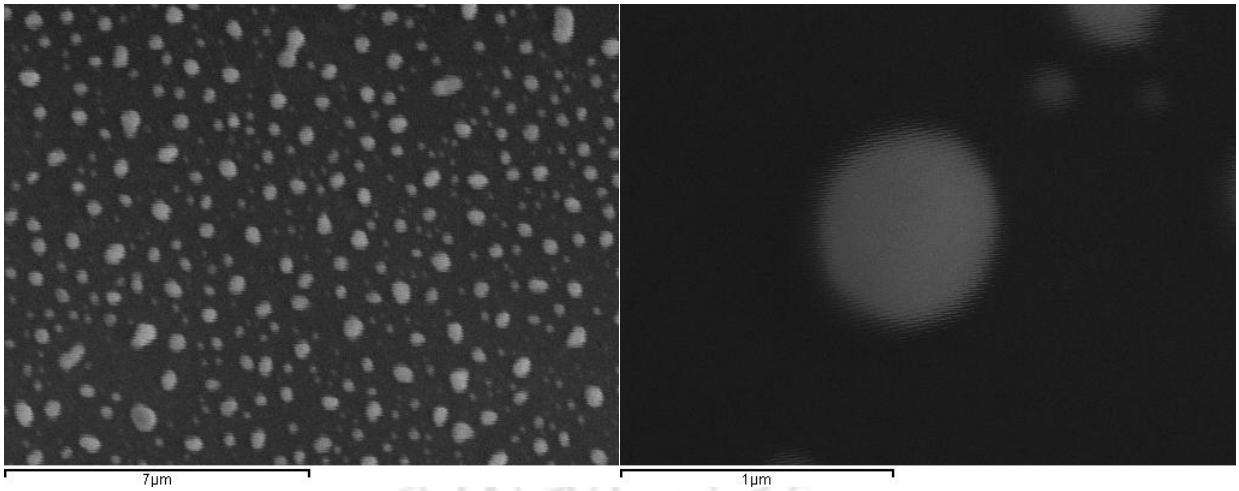

(e) 8 kX (f) 50 kX

Fig. A.1 SEM photographs of graphene domains grown on electrodeposited Cu on Si with different magnifications for (a/b) 10 min (c/d) 7 min and (e/f) 2 min, all grown at 950˚C

A.3.2 Raman study

The Raman spectrum of graphene carries distinctive features, each peak being characterized by its position, height and area. The two most significant feature in graphene spectra is the G band at ~1580 cm^{-1} and 2D band at ~2700 cm^{-1}[20]. The measured peaks are fit with Lorentzians. Several measurements are performed on both the same spot and different spots on the same sample. Fig. A.2 presents Raman spectra of graphene samples grown on electroplated Cu (different electrodeposition times) prepared at 850℃ and 950℃ for 6 min by LPCVD with 15 sccm C_2H_2 flow. Fig. A.2(a) to Fig. A.2(c) shows the spectra of samples grown at 950℃ on Cu/Si substrates with electrodeposition times of 2, 7 and 10 min respectively. Whereas Fig. A.2(d) to Fig. A.2(g) show the spectra of samples grown at 850℃ on Cu/Si substrates with electrodeposition times of 3, 5, 7 and 10 min, respectively. Fig. A.3 shows a detail analysis of 2D peak for the same samples as shown in Fig. A.2.

The position of D bands that suggests defects in the graphene layers is found to vary in the range of 1352 cm^{-1} to 1363 cm^{-1}. The G band, which proves the hexagonal lattice formation of the carbon are found at around 1588 $cm^{-1}$to 1600 cm^{-1}. The 2D band is a double resonance of D band and helps to determine the number of graphene layers and the quality of graphene through its intensity and shape. The position of 2D peaks in the present case range from 2693 cm^{-1} to 2709 cm^{-1}. The position of the bands, with the corresponding FWHM and I_{2D}/I_G ratios are listed in Table A.1.

The D bands are smaller in case of the graphene grown at 950℃ compared to those grown at 850℃. Very low D bands in Raman spectra are typical of high quality graphene structures implying that samples of 950℃, are of superior quality. The G and 2D peaks are found to shift upward in frequency with increasing number of layers. It is reported that generally accepted ratio for I_{2D}/I_G ratio for bilayer graphene is assumed between 0.8 and 1.4, whereas a ratio greater than 1.4 represents monolayer graphene. Few-layer graphene or graphene with more than three layers are generally identified with an I_{2D}/I_G ratio < 0.8 [Waduge et al. 2015]. As such, the peak intensity ratio of 0.87 and 1.06 and low FWHM values of 41.3 (G peak) & 62.7 (2D peak) and 34.1 (G peak) & 50.8 (2D peak) in case of G210 and G32, respectively (Table A.1) indicates the presence of bi layer graphene. On the other hand, a ratio of I_{2D}/I_G <0.8 confirms existence of few-layer graphene in rest of the samples. A lower FWHM suggests better homogeneity of thickness of the grown graphene. Table A.1 indicates the position, amplitude, FWHM and I_{2D}/I_G ratios for all the samples.

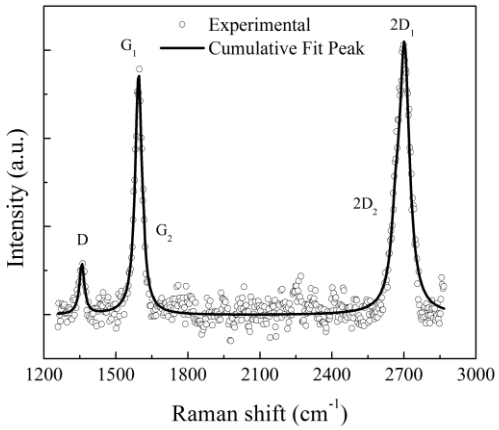

(a)

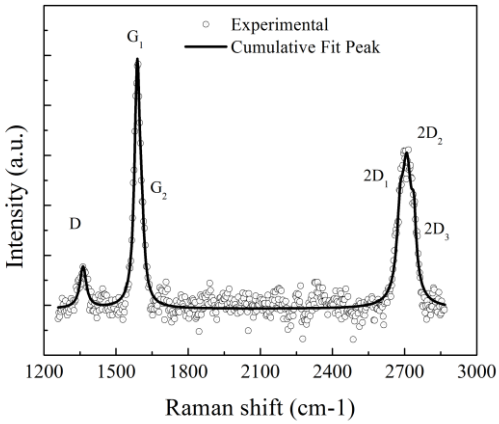

(b)

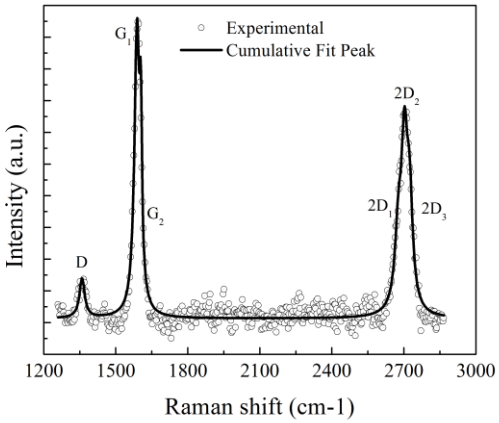

(c)

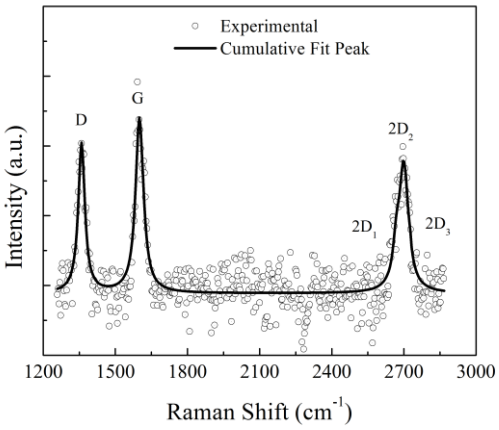

(d)

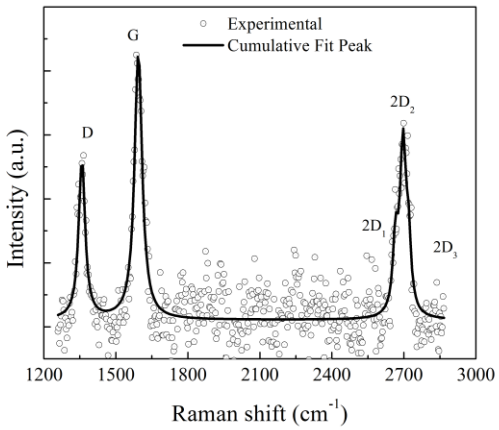

(e)

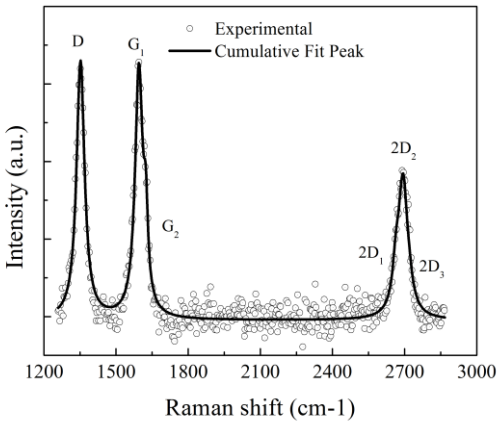

(f)

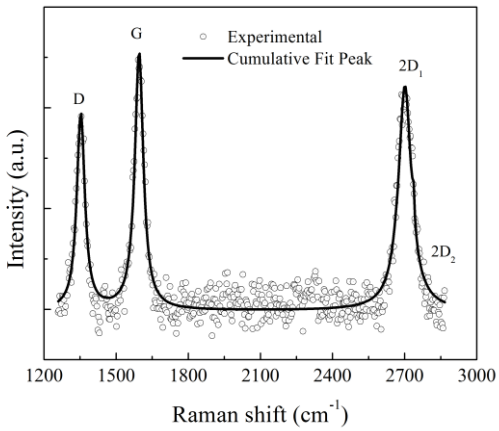

(g)

Fig. A.2 Raman spectra of graphene samples (a) G32 (b) G37 (c) G310 (d) G23 (e) G25 (f) G27 and (g) G210

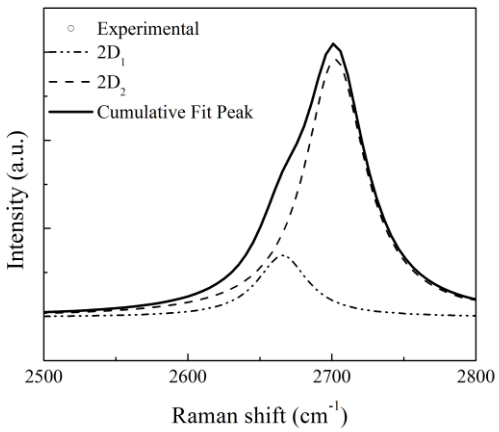

(a)

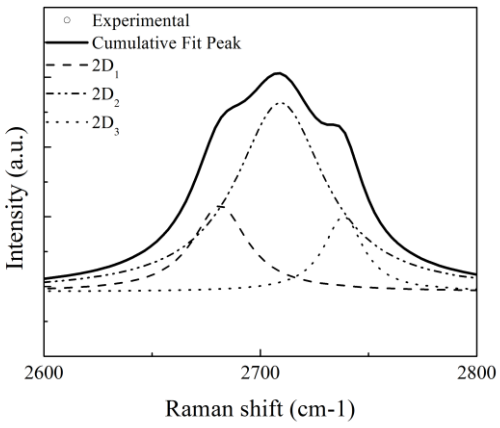

(b)

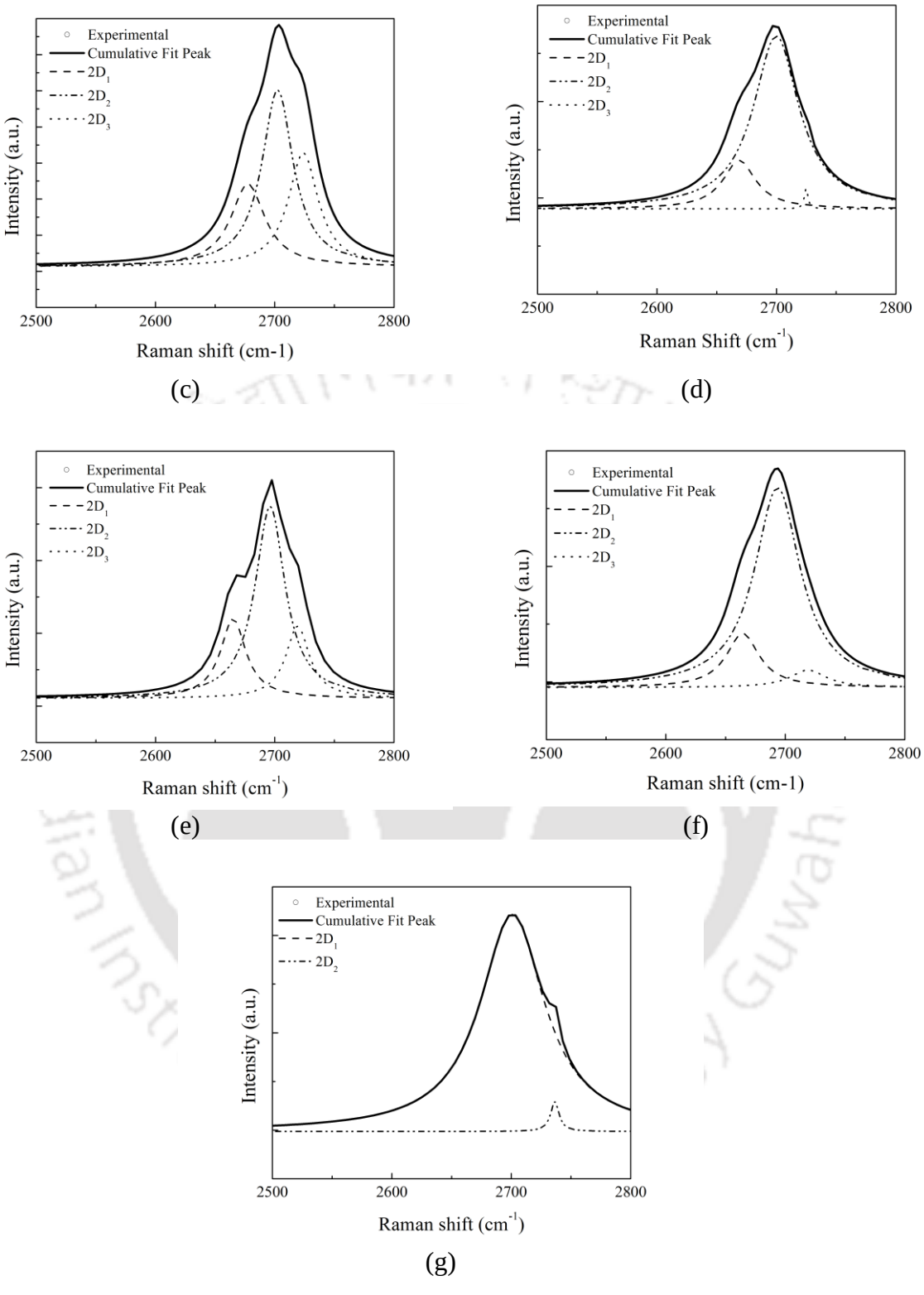

Fig. A.3 2D peak of Raman spectra of graphene samples (a) G32 (b) G37 (c) G310 (d) G23 (e) G25 (f) G27 and (g) G210

Table A.1 Raman analysis for graphene samples

Sample	Electro depo-sition time: Cu/ Si	Temp (˚C)	PosD (cm^{-1})	PosG (cm^{-1})	Pos2D (cm^{-1})	FWHM (G)	FWHM (2D)	I_{2D}/I_G
G23	3 min		1359.33	1595.65	2696.95	29.89	46.41	0.81
G25	5 min	850	1358.89	1589.90	2701.10	29.79	38.04	0.69
G27	7 min		1352.34	1594.97	2693.46	38.29	46.64	0.54
G210	10 min		1352.98	1594.60	2699.46	41.26	62.68	**0.87**
G32	2 min		1358.85	1594.83	2702.29	34.09	50.80	**1.06**
G37	7 min	950	1362.81	1588.07	2709.30	27.20	50.04	0.58
G310	10 min		1359.77	1588.48	2702.38	26.37	31.84	0.54

A.3.3 Optical study

Optical reflectivity spectra of the electrodeposited Cu on Si samples before and after the growth of graphene are shown in Fig. A.4(a) and Fig. A.4(b) respectively. It can be speculated from Fig. A.4(a), higher electrodeposition time leads to thicker films as the reflectivity increases with increase in thickness of the films. The difference is more prominent in IR wavelength than in the visible wavelength range. In Fig. A.4(b) also, the thickness seem to increase with increasing electrodeposition time with only the 2 min deposition sample following unusual trend.

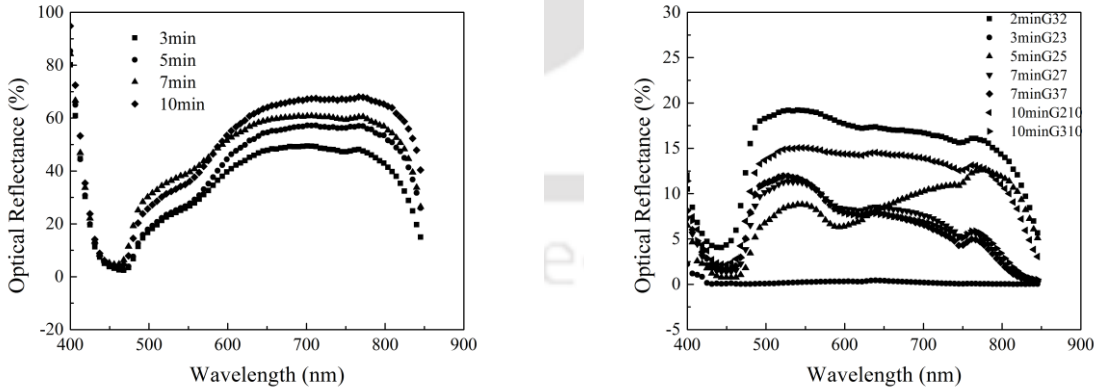

(a) (b)

Fig. A.4 Optical reflectivity spectra of Cu/Si samples

A.4 Conclusion

In case of graphene, since a continuous film is not obtained so electrical measurements have no point. However these graphene domains could be used for selective deposition of graphene quantum dots. The presence of Cu layer beneath the graphene could enhance the photoluminescence of the GQDs grown. Yet, to conclude, growth of few layer and bi layer graphene has been achieved successfully using a simple, low-cost electrodeposition method based on aqueous solutions $CuSO_4$. Domains of graphene are grown using a low-pressure CVD method, the most common method for graphene growth. The Raman spectra show low D bands (the defect related bands) in case of samples grown at 950℃ compared to those grown at 850℃. The line shape of the 2D peak and the FWHM indicates presence of bi and few layer graphene. The G and 2D peaks are shifted upward in frequency with increasing the number of layers and the number of layers is found to increase with increasing thickness of the samples except for the G210 sample.

APPENDIX B

Instruments and laboratory setup used

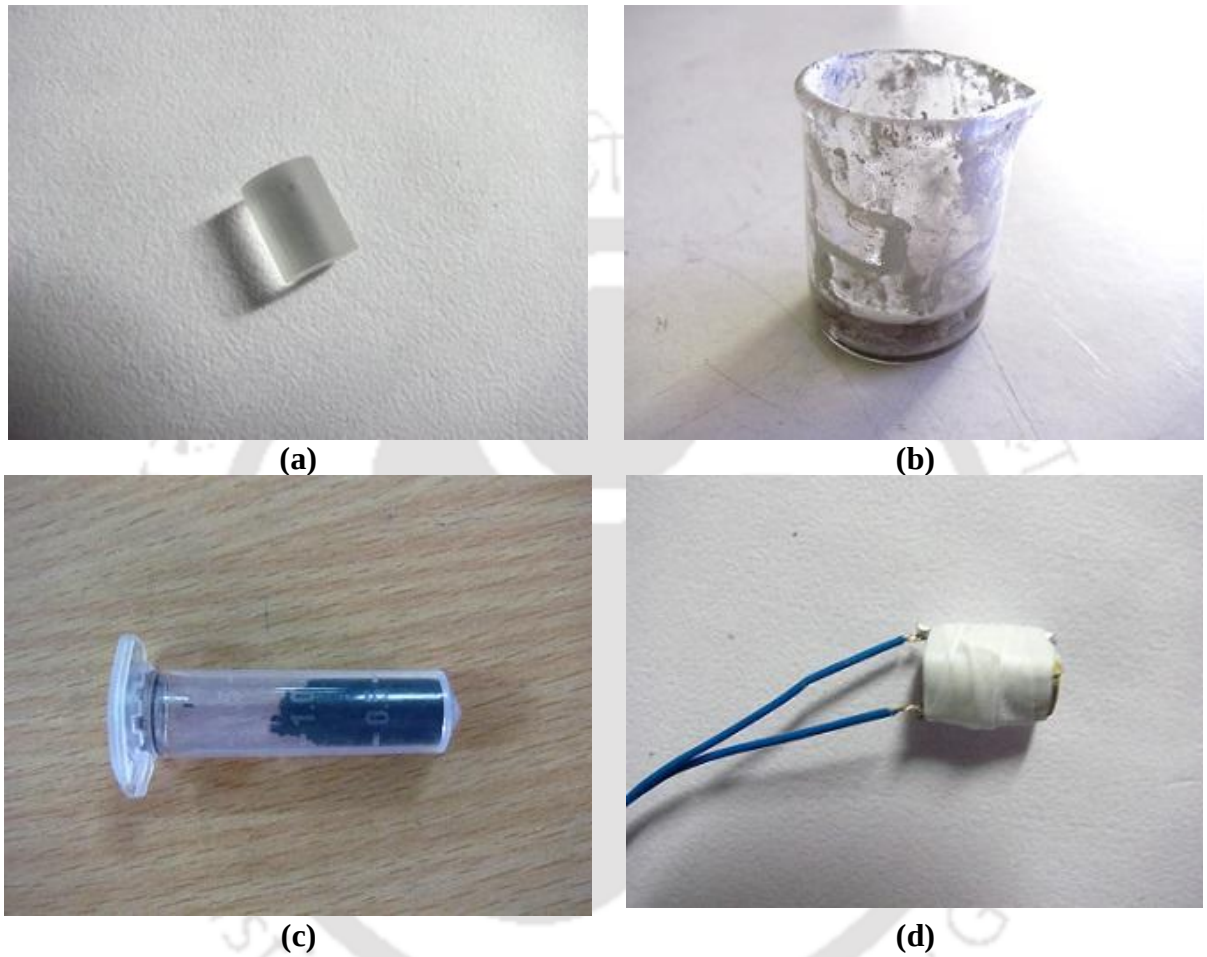

Fig. B.1 (a) Pyrex substrate (b) silver paste used in hand-painting (c) commercial MWCNTs and (d) a typical STFG

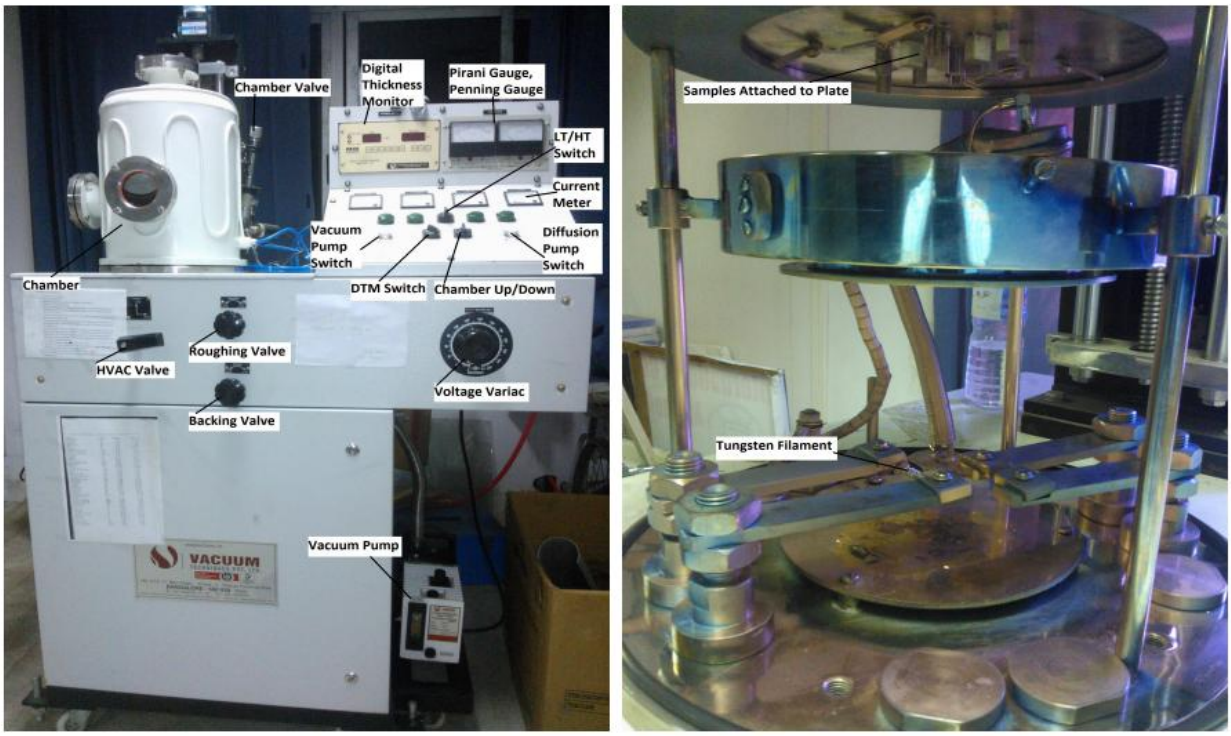

Fig. B.2 Vacuum coating unit

Fig. B.3 Four point technique setup for thickness vs. resistivity study

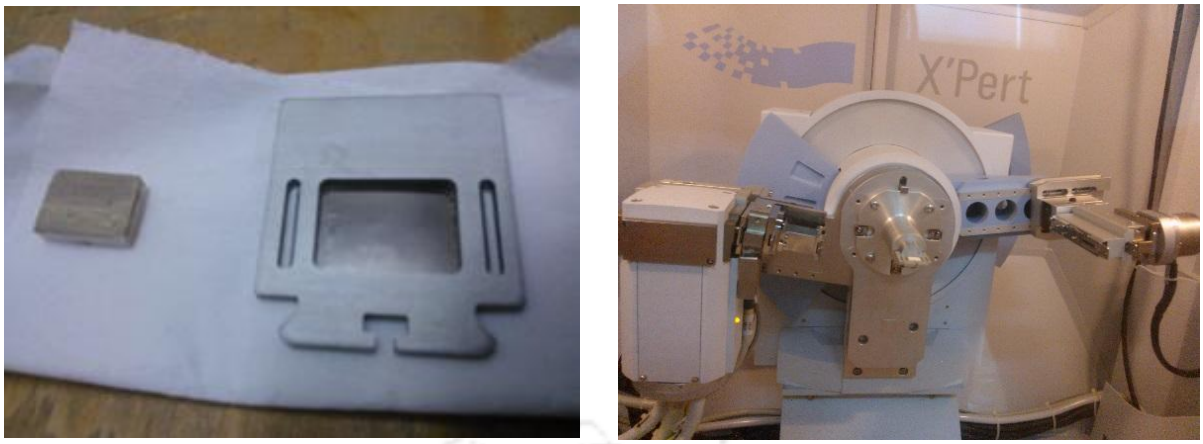

(a) **(b)**

Fig. B.4 (a) XRD sample holder and (b) XRD setup

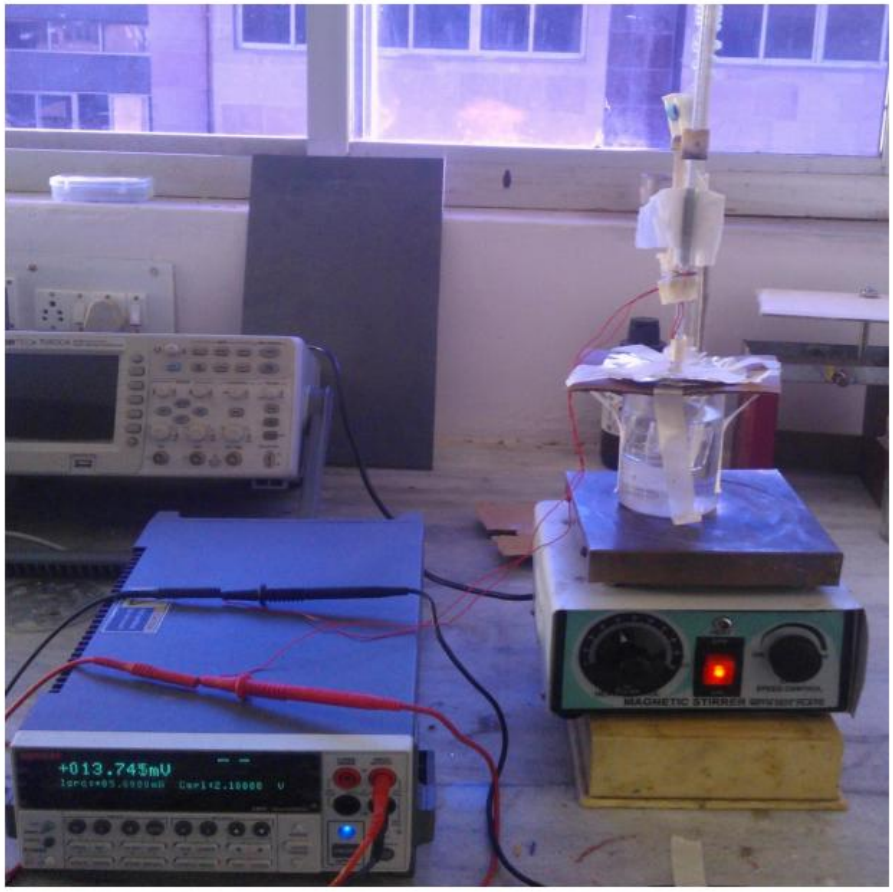

Fig. B.5 Oil bath calibration setup

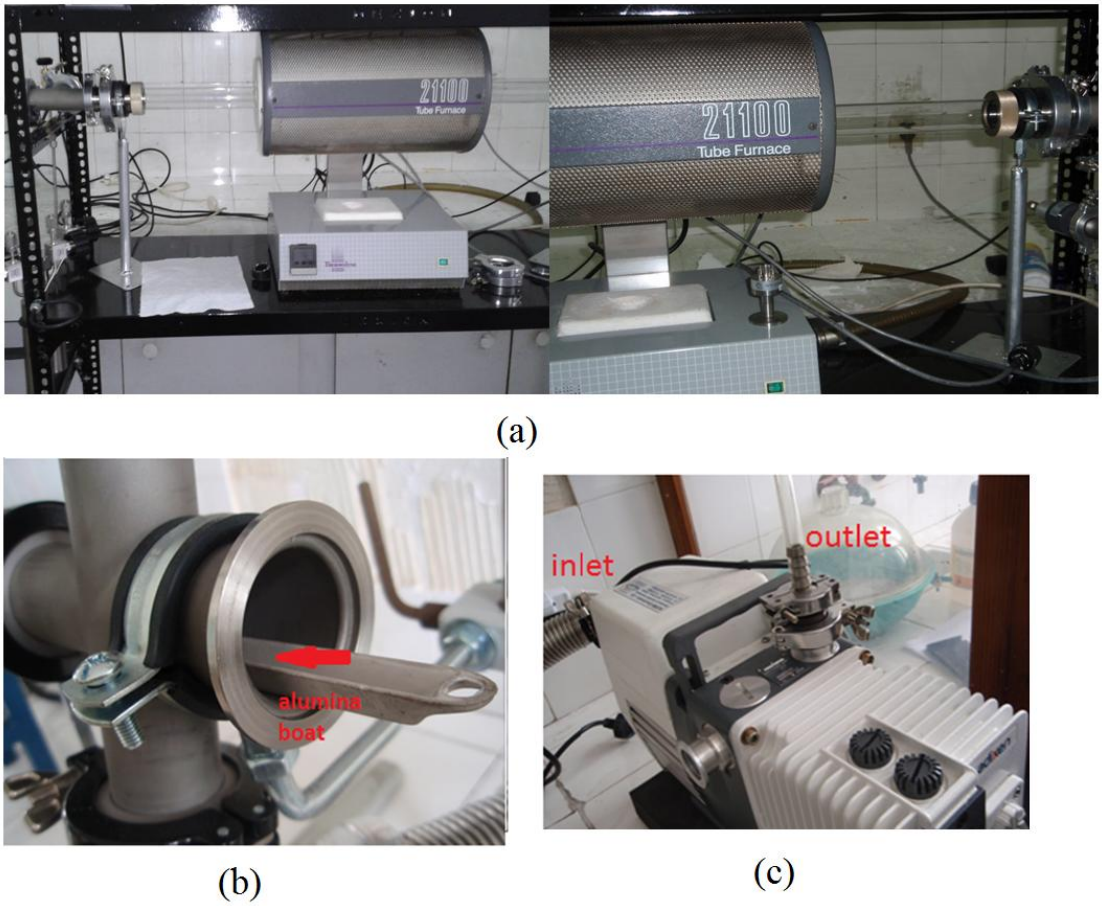

Fig. B.6 The LPCVD setup for growing CNT and graphene

Fig. B.7 Sample holder for Vander Paw measurement

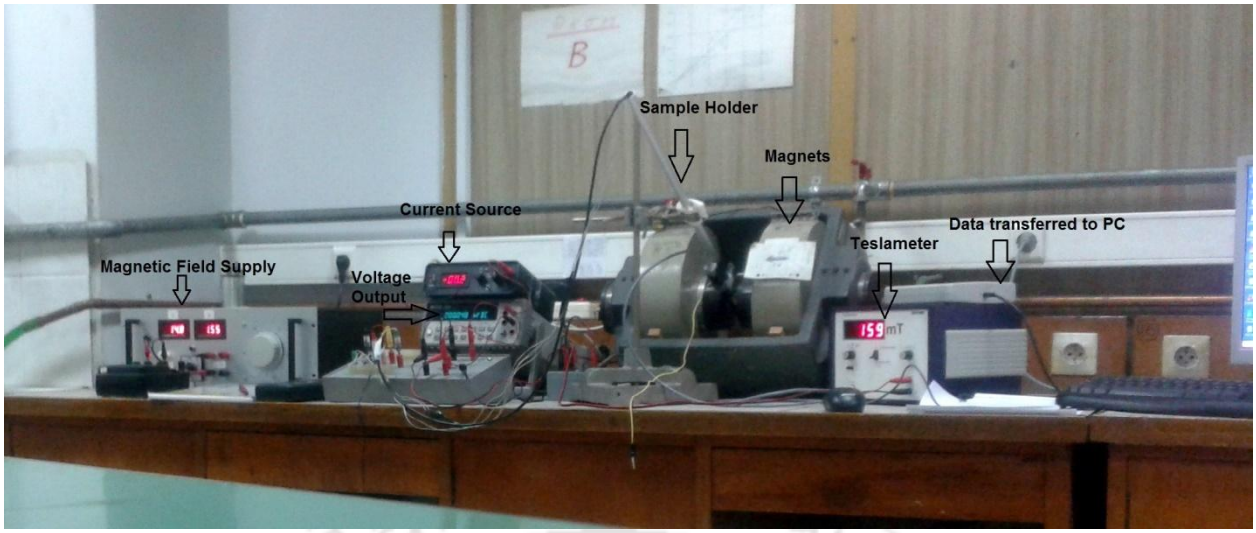

Fig. B.8 The complete setup for Hall co-efficient and Vander Paw measurement

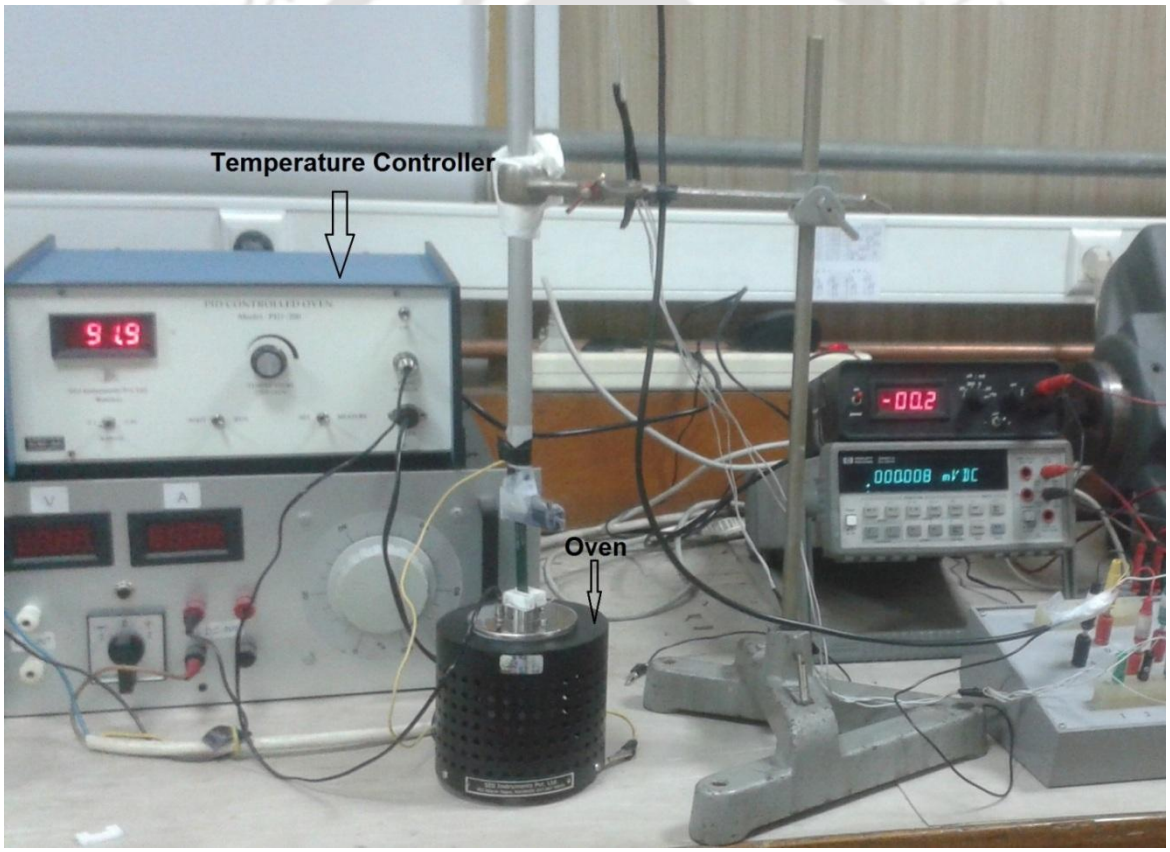

Fig. B.9 The setup for measuring TCR of multilayer film

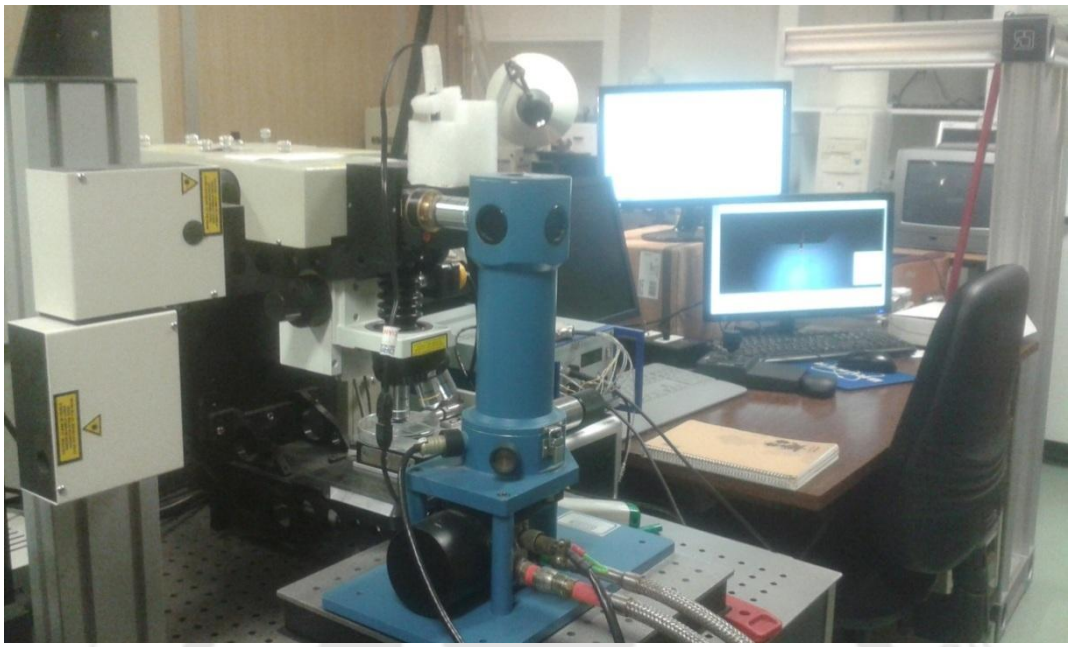

Fig. B.10 Raman spectrometer

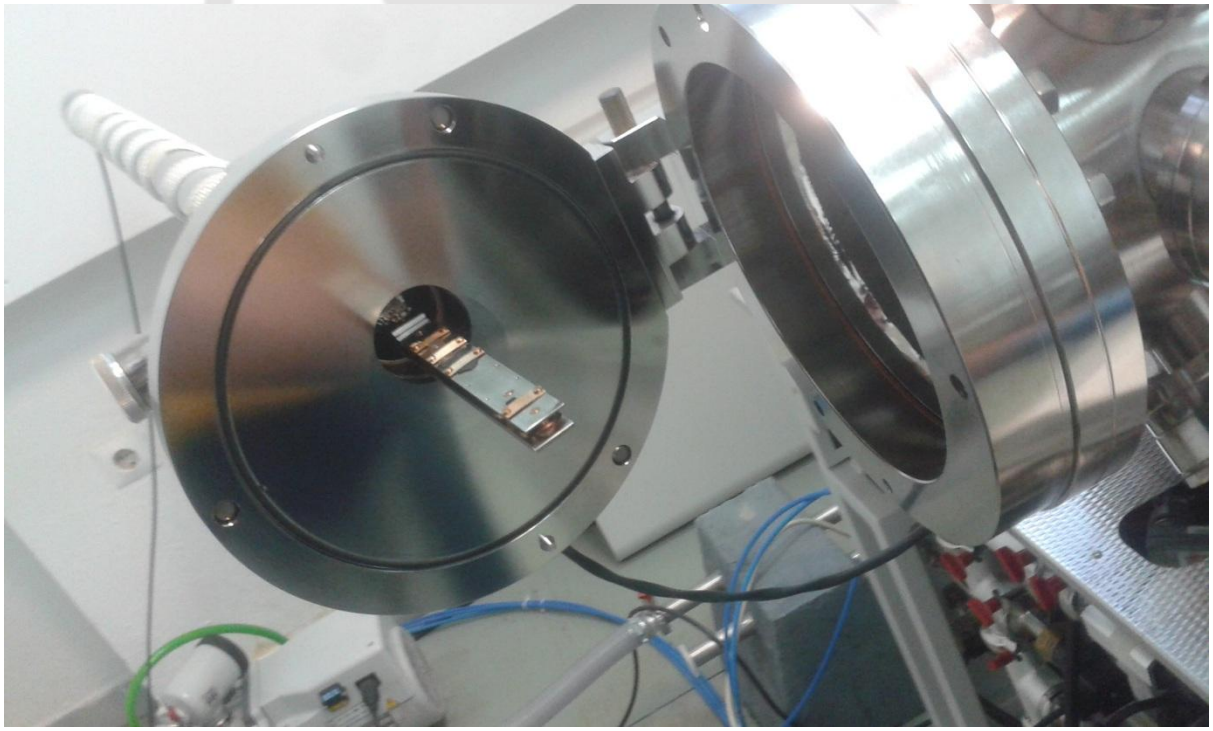

Fig. B.11 The XPS/AES setup

APPENDIX C

Specifications of instruments and properties of materials

Table C.1 Properties of substrate materials

Substrate	ρ (kg/m^3)	c (J/kg/K)	k (W/m/k)	α' (cm^2/s)	$\sqrt{\rho ck}$ J/cm^2/K/S$^{1/2}$
Pyrex	2220	775	1.36	0.00791	0.153
Macor	2520	790	1.46	0.00733	0.171
Silver	10490	233	429	1.75	3.238
Platinum	21450	130	71.6	0.257	1.413
Gold	19300	130	318	1.27	2.825

Table C.2 Brief specifications of high precision non-contact computerized surface profilometer (Taylor Hobson)

Description	Specification
Precision	1 Mega Pixel
Magnification	20x
Field of view	0.825 mm × 0.825 mm
Focal distance	4.7 mm
Power supply	220 V AC supply

Table C.3 Vacuum coating unit specifications (VACUUM TECHNIQUES (P) LTD)

Chamber size	**12" Metallic Belljar**
Material	SS 304
Chamber lifting mechanism	Manual Lifting
Diffusion pump model	VT-DP-114
Size	4 1/2"
Pumping Speed	500 lit/sec
Rotary pump model	VT 2012
Displacement	250 lit/min
High Vac Valve	4" Butterfly valve
Roughing and Backing valve	1" Butterfly valve
Vacuum Measuring Gauges	Digital Pirani-Penning Gauge
HT Power supply	3 KV, 50 mA
LT Power supply	10 V at 200 Amp and 20 V at 100 Amp
Cooling mechanism	Water cooled
Other items	LN2 trap

Table C.4 Density and acoustic impedance values for selected materials which are to be fed to vacuum coating unit

Material	Symbol	Density (g/cm^3)	Impedance $(g/cm^2 \sec)\times 10^5$
Aluminum	Al	2.70	8.17
Copper	Cu	8.93	20.21
Gold	Au	19.30	23.18
Iron	Fe	7.86	25.30
Palladium	Pd	12.00	24.73
Platinum	Pt	21.40	36.04
Silver	Ag	10.50	16.69

Table C.5 Equipment used in four point technique for measuring resistivity

Description	Specification	Remarks
Current Source	Constant current source can supply current from range 10 μA to 100 mA with accuracy 0.05% offset 10 nA	Keithley 224 Programmable Current Source
Voltmeter	Maximum output ± 1.2V with accuracy ± 0.1% of output	Keithley 2182 Nanovoltmeter

Table C.6 Equipment used for static calibration of thin film gauges fabricated

Description	Specification	Remarks
Silicone oil	Viscosity: $10^{-5} m^2/\text{sec}$ Density: $9.3\times10^5 kg/m^3$ Temperature range – 40^0C to 280^0C	High viscosity index and high chemical and thermal stability
Heater	Magnetic Stirrer with hot plate	Used for heating the oil bath
Source Meter	Source voltage: 5V to 210V; measure voltage: 1 μV to 211V; Source current: 50pA to 1.05A; measure current: 10pA to 1.055A Accuracy 0.015% volts and 0.035% current	Keithley 2400 SourceMeter
Thermometer	Least count 0.2^0C	Used to measure the temperature of hot air
Multimeter	Digital LC Meter	Used for measuring voltage difference in TFG

Table C.7 Laser parameters

Model: (LVD Orion 3015; 2.5 kW)	
Operational Parameters	Inputs
Input Power	10W, 20W
Pulse Frequency	500Hz
Duty Cycle	50
Time of Exposure	0.1s

APPENDIX D

Surface profiling of silver TFG using profilometer

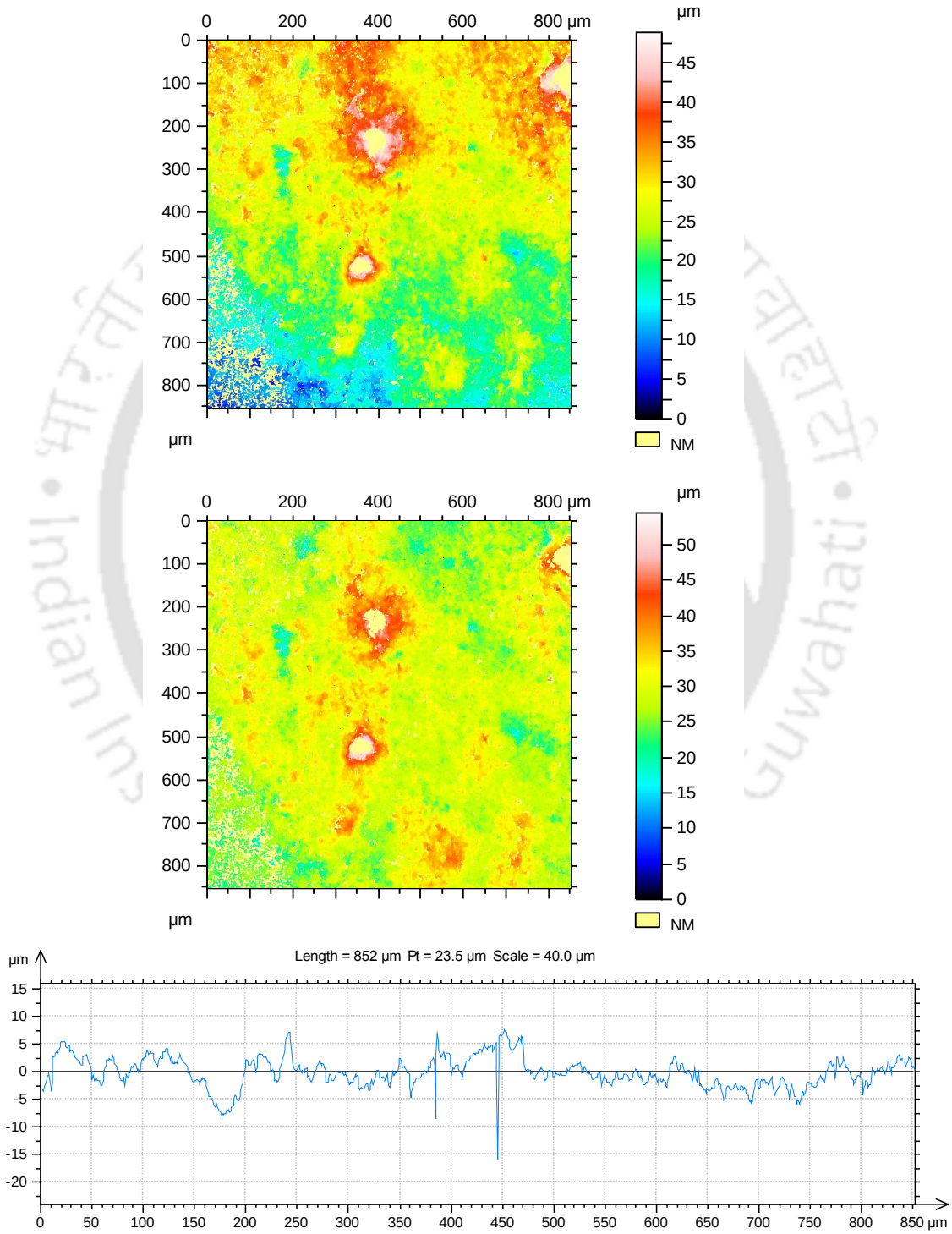

ISO 4287

Amplitude parameters - Roughness profile

Rp	6.84	µm	Gaussian filter, 0.25 mm
Rv	12.5	µm	Gaussian filter, 0.25 mm
Rz	19.3	µm	Gaussian filter, 0.25 mm
Rc	5.56	µm	Gaussian filter, 0.25 mm
Rt	25.5	µm	Gaussian filter, 0.25 mm
Ra	1.78	µm	Gaussian filter, 0.25 mm
Rq	2.46	µm	Gaussian filter, 0.25 mm
Rsk	-0.788		Gaussian filter, 0.25 mm
Rku	10.2		Gaussian filter, 0.25 mm

Material Ratio parameters - Roughness profile

Rmr	0.691	%	c = 1 µm under the highest peak, Gaussian filter, 0.25 mm
Rdc	3.05	µm	p = 20%, q = 80%, Gaussian filter, 0.25 mm